High Field ^{1}H-NMR Spectroscopy on Cell Suspensions of Neural Progenitor Cells and Brain Tumor-Initiating Cells

DISSERTATION ZUR ERLANGUNG DES DOKTORGRADES
DER NATURWISSENSCHAFTEN (DR. RER. NAT.)
DER FAKULTÄT FÜR BIOLOGIE UND VORKLINISCHE MEDIZIN
DER UNIVERSITÄT REGENSBURG

vorgelegt von
Paul Ramm

aus
Regensburg

im Jahr 2011

Das Promotionsgesuch wurde eingereicht am: 08.03.2011

Die Arbeit wurde angeleitet von: Prof. Dr. Dr. Hans Robert Kalbitzer

Unterschrift: _____

Outline

1. Abstract

NMR spectroscopy of living organisms provides a non-invasive and comprehensive insight into cellular composition and metabolism. In addition, identifying cell-specific NMR spectroscopic signals and patterns may lead to *in vivo* detection and tracking of different cell types including stem cells and tumor-initiating cells.

In this dissertation, the methodology of *in vitro* high-resolution ^{1}H-NMR spectroscopy on cell suspensions of brain-derived stem cells was investigated. Different sample preparations of cell suspensions, i.e. agarose embedding, sedimentation and pelleting, were compared regarding reproducible interpretation of NMR spectra. A possible explanation for cell density-dependent line broadenings, namely inhomogeneous magnetic B-field distributions, was supported by numerical simulations of B-field distortions in consequence of differences in magnetic susceptibility between intracellular and extracellular compartments. Methods were analyzed that allowed discrimination between different subtypes of NMR-visible molecules within cell suspensions. It could be shown that highly-resolved resonances almost exclusively originated from extracellular molecules. In case of metabolites and amino acids, a further pool of molecules with reduced self-diffusion was identified that gave rise to line broadened resonances. Regarding NMR-visible macromolecules, different relaxation- and diffusion-parameters were exploited to disentangle contributions from mobile lipids and mobile proteins. With respect to temperature, a reasonable long-term stability could be shown in NMR spectra acquired at 5° C, whereas at 37° C a stopped metabolism followed by continuous proteolysis was observed.

Moreover, the biological relevance of NMR-visible mobile lipids was investigated in terms of cellular stress and regarding stem cell-specificity. In cultured neural progenitor cells (NPC) and glioblastoma-derived tumor-initiating cells (BTIC) a positive correlation of mobile lipids to cell death was revealed. A further promoting factor for mobile lipid appearance and increase, i.e. cell culture confluence, could be identified not only in brain-derived stem cells, i.e. NPC and BTIC, but also for several control cell lines, e.g. mesenchymal stem cells (MSC), COS7 fibroblasts, and in one out of three differentiated glioblastoma tumor cell lines (GBM-TC “HTZ-417”). In contrast, a connection between mobile lipids and biological surrogate markers for stem cell identity, e.g. clonogenicity, could not be observed. However, cell type- and cell line-specific responses of confluence-induced mobile lipids to treatment with transforming growth factor β (TGF-β) were evident.

Adressing the NMR-visibility of cellular lipids, native low-density lipoproteins (LDL) and enzymatically degraded LDL (E-LDL) served as defined models for lipid droplets and lipid membranes, respectively. In contrast to native LDL, multilamellar E-LDL did not exhibit lipid resonances in NMR spectra, thus promoting the hypothesis of invisible lipid membranes. On the contrary, NMR spectroscopy of macrophages loaded with E-LDL revealed a transformation of the incorporated lipids to an at least partially NMR-visible structure. Furthermore, an increase in polyunsaturation of NMR-visible lipids was evident upon E-LDL-loading.

A small cohort of BTIC-lines was analyzed by statistical analyses to unveil possible connections between biological surrogate markers for stem cell identity and NMR-spectroscopic features. Regarding clonogenicity, a significant positive correlation to a specific NMR-spectral region including resonances of glutamate, mobile lipids and mobile proteins (2.28 ppm – 2.38 ppm) was calculated. Principal component analysis revealed a relative similarity of NMR spectra within each BTIC-line and a moderate clustering according to low or high clonogenicity.

2. Zusammenfassung

Die NMR-Spektroskopie an lebenden Organismen bietet einen nichtinvasiven und umfassenden Einblick in die Zusammensetzung und den Stoffwechsel auf zellulärer Ebene. Zusätzlich könnte die Identifizierung von zellspezifischen NMR-spektroskopischen Signalen und Signalmustern die Detektion und Verfolgung von unterschiedlichen Zelltypen inklusive Stammzellen und tumorinitiierenden Zellen *in vivo* ermöglichen.

Innerhalb dieser Dissertation wurde die Methodik der hochaufgelösten *in vitro* ^{1}H-NMR-Spektroskopie an Zellsuspensionen von Gehirn-assoziierten Stammzellen untersucht. Es wurden unterschiedliche Probenpräparationsmethoden bezüglich einer reproduzierbaren Interpretation der NMR-Spektren verglichen, insbesondere das Einbetten der Zellen in Agarose bzw. die Bildung eines Zellpelletts durch Sedimentation. Eine mögliche Erklärung für Zelldichte-abhängige Linienverbreiterungen, nämlich inhomogene Magnetfeld-Verteilungen, wurde unterstützt durch numerische Simulationen der magnetischen B-Feldverzerrungen als Folge unterschiedlicher magnetischer Suszeptibilitäten zwischen intrazellulären und extrazellulären Kompartimenten. Methoden wurden analysiert, die eine Unterscheidung von NMR-sichtbaren Molekül-Subgruppen innerhalb der Zellsuspensionen ermöglichten. Es konnte gezeigt werden, dass hochaufgelöste Resonanzen ihren Ursprung fast ausschließlich in extrazellulären Molekülen hatten. In Bezug auf NMR-sichtbare Makromoleküle wurden unterschiedliche Relaxations- und Diffusionsparameter ausgenutzt, um Anteile mobiler Lipide von denen mobiler Proteine zu separieren. Hinsichtlich der Temperatur konnte eine vertretbare Langzeitstabilität in NMR-Spektren, die bei 5° C aufgenommen wurden, festgestellt werden, wohingegen bei 37° C Anzeichen von metabolischem Stillstand und kontinuierlichem Proteinabbau beobachtet werden konnten.

Darüber hinaus wurde die biologische Relevanz der NMR-sichtbaren mobilen Lipide in Bezug auf zellulären Stress und auf Stammzellspezifität untersucht. In kultivierten neuralen Vorläuferzellen (NPC) und Glioblastom-assoziierten tumorinitiierenden Zellen (BTIC) wurde eine positive Korrelation zwischen den mobilen Lipiden und Zelltod aufgedeckt. Es konnte ein weiterer begünstigender Faktor für das Auftreten und die Zunahme von mobilen Lipiden identifiziert werden, nämlich Zellkulturkonfluenz, nicht nur in Gehirn-assoziierten Stammzellen, d.h. NPC und BTIC, sondern auch in mehreren Kontrollzelllinien, z.B. mesenchymalen Stammzellen (MSC), COS7-Fibroblasten und in einer der drei untersuchten differenzierten Glioblastom-Tumorzelllinien (GBM-TC „HTZ-417“). Im Gegensatz dazu konnte ein Zusammenhang zwischen mobilen Lipiden und biologischen Surrogatmarkern für Stammzellidentität, z.B. Klonogenität, nicht beobachtet werden. Jedoch zeigten sich zelltyp- und zelllinienspezifische Reaktionen auf Behandlung mit transformierenden Wachstumsfaktoren (TGF-β) in den mobilen Lipidsignalen.

Zur Untersuchung der NMR-Sichtbarkeit von zellulären Lipiden dienten native Lipoproteine (LDL) als Modellstrukturen für Lipidtröpfchen und entsprechend enzymatisch degradierte Lipoproteine (E-LDL) als Modelle für Membranstrukturen. Im Gegensatz zu nativem LDL zeigten die multilamellaren E-LDL keine Lipidresonanzen in den NMR-Spektren, was die

These bekräftigte, dass Lipidmembranen NMR-unsichtbar sind. Auf der anderen Seite deckte die NMR-Spektroskopie von E-LDL-beladenen Makrophagen auf, dass die aufgenommenen Lipide zumindest teilweise in NMR-sichtbare Strukturen umgewandelt wurden. Zusätzlich konnte ein Anstieg im Grad der Mehrfachsättigung der NMR-sichtbaren Lipide infolge der E-LDL-Beladung beobachtet werden.

Im Rahmen einer kleinen Studie an BTIC-Linien wurden statistische Methoden angewendet, um mögliche Zusammenhänge zwischen biologischen Surrogatmarkern für Stammzell-identität und NMR-spektroskopischen Merkmalen aufzudecken. Im Bezug auf Klonogenität wurde eine signifikante positive Korrelation zu einer bestimmten NMR-spektralen Region (2.28 ppm – 2.38 ppm) berechnet, die Resonanzen von Glutamat, mobilen Lipiden und mobilen Proteinen beinhaltet. Hauptkomponentenanalysen ergaben eine relative Ähnlichkeit in NMR-Spektren von Proben derselben BTIC-Linie, und deckten ein mittelmäßiges Clustern in Bezug auf hohe und niedrige Klonogenität auf.

3. Introduction

The idea of this dissertation was to investigate brain-derived stem cells by means of high-resolution nuclear magnetic resonance (NMR) spectroscopy *in vitro* in order to reveal stem cell-specific biomarkers. Since putative NMR-spectroscopic biomarkers could possibly be applied *in vivo* to monitor stem cell-associated phenomena, e.g. neurogenesis, tumorigenesis, and neurodegeneration, a reproducible *in vitro* method was sought for that represents the connective link between pure *in vitro* NMR spectroscopy of biofluids on the one hand, and clinical *in vivo* MR spectroscopy on the other hand.

Therefore, NMR spectroscopy of cell suspensions was considered superior to NMR spectroscopy of cell lysates or cell culture conditioned media, although it had to be established first in our department, and although it soon turned out that evaluation and interpretation of cell suspension spectra was by no means trivial. Nevertheless, the relative closeness to the *in vivo* situation tipped the scales in favor of investigating whole cells.

In order to overcome difficulties arising from NMR spectroscopy of cell suspensions, sample preparation methods were compared, influences of the sample heterogeneity on magnetic B-field distortions were simulated, approaches to obtain intracellular informations were conceived and analyzed, and methods to disentangle contributions of NMR-visible molecules were explored. The outcomes are presented in the first part of the Results chapter (section 5.1) and discussed in the first part of the Discussion chapter (section 6.1).

Apart from methodological investigations, the biological relevance of a certain species of NMR-visible macromolecules, so-called mobile lipids, was investigated. Possible connections to the stem cell identity and to cellular stress were examined in a variety of cultured cell types, especially neural progenitor cells (NPC) and their malignant counterparts, brain tumor-initiating cells (BTIC). New insights on this context are presented in the second part of the Results chapter (section 5.2) and discussed in the second part of the Discussion chapter (section 6.2).

A small study on NMR-visible lipid resonances in lipoproteins and in lipoprotein-loaded macrophages shed some further light on the nature of NMR-visible macromolecules. The results of this study are presented and discussed in sections 5.3 and 6.3, respectively.

An entirely different approach was chosen in a pilot study on brain tumor-initiating cells. Whole spectra as well as predefined spectral regions-of-interest were investigated by means of principal component analysis. Moreover NMR-spectral correlations to available biological data on hallmarks of stem cell identity, e.g. the ability to form clones from single cells, were calculated and evaluated. The results and their discussion can be found in sections 5.4 and 6.4.

In this Introduction chapter, basic theoretical approaches and seminal literature regarding NMR spectroscopy of cells and characteristics of brain-derived stem cells are summarized with respect to the understanding of the results and discussion presented in this dissertation. A general introduction both to the basics of NMR spectroscopy and to stem cell

biology is considered beyond the scope of this thesis. Alternatively, the reader is referred to standard NMR spectroscopy text books [Levitt 2008; Keeler 2005] and seminal reviews on neural stem cells [Lie et al. 2004; Reya et al. 2001], and brain tumor initiating cells [Vescovi et al. 2006; Reya et al. 2001].

3.1. NMR Spectroscopy of Cells

NMR spectroscopy of cells ranges from pure *in vitro* spectroscopy of cell culture supernatants and cell lysates to spatially resolved *in vivo* spectroscopy at clinical scanners. The different methods are summarized in the first section. Cell suspension NMR spectroscopy is between pure *in vitro* and clinical *in vivo* spectroscopy. On the one hand, it deals with cultured cells and can be carried out on ultra-high field NMR spectrometers. On the other hand, it examines cells under a quasi-physiological condition that show spectroscopic features similar to the *in vivo* situation. Two main obstacles in cell NMR spectroscopy, field distortions induced by magnetic susceptibility inhomogeneities and limited NMR-visibility due to hindered molecular motion, are addressed in the second and third sections, respectively. The last section focusses on a special subclass of intracellular macromolecules that may be detected in cells and also *in vivo*, so-called mobile lipids and mobile proteins.

3.1.1. Approaches to Cellular NMR Spectroscopy

NMR spectroscopy is capable of identifying and quantifying up to hundreds of different dissolved molecules in a biological sample, e.g. in urine, for the purpose of metabolomic studies [Beckonert et al. 2007]. Despite this enormous potential, the word “dissolved” should be emphasized, because high resolution NMR spectroscopy is mostly limited to molecules which tumble fast enough so that anisotropies are averaged out. This phenomenon is addressed in more detail in section 3.1.3. Owing to this limitation, a straight-forward method to analyze cellular compositions and metabolism by NMR spectroscopy is to investigate soluble fractions, either conditioned media/supernatants or cell extracts/lysates.

Studies on cell culture **supernatants** are mostly carried out using ^{13}C-labeled substrates whose metabolic products are also ^{13}C-labeled and thus can easily be distinguished from medium ingredients by ^{13}C-NMR spectroscopy. As an example, main parts of the amino acid metabolism and transport of/between neurons and astocytes was unveiled through this method [Zwingmann & Leibfritz 2003]. However, also ^{1}H-NMR spectroscopic investigations of supernatants are meaningful. Since supernatant NMR spectra rather display metabolic traces of cell metabolism than the ongoing metabolism itself, it is frequently referred to as metabolic “footprint”.

In contrast to NMR spectroscopy of supernatants, **cell extracts** yield direct information on intracellular metabolites. Therefore, extract NMR spectra are occasionally termed metabolic

“fingerprint”. There are many protocols on how to extract cells for NMR, but the most common ones are perchloric-acid (PCA) extractions [Urenjak et al. 1993] and methanol/chloroform (MC) extractions [Folch et al. 1957]. The former yields acid-soluble hydophilic metabolites and proteins, the latter provides both hydrophobic lipids and hydrophilic methanol-soluble metabolites in two separate phases. Both methods were compared in a study by Le Belle *et al.* [Le Belle et al. 2002] concluding that MC extraction is superior to PCA extraction in both yield and reproducibility. Employing these methods, many insights into cellular metabolism could be gained, e.g. cell-specific metabolic patterns. This allowed e.g. discrimination among neural cell types such as neurons, astrocytes, oligodendrocytes, O2A-progenitors and tumor cells [Urenjak et al. 1993].

Despite the wealth of information obtained by NMR spectroscopy of extracts, there are also drawbacks of this methodology: First, spectra of such intensely chemically processed samples cannot be compared with those acquired *in vivo*. Obviously, the latter constitutes a heterogeneous mixture of cells embedded in an extracellular matrix. Second, informations on the mobility of molecules within intact cell are lost, e.g. informations on self-diffusion coefficients, on restrictions in diffusion and thus on compartmentization, and on bindings to diverse cellular structures, e.g. to cytoskeleton proteins. Third, there are certain organelles and other cellular compartments, e.g. lipid bodies, that are not recovered by common extraction methods, and thus cannot be investigated, at least not in their native state.

In contrast, *in vitro* NMR spectroscopy of unprocessed **cell suspensions** has proven to be a very powerful method to study intracellular compositions in their natural environment. However, the NMR-visibility of intracellular metabolites and the possibility to distinguish intracellular and extracellular fractions are still matters of debate [Duarte et al. 2009] and are also addressed in detail within this dissertation (sections 5.1.4 and 6.1). Nevertheless, a special subclass of macromolecules called “mobile lipids” can be detected by NMR spectroscopy of suspensions but not of extracts. These highly informative macromolecule resonances are introduced in section 3.1.4, and constitute one focus of this thesis. A further unique feature of this methodology is the possibility to perfuse cells with nutrients and oxygen during the measurement [Brand et al. 1998]. By means of perfusion, metabolic information of cells may be obtained under physiological cell culture conditions. Moreover, these conditions can be varied, e.g. from normoxia to hypoxia, which makes perfusion NMR spectroscopy a very unique tool. No other method is able to yield such comprehensive information from within living cells under both physiological and highly variable conditions.

A further method of NMR spectroscopy of cells has been attracted more and more attention within the last few years: **Magic angle spinning** (MAS), a technique originating from solid-state NMR spectroscopy. A detailed introduction to this area of research is beyond the scope of this dissertation, so the reader is referred to standard textbooks, e.g. written by Duer [Duer 2002] and seminal papers [Andrew et al. 1958; Andrew et al. 1959] on this topic. Briefly, small samples are spun at very high frequencies (up to several kHz) around an axis tilted by the so-called magic angle (approximately 54.7°) with respect to the external magnetic B-field. Thereby, distinct line broadening effects, e.g. dipole-dipole couplings, chemical shift anisotropy and magnetic susceptibility changes, are partly averaged out. This facilitates high resolution NMR spectroscopy of solids and – in case of cellular NMR spectroscopy – of intracellular metabolites [Mirbahai et al. 2010]. Thus, this method exhibits the advantages of both cell extractions and cell suspensions, namely high resolution of both intracellular metabolites and macromolecules within their native compartments. However,

the cell integrity remains questionable at such high spinning rates [Opstad et al. 2008a]. Additionally, the perfusion of cells during the measurement is not possible. Nevertheless, MAS-NMR spectroscopy of cells seems to become state-of-the-art, although this technique has not been widely used yet.

A short remark about *in vivo* NMR spectroscopy [de Graaf 2007] should not be missing in this cell-NMR overview, although it constitutes a special case. Nevertheless, there are remarkable similarities between *in vivo* spectra and their *in vitro* counterparts. For example, spatially resolved NMR spectra within glioma in rats [Lehtimäki et al. 2003] show comparable features with *in vitro* suspension NMR spectra of glioma cell lines [Barba et al. 2001]. However, especially in the case of clinical *in vivo* NMR spectroscopy, the very poor sensitivity and resolution limit the informative value of this technique [McLean et al. 2000].

Tab. 3.1 summarizes advantages and drawbacks of the respective methodology and its informative value with respect to NMR-visibility.

Molecules	**Supernatant**	**Extracts**	**Suspension**	**MAS**	***in vivo***
Extracellular metabolites	sharp	n.d.	sharp (low cell densities)	unknown	broad
Intracellular metabolites	n.d.	sharp	unknown	sharp	broad
Membrane compounds	n.d.	sharp, degraded	n.d.	n.d.	n.d.
Mobile lipids	n.d.	sharp, degraded	broad	broad	broad
Mobile proteins	n.d.	partially, broad	broad	broad	broad
Advantages	straight forward, high-throughput, resolution	resolution, informational content	straight forward, perfusable	resolution	clinically available, non-invasive
Drawbacks	informational content	preparation artifacts, degraded macromolecules	discrimination extra- vs. intracellular, resolution	availability, cell viability	very limited resolution and sensitivity

Tab. 3.1 Cellular NMR-spectroscopic methods: Visibility, advantages, drawbacks. Different methods in columns. “Extracts”: Perchloric-acid extraction and methanol/chloroform extraction, “MAS”: Magic angle spinning, “*in vivo*”: Spatially resolved NMR spectroscopy at clinical magnetic resonance imaging scanners, “sharp”: Linewidth below 7 Hz, “unknown”: Not clarified in detail yet, “broad”: Linewidth above 7 Hz, typically >30 Hz for macromolecules, “n.d.”: not detectable.

3.1.2. Susceptibility-Induced Magnetic B-Field Distortions

Susceptibility-induced magnetic B-field distortions are well-known phenomena that occur in all samples with non-constant susceptibility distributions when brought into a magnetic field. In some special cases this effect solely changes the offset of the magnetic B-field, facilitating e.g. highly resolved NMR spectroscopy of a diamagnetic solution inside an NMR tube that is surrounded by paramagnetic air. In contrast, in randomly distributed and shaped

compartments that exhibit individual susceptibilities, the magnetic B-field becomes inhomogeneous. In this case, high-resolution ^{1}H-NMR spectroscopy may be limited.

In this section, a method is derived which enables simulations of susceptibility-induced B-field distortions. In order to provide a comprehensive derivation of this method, in the first part, fundamentals of NMR-detectable magnetic fields are discussed.

The frequency which is measured in NMR spectroscopy is proportional to the magnetic B-field at the site of the nucleus:

$$f = \gamma/2\pi \cdot B_{\mathrm{nuc}} \qquad 3.1$$

with the Larmor frequency f, the gyromagnetic ratio γ ($\gamma/2\pi$ = 42.6 MHz/T), and the B-field at the nucleus B_{nuc}. In contrast to the apparent simplicity of Eq. 3.1, the field B_{nuc} has many contributions, and in general they cannot be determined analytically. Neglecting couplings (e.g. J-coupling or dipole coupling) the four main steps towards B_{nuc} are [Durrant et al. 2003]:
First, the **homogeneous applied magnetic B-field $\boldsymbol{B_0}$** due to the current within the superconducting coils of the NMR spectrometer, as would be measured in vacuum;
Second, the **macroscopic B-field $\boldsymbol{B_{\mathrm{mac}}}$** in which the reaction of matter to the applied field B_0 is incorporated. This term is determined by the Maxwell equations for magnetostatics (*vide infra*) and is derived by averaging over microscopic magnetism to yield macroscopic expressions. In other words, these expressions do not depend on parameters at the discrete molecular scale, but on continuous variables like the magnetization, the magnetic susceptibility etc. (*vide infra*);
Third, the **local B-field $\boldsymbol{B_{\mathrm{loc}}}$** which corrects the macroscopic field B_{mac} about the error that occurs by averaging over the region of the focused nucleus. Conceptionally, a so-called "Sphere of Lorentz" is spanned around the molecule of interest, in which there is nothing but the molecule. It can be shown [Durrant et al. 2003] that

$$\vec{B}_{\mathrm{loc}}(\vec{r}) = \vec{B}_{\mathrm{mac}}(\vec{r}) \cdot (1 - \frac{2}{3}\chi_{\mathrm{surr}}(\vec{r})) \qquad 3.2$$

with the magnetic susceptibility of the matter surrounding the focussed molecule χ_{surr}. Note that in general, both the local B-field and the macroscopic B-field are vectors and depend on postion (postion vector $\vec{\mathrm{r}}$). The principle of the "Sphere of Lorentz" was introduced in electrostatics of dielectric media by Lorentz [Lorentz 1916] and transferred to the NMR situation by Dickinson [Dickinson 1951]. Incorporating this concept, correct susceptibility-induced magnetic B-field distributions can be calculated analytically for regularly shaped samples [Live & Chan 1970], and even for simplified models of cells, e.g. erythrocytes in blood plasma [Durrant et al. 2003];
The **nuclear B-field $\boldsymbol{B_{\mathrm{nuc}}}$** which finally introduces the electronic shielding/deshielding within the molecule of interest. The shielding difference between this molecule and a standard compound (e.g. DSS) is the most frequently used variable in NMR spectroscopy, the chemical shift:

$$\vec{B}_{\mathrm{nuc}}(\vec{r}) = \vec{B}_{\mathrm{loc}}(\vec{r}) \cdot (1 - \sigma) = \vec{B}_{\mathrm{nuc,ref}}(\vec{r}) \cdot (1 + \delta) \qquad 3.3$$

with the electronic shielding σ, the nuclear B-field for the reference compound (e.g. DSS) $B_{\mathrm{nuc,ref}}$, and the chemical shift δ.

In the following, a Fourier-based approach to calculate the local B-field distortions due to sample heterogeneities is derived based on publications of Salomir *et al.* and Marques *et al.* [Salomir et al. 2003; J. P. Marques & Bowtell 2005]. In order not to get confused with different definitions for magnetic fields and other magnetic variables, some definitions have to be given first.

The **magnetic B-field** is defined through its interaction with moving electric charges:

$$\vec{F}_L = q \cdot \vec{v} \times \vec{B} \qquad 3.4$$

with the Lorentz force $\vec{F}_L$, the charge of a probing particle q, and its velocity $\vec{v}$. In matter, the B-field does not only originate from free currents (described by the law of Biot-Sarvart), but also depends on "bound" currents, e.g. induced electron currents in atom orbitals (i.e. diamagnetism). These two contributions can conceptionally be separated. The "bound" current part is called **magnetization** and is defined as the average over the magnetic dipole moment times the dipole density:

$$\vec{M} = \frac{N}{V} \cdot \vec{m} = n \cdot \vec{m} \qquad 3.5$$

with the magnetization $\vec{M}$, the number of magnetic dipoles per volume $n = N/V$, and the magnetic dipole moment $\vec{m}$. In contrast, the "free" current component is named **magnetic H-field** or auxillary field, and is defined by the difference of the B-field and the magnetization:

$$\vec{H} = \frac{\vec{B}}{\mu_0} - \vec{M} \qquad 3.6$$

with the vacuum permeability (also known as magnetic constant) μ_0. Neglecting ferromagnets and other highly magnetic materials, the magnetization is proprotional to the magnetic H-field:

$$\vec{M} = \chi \cdot \vec{H} \qquad 3.7$$

with the dimensionless proportionality factor χ which is called **magnetic susceptibility**. In general, the magnetic susceptibility is not a scalar but a tensor, e.g. in lipid membranes [Azanza et al. 1993]. Moreover, the susceptibility itself may depend on the magnetic field, e.g. in ferromagnets. However, here, calculations are based on the approximation of a linear and scalar susceptibility.

The magnetic susceptibility is a property of the material that gives the reaction of the "bound" currents to an applied magnetic H-field. Usually, it is very small, e.g. expressed in parts per million (ppm). For diamagnets it is negative, and positive for paramagnets. Eq. 3.7 also implies that $\vec{B}$, $\vec{H}$ and $\vec{M}$ are parallel or antiparallel.

In magnetostatics (no free currents) the macroscopic magnetic field is governed by two simplified Maxwell equations:

$$\begin{aligned} \mathrm{rot}\vec{H} &= \nabla \times \vec{H} = 0 \\ \mathrm{div}\vec{B} &= \nabla \cdot \vec{B} = 0 \end{aligned} \qquad 3.8$$

with the del-operator $\nabla = (\partial/\partial x, \partial/\partial y, \partial/\partial z)$. The first row of Eq. 3.8 is Ampere's law for zero current density, the second row is Gauss' law. In other words, the H-field is curl-free and the B-field has no sources (i.e. there are no magnetic monopoles). Applying these two equations to magnetic fields at the boundary of two materials with different susceptibility, it can be shown that the tangential component of the H-field must be equal on both sides of the boundary. The same is true for the perpendicular component of the B-field.

A curl-free field is also conservative, therefore it can be written as the gradient of a scalar field. In case of the curl-free magnetic H-field, this scalar field is named the **magnetic potential $\boldsymbol{\phi}$**:

$$\vec{H} = -\nabla\phi \qquad 3.9$$

Applying the del-operator ∇ to Eq. 3.6 gives Poisson's equation:

$$\Delta\phi = \nabla\vec{M} \qquad 3.10$$

Inserting Eqs. 3.7 – 3.9 yields

$$(1+\chi)\cdot\Delta\phi + \nabla\chi\cdot\nabla\phi = 0 \qquad 3.11$$

with the Laplace operator $\Delta = \partial^2/\partial x^2 + \partial^2/\partial y^2 + \partial^2/\partial z^2$. Note that both χ and ϕ depend on position. In principle, the magnetic field distortions due to susceptibility inhomogeneities could be calculated by solving Eq. 3.11. considering the boundary conditions mentioned above. However, this partial differential equation cannot be solved analytically in general. Nevertheless, for regular shapes with homogeneous but different susceptibilities inside and outside, an analytical solution can be derived [Durrant et al. 2003]:

$$\begin{aligned} \vec{B}_{\mathrm{mac}}(\vec{r}) &= \vec{B}_0 + (\chi_{\mathrm{in}} - \chi_{\mathrm{out}})\cdot\left(\vec{B}_0 + \frac{1}{4\pi}\iint_S \frac{(\vec{B}_0\cdot\vec{n})\cdot(\vec{r}-\vec{r}')}{|\vec{r}-\vec{r}'|^3}\,d^2r'\right) = \\ &= \vec{B}_0 + (\chi_{\mathrm{in}} - \chi_{\mathrm{out}})\cdot\vec{B}_0\cdot\mathcal{D}_s \end{aligned} \qquad 3.12$$

with the susceptibilities inside and outside the regular shape χ_{in} and χ_{out}, respectively, and with the unit vector perpendicular to the surface of the shape $\vec{n}$. The integral has to be carried out over the whole surface of the shape and is incorporated in the so-called geometric demagnetization factor $\mathcal{D}_s$. For a sphere, and cylinders alligned parallel or perpendicular to the applied field, the demagnetization factors are

$$\mathcal{D}_s = \begin{cases} 2/3 & \text{for sphere} \\ 1 & \text{for cylinder} \parallel \vec{B}_0 \\ 1/2 & \text{for cylinder} \perp \vec{B}_0 \end{cases} \qquad 3.13$$

Therefore, inside a sphere filled with vacuum, e.g. the "Sphere of Lorentz", the macroscopic B-field is given by

$$\vec{B}_{\mathrm{mac}} = \vec{B}_0 \cdot (1 - \frac{2}{3}\chi_{\mathrm{out}}) \qquad 3.14$$

which resembles Eq. 3.2.

Since the applied magnetic field is much stronger than the other field components, it is reasonable to split the magnetic H-field and thus also the magnetic potential ϕ in two components: The strong "background" component of the applied field on the one hand, and the perturbation component due to the susceptibility $\chi(\vec{r})$ on the other hand:

$$\begin{aligned} \vec{H} &= \vec{H}_0 + \vec{H}_{\mathrm{pert}} \\ \phi &= \phi_0 + \phi_{\mathrm{pert}} \end{aligned} \qquad 3.15$$

with "0" and "pert" meaning "background" and "perturbation", respectively.
The background component of the magnetic potential is

$$\phi_0 = -\vec{H}_0 \cdot \vec{z} = -H_0 \cdot z \qquad 3.16$$

with the z-component of the position vector z, the z-component multiplied by the unit vector in z-direction $\vec{z}$, and the z-component of the background H-field H_0. Inserting Eqs. 3.15 and 3.16 in Eq. 3.11 yields

$$(1+\chi) \cdot \Delta\phi_{\mathrm{pert}} + \nabla\chi \cdot \nabla\phi_{\mathrm{pert}} - H_0 \cdot \frac{\partial\chi}{\partial z} = 0 \qquad 3.17$$

Since this equation already describes very small changes in magnetic potential due to susceptibility distributions, quadratic terms in χ and ϕ_{pert} can be omitted [K. M. Koch et al. 2006]. In other words, since $\chi \ll 1$ and $-\nabla\phi_{\mathrm{pert}} = \vec{H}_{\mathrm{pert}} \ll \vec{H}_0$, Eq. 3.17 can be approximated as

$$\Delta\phi_{\mathrm{pert}} = H_0 \cdot \frac{\partial\chi}{\partial z} \qquad 3.18$$

For partial differential equations of this kind, the Fourier transformation (FT) offers an elegant solution, since $\mathrm{FT}\{\partial^n / \partial x^n f(x)\} = (ik)^n \cdot \mathrm{FT}\{\mathrm{f(x)}\}$ [Erdelyi 1954]

$$\mathrm{FT}\{\phi_{\mathrm{pert}}\} = -H_0 \cdot \frac{ik_z}{\vec{k}^2} \cdot \mathrm{FT}\{\chi\} \qquad 3.19$$

with the vector and the z-coordinate of the spatial frequency domain (known as k-space) $\vec{k}$ and k_z, respectively. Since $\vec{H}_{\mathrm{pert}} = -\nabla\phi_{\mathrm{pert}}$,

$$\mathrm{FT}\{H_{\mathrm{pert,\,z}}\} = -H_0 \cdot \frac{{k_z}^2}{{k_x}^2 + {k_y}^2 + {k_z}^2} \cdot \mathrm{FT}\{\chi\} \qquad 3.20$$

with the z-component of the perturbation part of the H-field $H_{\mathrm{pert,z}}$.
According to Eq. 3.2, the local B-field can be expressed as

$$B_{\mathrm{loc}} = B_{\mathrm{mac}} \cdot \left(1 - \frac{2}{3}\chi\right) = \mu_0 H_{\mathrm{mac}} \cdot (1+\chi) \cdot \left(1 - \frac{2}{3}\chi\right) \approx \mu_0 H_{\mathrm{mac}} \cdot (1 + \frac{1}{3}\chi) \qquad 3.21$$

neglecting terms quadratic in χ. Inserting Eq. 3.15 yield

$$\begin{aligned} B_{\mathrm{loc}} &\approx \mu_0 H_{\mathrm{mac}} \cdot \left(1 + \frac{1}{3}\chi\right) = \mu_0 H_0 \cdot \left(1 + \frac{1}{3}\chi\right) + \mu_0 H_{\mathrm{pert}} \cdot \left(1 + \frac{1}{3}\chi\right) \\ &\approx \mu_0 H_0 + \mu_0 H_0 \cdot \frac{1}{3}\chi + \mu_0 H_{\mathrm{pert}} \end{aligned} \qquad 3.22$$

again neglecting terms quadratic in χ.

The change in the local B-field due to the susceptibility distribution is therefore

$$B_{\mathrm{ind,\,z}} = B_{\mathrm{loc,\,z}} - B_0 = B_0 \cdot \frac{1}{3}\chi + \mu_0 H_{\mathrm{pert,\,z}} \qquad 3.23$$

The Fourier-transform of Eq. 3.23 and the application of Eq. 3.20 finally yields

$$\mathrm{FT}\{B_{\mathrm{ind,\,z}}\} = B_0 \cdot \left(\frac{1}{3} - \frac{{k_z}^2}{{k_x}^2 + {k_y}^2 + {k_z}^2}\right) \cdot \mathrm{FT}\{\chi\} \qquad 3.24$$

Therefore, the magnetic B-field distortions can be calculated by applying the Fourier transform to the susceptibility distribution, and subsequently by multiplying this k-space susceptibility distribution with a k-space-dependent scaling factor, followed by the inverse Fourier transform of this product. Since Eq. 3.21 solely depends on the change in susceptibility, and not on the absolute values, the solution derived here (Eq. 3.24) is not able to predict absolute B-field values. Instead, differences in magnetic B-field relative to the average value are obtained. In other words, the average of $B_{\mathrm{ind,\,z}}$ always vanishes.

For rapid computer-based calculations of the B-field distortion, the discrete Fast Fourier Transform (FFT) is suitable, because it is able to handle discrete susceptibility distributions. The fact that the discrete FFT acts on an image or matrix as if it was repeated periodically in all dimensions constitutes a drawback in the case of one isolated object of interest, which has to be compensated by adding homogenous “buffer-regions” around the object [J. P. Marques & Bowtell 2005]. However, this interesting side-effect of the Fourier transform approach can also be of great benefit in the case of periodic problems. For instance, distance-dependent field distortions may be simulated by solely varying the ratio between the diameter of the object and the size of the image. This approach is described in the Methods section 4.3, and results relevant for NMR spectroscopy of cell suspensions and of cell pellets are presented in 5.1.3.

3.1.3. Hindered Molecular Motion and NMR-Visibility

The intracellular situation differs from that within a diluted isotropic solution in many aspects [Luby-Phelps 2000], e.g. regarding macromolecular density and heterogeneity. Against intuition, the intracellular space is substantially crowded. In Fig. 3.1 a manual drawing (true in scale) of the cytoplasm is depicted [Goodsell 2009]. Apart from heterogeneity-induced magnetic B-field distortions, already introduced in section 3.1.2, the crowding leads to a hindered molecular motion, both translational and rotational. The translational hindrance attenuates the apparent diffusion coefficient, whereas rotational restraints change the rate of magnetic B-field fluctuations at the site of the proton. This in turn changes the relaxation rate and thus the resonance linewidth. In the following, this line of thought is explained in more detail. If not referenced additionally, derivations and proofs can be found in standard NMR spectroscopy text books, e.g. [Levitt 2008; Keeler 2005]

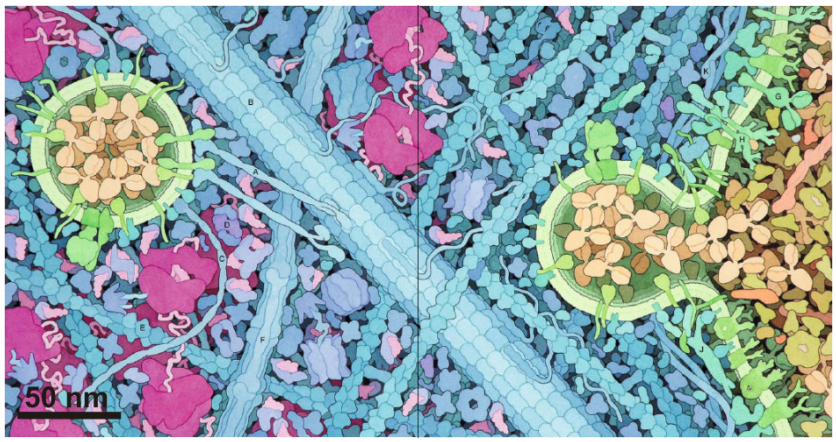

Fig. 3.1 True in scale drawing of molecular crowding inside the cell. Green: Plasma and vesicle membrane, blue strands: actin filaments (thin), intermediate filaments (thicker) and microtubules (thick), brown: antibodies (shuttled in vesicle, left), violet and purple: cytosolic proteins. Copied from **[Goodsell 2009]** and scale bar inserted.

Of course, the linewidth is crucial regarding NMR-visibility. To illustrate this, a broadening of 100 Hz reduces the signal-to-noise ratio (SNR) to about 3 % of the original SNR at typically 3 Hz linewidth. Additionally, the lower resolution complicates identification, discrimination and quantification of resonances.

The linewidth of a single resonance is determined by the time the acquired signal in the temporal space decays to $1/e$ (approximately 37 %) of its initial amplitude. This characteristic time is called T_2^*. Neglecting phenomena like chemical exchange, radiation damping, magnetization transfer, and J-couplings, it is affected by two broadening mechanisms: Homogeneous and inhomogeneous broadenings. Within the term homogeneous broadening, all relaxation mechanisms are summarized. Typical examples of homogeneous broadening effects are T_1- and T_2-relaxation (*vide infra*). In contrast, inhomogeneous line broadenings occur if identical molecules experience different magnetic fields during the acquisition. As a consequence, they resonate at different frequencies, and thus the inhomogeneously shifted sharp resonances sum up to a broadened lineshape. A typical example would be a simple linear magnetic B-field gradient applied during acquisition.

The time-dependent signal of a single resonance of an uncoupled nucleus is given by:

$$S(t) = e^{-\frac{t}{T_2}} \cdot \frac{1}{V} \iiint_V e^{i\gamma B_{\text{nuc, z}}(\vec{r})t}\, d^3r = e^{-\frac{t}{T_2{}^*}} \cdot e^{i\gamma \bar{B}_{\text{nuc, z}}t} \qquad 3.25$$

with the transverse relaxation time T_2, the gyromagnetic ratio γ, the volume of the sample inside the coil V, the nuclear B-field component in the direction of the applied magnetic field $B_{\text{nuc, z}}$, which may dependent on position (see previous section 3.1.2), and its average $\bar{B}_{\text{nuc, z}}$. In other words, the dephasing of the signal due to inhomogeneous fields (inhomogeneous broadening) and the signal attenuation due to transverse relaxation (homogeneous broadening) are incorporated in $T_2{}^*$.

The transverse or spin-spin relaxation time T_2 is influenced by many factors, i.e. by all interactions which enable energy transfer away from the spin bath to the environment (so-called spin-lattice or longitudinal relaxation effects with characteristic time T_1), and additionally by effects causing a loss in coherence, the latter solely affecting T_2 times. Mechanisms for these phenomenons can be e.g. the chemical shift anisotropy, additional paramagnetic species and dipole-dipole interactions [Keeler 2005]. The latter depends strongly on the rotational speed of the molecule. According to the Bloembergen-Purcell-Pound theory (BPP theory) [Bloembergen et al. 1948], the transverse relaxation rate for two dipole-dipole coupled protons gives

$$\frac{1}{T_2} = \frac{3}{320\pi}{\mu_0}^2\hbar^2\gamma^4\frac{1}{r^6}\{3J(0) + 5J(\omega_0) + 2J(2\omega_0)\} \qquad 3.26$$

with the magnetic constant μ_0, the Planck constant $\hbar$, the distance between these two protons r and the normalized spectral density $J(\omega)$ at the frequencies zero, once and twice the Larmor frequency ω_0. Accordingly, the longitudinal relaxation rate can be written as

$$\frac{1}{T_1} = \frac{3}{160\pi}{\mu_0}^2\hbar^2\gamma^4\frac{1}{r^6}\{J(\omega_0) + 4J(2\omega_0)\} \qquad 3.27$$

The normalized spectral density, i.e. the Fourier transform of the normalized auto-correlation function $e^{-\tau/\tau_c}$, denotes

$$J(\omega) = \frac{\tau_c}{1 + \omega^2{\tau_c}^2} \qquad 3.28$$

with the correlation time τ_c, which is roughly the time the molecule rotates about one radian. Inserting Eq. 3.28 in Eq. 3.26, an expression is derived connecting the linewidth with the correlation time. Since $J(0) = \tau_c$, the linewidth increases monotonically with τ_c.

Apart from hindered motion, τ_c depends on the size of a molecule, e.g. according to the spherical approximation of the Stokes-Einstein-Debye equation:

$$\tau_c = \frac{4\pi\eta R^3}{3k_bT} \qquad 3.29$$

with the viscosity η, the hydrodynamic radius of the molecule R, the Boltzmann constant k_b and the temperature T. In other words, τ_c is proportional to the volume of the molecule.

Summarizing the lineshape effect of hindered motion, both the size of molecules and additional rotation attenuations affect the relaxation rates of NMR spectroscopic resonances. Therefore, relaxation-weighted measurements, e.g. by T_2-weighting, enable filtering small, freely tumbling molecules.

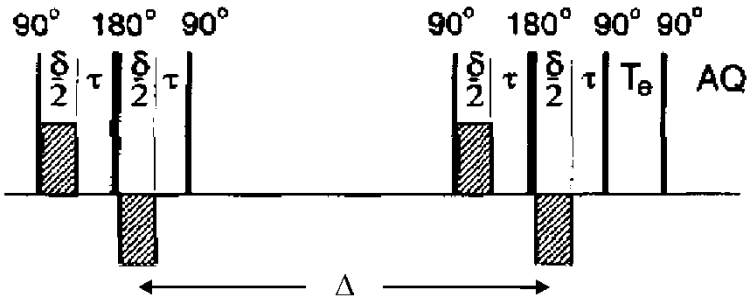

Fig. 3.2 Pulse sequence for diffusion weighting. Stimulated echo with bipolar pulsed-field gradients (shaded) and longitudinal eddy-current delay (T_e). Δ = diffusion time, $\boldsymbol{\delta}$ = gradient duration, $\boldsymbol{\tau}$ = bipolar pulse separation, AQ = acquisition, 90° and 180° refer to hard RF-pulses. Adapted from **[Wu et al. 1995]**

On the other hand, not only a hindered rotational motion, but also attenuations in translational diffusion have an effect on NMR spectroscopy. These differences in diffusion can be addressed by means of diffusion-weighted experiments. Originally established for a spin-echo sequence [Stejskal & Tanner 1965], diffusion-weighting pulsed-field gradient (PFG) experiments are nowadays conducted by means of stimulated-echo sequences with bipolar PFG (BP-PFG) and an additional longitudinal eddy-current delay [Wu et al. 1995]. Briefly, the mechanism of diffusion weighting is as follows: The magnetization, which is deflected to the plane perpendicular to the external field by an initial excitation 90° pulse, is rapidly dephased by a BP-PFG of duration δ. After a so-called diffusion delay Δ including one 180° pulse (spin-echo) or two 90° pulses (stimulated-echo), the magnetization is again rephased by a second BP-PFG. This yields a diffusion-weighted echo signal. The magnetization of molecules which diffuse along the direction of the PFG during the diffusion delay Δ is rephased only partially, because the de- and rephasing effect of the gradients depends on space *per definitionem*. In the isotropic unhindered case, the attenuation of signals from molecules with specific diffusion coefficients can be expressed as [Wu et al. 1995]

$$I(D) = I_0 \cdot e^{-\gamma^2 g^2 \delta^2 (\Delta - \delta/3 - \tau/2) D} \qquad 3.30$$

with the signal intensity with and without diffusion weighting $I(D)$ and I_0, respectively, with gyromagnetic ratio γ, gradient strength g, gradient duration δ, diffusion time Δ, bipolar-pulse separation τ and diffusion coefficient D. Obviously, by carefully adjusting the value of $g^2\delta^2(\Delta - \delta/3 - \tau/2)$, known as b-value, it is possible to edit NMR spectra such that signals of molecules with high diffusion coefficients are heavily attenuated, e.g. beyond the noise level, whereas resonances of slowly diffusing molecules are virtually not affected.

In case of inhomogeneously hindered diffusion, the situation is more complex. For extracellular molecules it is assumed that the apparent diffusion coefficient (ADC), i.e. the coefficient extracted by fitting Eq. 3.30 to the increasingly diffusion-weighted spectra, is solely scaled down by the so-called turtuosity λ such that $ADC = D/\lambda^2$ [C. Nicholson & Phillips 1981]. The turtuosity includes the detours caused by obstacles, i.e. the cells. Thus the ADC is always smaller than in pure solution.

For molecules restricted in diffusion within boundaries, the Tanner model [Tanner & Stejskal 1968] yields an attenuation behavior that cannot be described by the function in Eq. 3.30 anymore. In this case, an evaluation on the basis of Eq. 3.30 would give an ADC that would depend intrinsically on the diffusion time Δ. A detailed description of restricted diffusion can be found e.g. in a publication by Pfeuffer *et al.* [Pfeuffer et al. 1998]. Moreover, non-specific adsorption and desorption, specific binding, the relative and absolute dimensions of the aqeuous phase and intervening immobile structures, cytoplasmic streaming, inhomogeneous viscosity distributions etc. (clearly reviewed by Nicolay *et al.* [Nicolay et al. 2001]) argue against a simple diffusion model for the intracellular space.

Nevertheless, diffusion-weighting has already been applied in order to discriminate between NMR spectral signals of molecules from intra- and extracellular compartments [Van Zijl et al. 1991].

3.1.4. NMR-Visible Mobile Lipids and Mobile Proteins

Mobile lipids are called “mobile”, because they are mobile enough to be NMR-visible. This phenomenon constitutes a great exception – at least in cells and tissues – since cells are surrounded by and filled with lipid membranes that are virtually invisible for NMR spectroscopy [Hakumäki & Kauppinen 2000]. Only this subfraction of lipids can be detected by NMR spectroscopy on cell suspensions and by *in vivo* NMR spectroscopy. Synchroneously with the NMR spectroscopic appearance of mobile lipid resonances, cytoplasmic lipid droplets become detectable by immunocytochemical methods, e.g. lipid staining followed by fluorescent microscopy [Al-Saffar et al. 2002; Barba et al. 1999; Ferretti et al. 1999; Quintero et al. 2007]. Interestingly, not all cells show these mobile lipid resonances. To date, the underlying mechanisms and the biological significance of cytosolic lipid accumulations have not been clarified in total yet, but several conditions favoring mobile lipid appearance are already established.

Some of the seminal published results about mobile lipids concerning cellular NMR spectroscopy are summarized in the following paragraph:

Cell types that exhibited mobile lipids were: Macrophages [N. J. King et al. 1994], lymphocytes [Veale et al. 1997], neutrophils [May et al. 1994], 3T3 fibroblasts [Ferretti et al. 1999], Jurkat T-cells [Al-Saffar et al. 2002], C6 glioma cells [Barba et al. 1999], HeLa cervical cancer cells [Grande et al. 2001], prostate cancer cells [Milkevitch et al. 2005], lymphoma cells [Blankenberg et al. 1997], MG-63 osteosarcoma cells [Santini et al. 2006], breast cancer cells [Le Moyec et al. 1992], myeloma cells [Callies et al. 1993], K562 erythroleukaemic cells [Le Moyec et al. 2000], etc.

Conditions and properties that favored mobile lipid formation were: Proliferation [Barba et al. 1999], drug resistance [Ferretti et al. 2003; Le Moyec et al. 2000], ability to metastasize

[Mountford & Tattersall 1987], cell culture confluence [Barba et al. 2001; Delikatny, Lander et al. 1996; Quintero et al. 2007], growth retardation [Barba et al. 1999], inflammation [May et al. 1994; N. J. King et al. 1994], apoptosis [Al-Saffar et al. 2002; Blankenberg et al. 1996; Blankenberg et al. 1997; Brisdelli et al. 2003; Di Vito et al. 2001; Iorio et al. 2003; Lehtimäki et al. 2003; Milkevitch et al. 2005; J. E. Schmitz et al. 2005], necrosis [Mirbahai et al. 2010], growth arrest [Barba et al. 2001; Quintero et al. 2007], pH-stress [Barba et al. 2001], cytotoxic insult [Mountford & Tattersall 1987; Delikatny, Roman et al. 1996; Roman et al. 1997], chemotherapy [Delikatny et al. 2002], cell seeding [Quintero et al. 2007], inhibition of DNA-synthesis and replication [Mikhailenko et al. 2005], radiation [Grande et al. 2006; Luciani et al. 2002; Santini et al. 2006], growth factor deprivation [Quintero et al. 2007], etc.

Almost all publications about NMR-visible mobile lipids indicate that two requirements are needed for mobile lipid formation: the ability to proliferate and a condition associated with cellular stress. Both items are of special interest for oncology, because a non-invasive marker for stressed proliferative cells could constitute a new read-out for efficacy of tumor therapies. Therefore, in many groups publishing on mobile lipids the focus was on establishing mobile lipid resonances as surrogate markers for early stages of apoptosis [Lehtimäki et al. 2003] and not, e.g., necrosis. But the nature of NMR-visible lipid formation seems to be more complex [Brisdelli et al. 2003; Ferretti et al. 2003; Quintero et al. 2010; Santini et al. 2006], maybe being the reason why mobile lipids have not been established as apoptosis markers for therapeutic response in the clinic yet.

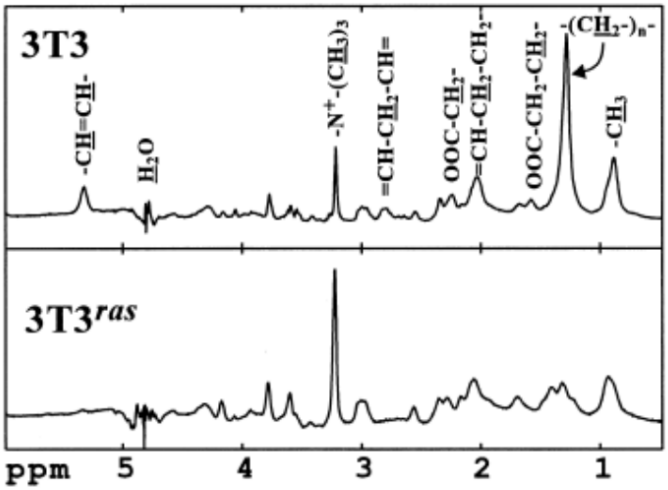

Fig. 3.3 Typical NMR spectra of cell suspensions with and without mobile lipid resonances. (Top) Spectrum showing predominant mobile lipid signals, resonating lipid moieties are assigned. **(Bottom)** Spectrum lacking mobile lipid peaks. The residual broad peaks, i.e. mobile proteins, are different in lineshape and chemical shift position than those of mobile lipids, and show strong consistency to non-lipid macromolecular peaks in other cell suspension NMR spectra. Cells: NIH-3T3 fibroblasts (top) and *ras*-transformants. Spectra copied from Knijn *et al.* **[Knijn et al. 1997]**.

Fig. 3.3 (top) shows a typical cell suspension NMR spectra containing mobile lipid signals [Knijn et al. 1997]. The lipid moieties were assigned to the corresponding resonances.

In contrast, in Fig. 3.3 (bottom) an NMR spectrum is depicted without mobile lipid signals. The absence of mobile lipids could be clarified not only by the typical lineshapes, but also by additional two-dimensional correlation spectra (COSY) [Le Moyec et al. 1992]. Instead, the broad signals in this spectra are caused by another group of NMR-visible macromolecules: **mobile proteins**. Compared to the literature concerning mobile lipids, mobile proteins are discussed very rarely [Behar et al. 1994; Behar & Ogino 1991; Behar & Ogino 1993; Kauppinen et al. 1992; Kauppinen et al. 1992; Kauppinen et al. 1993; Kauppinen & Palvimo 1992], and in the majority of cases they are treated as baseline artefacts that should be subtracted accurately to yield proper quantifications of the overlapping metabolites [Opstad

et al. 2008b]. The identity of the underlying proteins giving rise to mobile protein signals is not clarified in detail yet, although there is evidence that these proteins are at least partially unfolded and acid-extractable [Kauppinen et al. 1993]. This finding fits well to the fact that the chemical shifts of mobile proteins resemble those obtained by random coil peptides [Wishart et al. 1995], which are unfolded as defined.

Proposed protein candidates for major contributions to mobile protein resonances are e.g. thymosin β4 and histone H1 [Kauppinen et al. 1993; Kauppinen et al. 1992; Kauppinen & Palvimo 1992], which play key roles in cytoskeleton formation and DNA replication, respectively. Changes in these two processes could possibly be associated to proliferative activity. Therefore, also mobile proteins might be interesting for read-out of proliferative status of cells. However, the underlying mechanisms as well as possible changes in mobile protein signals are even less clear than those of mobile lipids.

3.1.5. Low Density Lipoproteins

Low density lipoproteins (LDL) constitute an interesting model system for the NMR-visibility of lipids, since their structure is understood in more detail: LDL, the major carriers of cholesterol within the blood circulation, consist of a hydrophobic core of lipids surrounded by an amphiphilic monolayer. With an average diameter of 22 nm, they contain about 1600 cholesteryl esters, 170 triglycerides, 700 phospholipids, 600 free cholesterol molecules, and one single protein, i.e. apoB-100 [Hevonoja et al. 2000]. Between 20° C (LDL-subfraction with largest LDL particles) and 30° C (smallest LDL), the core undergoes a phase transition [Baumstark et al. 1990]. At low temperatures, the cholesteryl ester molecules are ordered in a liquid-crystalline phase [Prassl & Laggner 2008]. In contrast, above the phase transition temperature, the LDL core resembles a fluid, oil-like phase. A schematic drawing of these two structures based on X-ray small angle scattering experiments [Baumstark et al. 1990] was published by Hevenoja *et al.* [Hevonoja et al. 2000] and is depicted in Fig. 3.4.

Lipoproteins can be structurally modified by oxidation or by enzymatic degradation [Grandl et al. 2006]. In contrast to native low-density lipoproteins (LDL) and mildly oxidized LDL (Ox-LDL), enzymatically degraded LDL (E-LDL) do not exhibit a significant core of neutral lipids in an oil-like, fluid phase. Instead, E-LDL are arranged in a multilamellar liposome-like fashion [Chao et al. 1992; G. Schmitz & Grandl 2009]. In other words, whereas above the phase transition temperature, native LDL and Ox-LDL are dominated by reasonably free-floating neutral lipids, E-LDL mainly consist of an “onion-like” formation of membrane compounds, as unveiled by electron microscopy [Chao et al. 1992] (see Fig. 3.5). Moreover, the degradation of LDL to E-LDL, i.e. a protein degradation by trypsin and a subsequent hydrolysis by cholesterol esterase, results in a large shift in molecular composition from large percentages of cholesteryl esters (*vide supra*) to mainly unesterified cholesterol [Hevonoja et al. 2000].

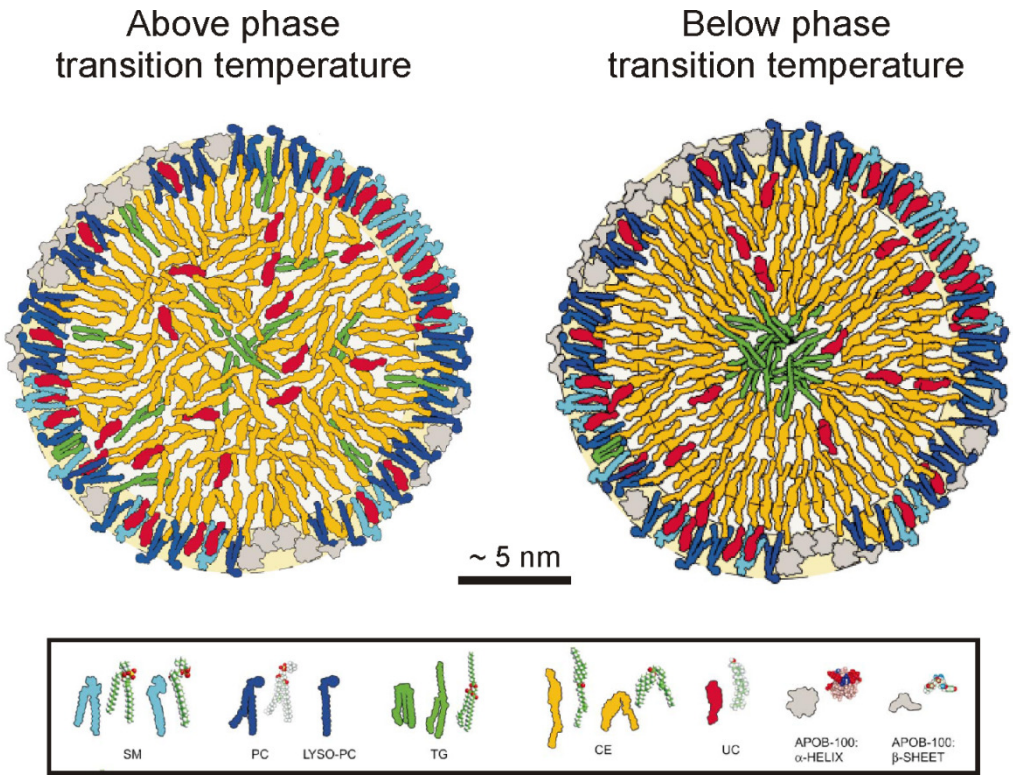

Fig. 3.4 Structural phase transition of low density lipoproteins (LDL). CE = cholesteryl ester, UC = unesterified cholesterol, TG = triglyceride, PC = phospholipid, SM = sphingomyelin. Adapted from **[Hevonoja et al. 2000]**.

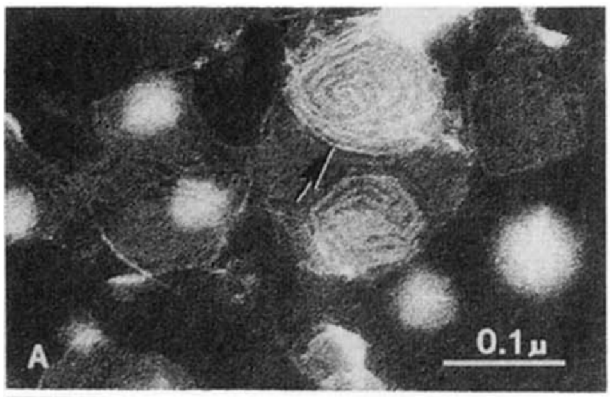

Fig. 3.5 Electron micrograph of multilamellar structure of LDL treated with trypsin an cholesterol esterase. Copied from **[Chao et al. 1992]**.

When macrophages are loaded with enzymatically degraded LDL (E-LDL), they show an increased formation of cytoplasmic lipid droplets [G. Schmitz & Grandl 2009], which results in a conversion of the macrophages to so-called foam cells [Kapinsky et al. 2001]. During phagocytosis, the free cholesterol molecules of E-LDL are reesterified to cholesteryl esters and subsequently stored in lipid bodies. Due to this structural reorganization of multilamellar E-LDL to oil-like droplets, also the NMR-visibility of E-LDL-associated lipids is likely to change during internalization by macrophages.

In vivo, macrophage foam cells play a major role in atherosclerosis [G. Schmitz & Grandl 2009]. Therefore, foam cell formation by loading with E-LDL constitutes a well-defined model to investigate mechanisms that lead to atherosclerotic lesions.

3.2. Brain-Derived Stem Cells

Neural progenitor cells (NPC) and brain tumor-initiating cells (BTIC), herein called brain-derived stem cells, both constitute cutting-edge areas of research. As already mentioned in the introduction, great expectations rose on NMR spectroscopy to identify NPC- or BTIC-specific biomarkers. These could be utilized to detect neurogenesis and tumorigenesis, i.e. the formation of new neurons and tumor cells, respectively, *in vivo* in humans non-invasively. Furthermore, unveiling metabolic peculiarities in these cells, e.g. upon specific drug treatments, by NMR spectroscopy would constitute a benefit exceeding that of a pure diagnosis and monitoring tool by far.

In the following, a short overview is given on biological aspects of NPC and BTIC whose knowledge are crucial for the comprehension of this dissertation and its intentions. Since this doctoral thesis constitutes a biophysics work written by a physicist, the reader is also referred to more detailed and balanced reviews, e.g. written by Lie *et al.* [Lie et al. 2004] and by Vescovi *et al.* [Vescovi et al. 2006] addressing NPC and BTIC, respectively, and by Reya *et al.* [Reya et al. 2001] for a more fundamental and illustrative approach to the stem cell hypothesis.

At the end of this section, some major findings are summarized regarding the transforming growth factor TGF-β treatment and its implications on NPC and BTIC. This overview is based on the review of Aigner and Bogdahn [Aigner & Bogdahn 2008].

All statements in this chapter are adopted from seminal reviews on these areas of research (references *vide infra*), and are therefore not referenced to their original science reports, which would be beyond the scope of this introducing overview. All direct citations can be found within the reviews mentioned above.

3.2.1. Neural Progenitor Cells

Today it is common knowledge that the formation of new functional neurons continues also in human adulthood, although the rate and relevance of this process cannot yet be compared to that in other organs, e.g. blood or skin. In addition, adult neurogenesis is probably focussed mainly to two distinct regions in the brain: the subventricular zone (SVZ) of the lateral ventricles and the dentate gyrus of the hippocampus. From the SVZ, immature cells migrate towards the olfactory bulb to maturate and integrate there into the neuronal network. In contrast, within the hippocampus, the migration distance of the newborn cells is negligible, i.e. they replace neurons within the hippocampus. At both locations neurogenesis seems to be fundamental, and alterations in neurogenesis have been described for the majority of neurodegenerative diseases (e.g. Alzheimer's disease, Parkinson's disease, Huntington's disease, amyotrophic lateral sclerosis (ALS)) and in other clinical pictures like ischemia, multiple sclerosis, bipolar disorders, depression etc.

Two major hallmarks exist for the definition of stem cells: First, the ability of quasi-infinite selfrenewal, i.e. the ability to divide asymmetrically and thus always create an identical daughter cell that keeps stem cell characteristics and a more differentiated progenitor cell.

Second, the capacity to differentiate into different cell types. For a neural stem cell, this differentiation cascade is depicted in Fig. 3.6. Quiescent neural stem cells can give rise to rapidly dividing neural progenitor cells, which in turn are able to differentiate into the glial or the neuronal lineage. Within these lineages they mature via lineage-restricted progenitor cells, i.e. oligodendrocyte progenitors (OPC), astrocyte progenitors, and neuroblasts (immature neurons) to mature, postmitotic and functional oligodendrocytes, astrocytes and neurons, respectively.

In addition to the definition of stem cells, lineage- and stage-specific surrogate markers have been established, e.g. cytoplasmic proteins (Sox2 for neural stem cells, Nestin for neural progenitor cells, DCX for neuroblasts etc.), whose genetic promoters can be used and modified such that whenever these specific proteins are expressed, also additional reporter proteins, e.g. fluorescent proteins, are synthesized. These reporter proteins enable cell-specific microscopy and imaging *in vivo*. However, a non-invasive method to detect and track neural stem/ progenitor cells *in vivo* in humans has not been established yet, but is heavily sought for.

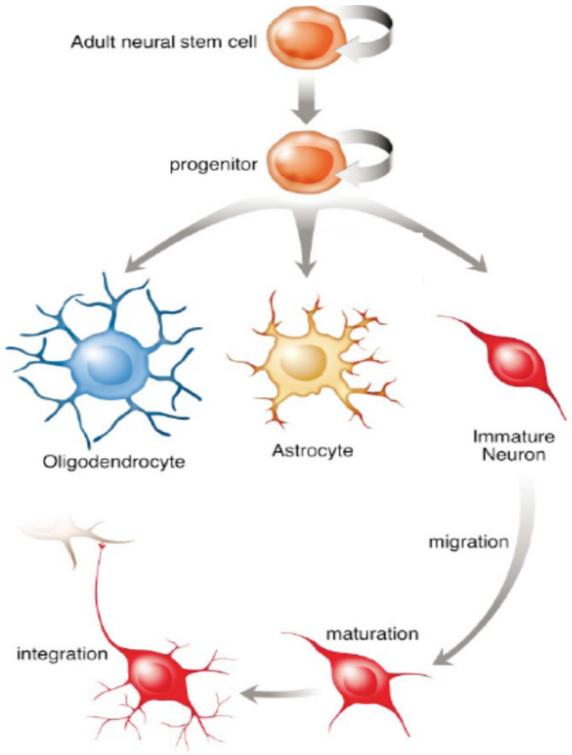

Fig. 3.6 The differentiation tree of neural stem cells. Modified after Lie *et al.* **[Lie et al. 2004]**. Adult neural stem cells give rise to transient amplifying neural progenitors that differentiate to either the glial or the neuronal lineage. Within the glial lineage they maturate to oligodendrocytes or astrocytes, whereas within the neuronal lineage they become neuroblasts, i.e. migrating immature neurons, which maturate to post-mitotic functional neurons and either integrate into the neuronal circuit or undergo apoptosis.

3.2.2. Brain Tumor Initiating Cells

In brain tumors, e.g. glioblastoma multiforme (GBM), brain tumor-initiating cells (BTIC) constitute the putative analogue to neural progenitor cells (NPC) in the neurogenic regions of the brain. The hypothesis reads that a subpopulation of distinct initiating cells with typical stem cell characteristics serves as source of cell replacement for the growing tumor mass.

However, in contrast to NPC, the hypothesis of cancer stem cells (CSC), also known as brain tumor stem cells, brain tumor propagating cells, glioblastoma (GBM) initiating cells, or – more tentatively – brain tumor-initiating cells (BTIC), has not been fully accepted yet. Nevertheless, beyond doubt there are GBM-derived cells which in contrast to conventional GBM cell lines are able to grow in medium without growth factor containing serum. Furthermore, these cells are able to form clones from single cell seedings, but can also be forced to "differentiate" to cells with different phenotypes. In addition, this subpopulation of cells is less sensitive to chemotherapy and radiation therapy. As an ultimate proof of stemness, these cells can be transplanted orthotropically and then give rise to tumors phenotypically identical to the tumor of origin. Interestingly, transplanted GBM tumor cells (GBM-TC), which were depleted of BTIC do not give rise to aggressive tumors.

In Fig. 3.7 two contradictory models of tumor initiation are contrasted. The stochastic model is preferred by researchers expressing the view that there are no stem cell-like cells within the tumor. In this model almost all cells of the heterogeneous cell type mixture within the tumor are capable of initiating new tumors by e.g. de-differentiation, cell fusion, horizontal gene transfer etc. In contrast, supporters of the hierarchical model assume that a small subpopulation of tumor cells is responsible for tumor initiation and progression. Even among the tumor stem cell community, it is discussed controversially if these brain tumor-initiating cells (BTIC) might be transformed progenies of physiological neural stem cells. In other words, maybe every tumor cell could be traced back to a transformed neural stem cell.

Brain tumor-initiating cells (BTIC) are gained quasi-routineously by treating glioblastoma-derived primary cells similarly to e.g. fetal forebrain-derived cells cultured in order to yield neural progenitor cells (NPC). That is, in contrast to most other cell culturing methods, without any kind of serum, e.g. fetal calf serum (FCS). Instead, special stem cell medium supplements and growth factors, e.g. epidermal growth factor (EGF) and fibroblast growth factor (FGF) are used. The same glioblastoma specimen would give a differentiated tumor cell line (herein named GBM-TC) if cultured in medium containing serum on the one hand, and a BTIC line if grown in neural stem cell medium without serum on the other hand.

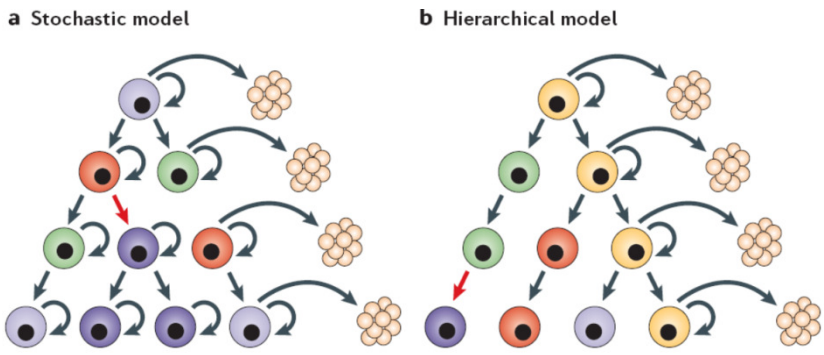

Fig. 3.7 Comparison of different models of tumor initiation. (a) The stochastic model proposing every cell to be a potential source of tumor initiation, possibly through transformation, de-differentiation, cell fusion etc. **(b)** The hierarchical model attributing the tumor initiation potential solely to a small subset of tumor cells, i.e. BTIC (yellow). Image copied from Vescovi *et al.* **[Vescovi et al. 2006]**.

In contrast to e.g. Nestin for neural progenitor cells (NPC), there have not been any established and widely accepted markers for tumor-initiating cells yet. Proposed surface markers, especially CD133, were found to identify cells exhibiting some major criterions of brain tumor-initiating cells (BTIC). However, more recently, also CD133 negative cells proved to generate NPC- and BTIC-typical neurospheres (round, floating cell clusters) *in vitro* and solid brain tumors after transplantation *in vivo* [C. P. Beier & D. Beier 2011] . Nevertheless,

CD133 is a marker worth including in the portfolio of BTIC characterization. In contrast, established methods to quantify stemness within a BTIC line exist. *In vitro* these are single cell clone-forming assays, also named clonogenicity tests. A very time consuming but ultimate verification of stem cell characteristics constitutes serial transplantation studies *in vivo*, in which a cell type may proof its capacitiy for both self-renewal and tumor initiation within its natural environment.

3.2.3. Transforming Growth Factor β

In Results section 5.2.2, the changes in NMR spectra of neural progenitor cells (NPC), glioblastoma-derived tumor cells (GBM-TC) and brain tumor-initiating cells (BTIC) upon treatment with transforming growth factor β (TGF-β) are presented. Therefore, in the following section a short introduction based on the review of Aigner and Bogdahn [Aigner & Bogdahn 2008] is given.

TGF-β molecules belong to a small group of multifunctional cytokines of the TGF-β superfamily. All three isoforms, i.e. TGF-β1, TGF-β2, and TGF-β3, are expressed within the nervous system, however, TGF-β2 and TGF-β3 are found ubiquitously, whereas TGF-β1 is predominantly upregulated after brain lesions, upon neurodegeneration and in brain tumors. In general, TGF-β has opposite effects on tumors and on non-tumoral brain tissue. In the latter case, TGF-β is neuroprotective in that it limits inflammation, suppresses microglia activation as well as proliferation, and inhibits NPC proliferation through an enhanced arrest in cell cycle G_0/G_1 phase without changing the NPC identity or differentiation potential, and without increasing apoptosis. In contrast, these partially tumor-suppressing properties of TGF-β transform to oncogenic characteristics in the case of malignant gliomas or many other solid malignancies. Somehow, the tumor cells escape from the cytostatic response to TGF-β, but maintain the TGF-β signaling pathway intact, thus promoting an autocrine loop of growth stimulation, which leads to an enhanced proliferation. In brain tumors, TGF-β is considered a key mediator for tissue invasion, metastasis, tumor angiogenesis, escape from immune attack, and Epithelial to Mesenchymal Transition (EMT). So far the main source of tumor-associated TGF-ß was thought to be the tumor cells, but more recently so called myeloid derived suppressor cells invading the tumor tissue probably contribute at least as much active TGF-ß. With respect to this tumor progression promoting effects of TGF-β, antisense molecules targeting TGF-β receptor expression and thus downregulating TGF-β signaling in tumors are currently tested in clinical trials.

Unpublished observations by Praveen Kumar and Christoph Beier, former members of our group, indicate that both the expression of TGF-β and the susceptibility to TGF-β treatment are very inhomogeneous among different cultured brain tumor-initiating cell lines (BTIC).

3.3. NMR Spectroscopy of Neural Progenitor Cells

Since the number of groups publishing on NMR spectroscopy of neural progenitor cells (NPC) is rather low, a more detailed insight into their findings can be given.

In the early 1990's, Urenjak *et al.* [Urenjak et al. 1993] published that N-acetyl-aspartate (NAA), which was previously thought to be specific for mature neurons, can also be found in NMR spectra of perchloric-acid extracts of immature oligodendrocytes and of oligodendrocyte-type-2 astrocyte progenitor cells (O-2A progenitors). The NAA content in O-2A progenitors was even twice as high as in neurons. Moreover, they could define metabolites for each of the five investigated neural cell types (neurons, astrocytes, O-2A progenitors, oligodendrocytes, meningeal cells) that allowed discrimination between these cell types. In the case of O-2A progenitors, the NAA content was at least one order of magnitude higher than in astrocytes, oligodendrocytes and meningeal cells, whereas hypo-taurine was minimum one order of magnitude higher than in neurons. Besides that, O-2A progenitors were characterized by very low or vanishing values of β-hydroxybutyrate and taurine.

Almost ten years later, Griffin *et al.* [Griffin et al. 2002] employed magic angle spinning NMR spectroscopy on whole cells to distinguish between cerebellar granular neurons, astrocytes and again O-2A progenitors. The latter showed the highest levels of glycine and lactate and low amounts of NMR-visible macromolecules, which at that time were solely assigned to lipids. Especially the glycine-macromolecular ratio allowed discrimination of O-2A progenitors from neurons and astrocytes.

In 2006, Jansen *et al.* [Jansen et al. 2006] reported on differences in NMR spectra of perchloric-acid extracts of embryonic stem cells (ESC) and neural stem cells (NSC) differentiated from ESC. To discriminate between these two stem cell types, significant changes in phosphocholine (PCho) and creatine (Cre) upon differentiation could be used. The authors also compared their findings to that of other groups and discovered e.g. the highest amounts of PCho and glycerophosphocholine (GPC) in their stem cells compared to neurons, Schwann cells and a couple of tumor cells. Especially NSC constituted remarkable outliers with respect to their high GPC, myo-inositol (m-Ino) and Cre contents, whereas an even higher amount of PCho in ESC tempted the authors to a possible explanation: Elevated expression of two enzymes in choline metabolism, i.e. choline kinase processing free choline to PCho, and phospholipase C degrading membrane phosphatidylcholine to PCho, would lead to an increased PCho accumulation.

Causing great attention in the field of neural stem cell and neurogenesis biology, in 2007 Manganas *et al.* [Manganas et al. 2007] claimed to have found an NMR-spectroscopic biomarker specific for NPC, which could also be used for detection of transplanted NPC in rat brain, and for quantification of hippocampal neurogenesis in humans (Fig. 3.8). Because of the non-detectability of this biomarker *in vivo* by conventional spectral processing, i.e. Fourier transform, the authors supplied an evaluation method based on iterative singular value decomposition (SVD) and filtering of the biomarker from neighboring signals. In 2008

three comments were published, again in *Science* [Friedman 2008; Hoch et al. 2008; Jansen et al. 2008], all expressing violent doubts about the unconventional processing, post-processing and evaluation methodology. Two of them [Friedman 2008; Jansen et al. 2008] also questioned the nature of the 1.28 ppm peak and the ability to discriminate between this signal and e.g. mobile lipids. In parallel, we investigated the appearance and specificity of this biomarker peak in more detail and published our doubts in 2009 [Ramm et al. 2009]. Part of this study is presented in the Results chapter, section 5.2.1. Later that year, Dong *et al.* [Z. Dong et al. 2009] rounded off the comments on Manganas' findings by addressing the missing robustness of the SVD-based evaluation method in case of low signal-to-noise ratios (SNR).

Recently, Ma *et al.*, affiliated to the group of Maletic-Savatic like Manganas, reinforced their argumentation by publishing their protocol of NPC detection [Ma et al. 2011].

Concluding the current state of research in the field of NMR spectroscopy of neural progenitor cells, some differences to mature neural cells have been found *in vitro*, especially in the metabolites associated with membrane synthesis and breakdown, e.g. choline compounds. However, the underlying mechanisms as well as the reproducibility in other groups and with other cell lines still have to be elucitated. In case of *in vivo* detection of NPC by specific NMR spectroscopic biomarkers, convincing reproducable findings are missing.

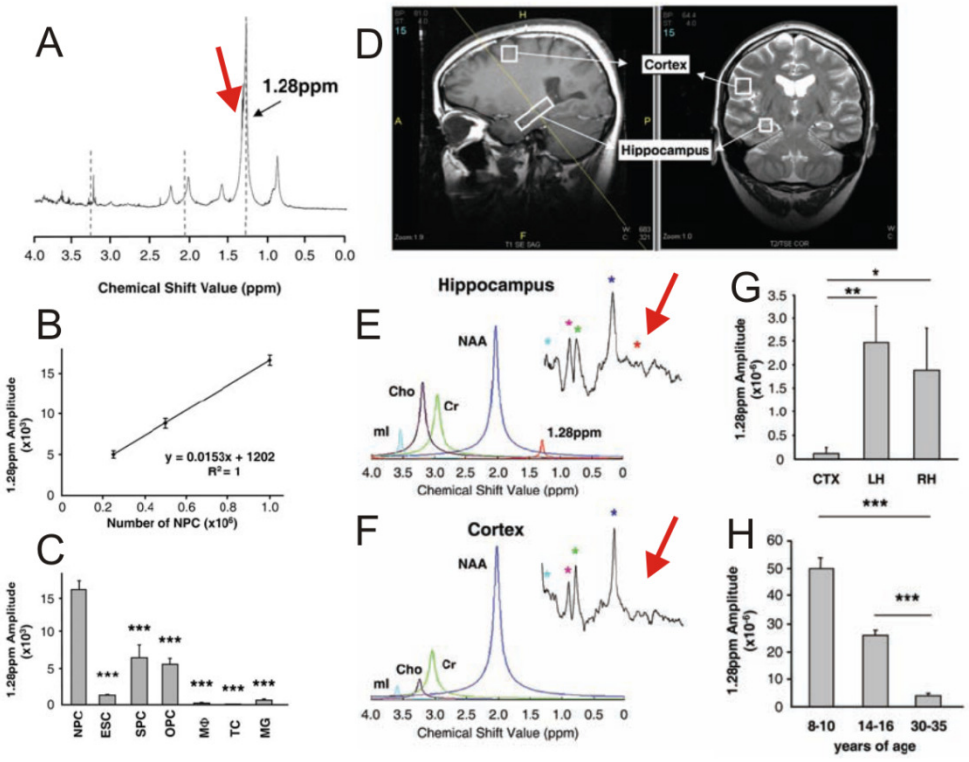

Fig. 3.8 NPC-specific NMR-spectral biomarker, as published by Manganas *et al.* [Manganas et al. 2007] (A) *In vitro* NMR spectrum of cultured NPC. The proposed biomarker at 1.28 ppm is highlighted by a red arrow. **(B)** Dependence of the biomarker from the number of cells investigated. **(C)** Comparison of the biomarker amplitude in NPC to other cells (embryonic stem cells, ESC, hair follicle-derived sphere cultures, SPC, oligodendrocyte progenitor cells, OPC, macrophages, MΦ, T lymphocytes, TC, microglia, MG). **(D)** Voxel location for *in* vivo single voxel spectroscopy (SVS) in a healthy human being. **(E+F)** Intensely post-processed NMR data of voxels containing the hippocampus and the cortex, respectively. Insets: Corresponding Fourier-transformed SVS NMR spectra. Red arrows at biomarker resonances. **(G)** Quantified biomarker in voxels containing cortex (CTX), left (LH) and right (RH) hippocampus. **(H)** Amplitude of the biomarker broken down to three different age groups. All figures copied from **[Manganas et al. 2007]**, rearranged and partially highlighted.

4. Methods

In the following chapter, the methods are described which were employed to yield the results presented in chapter 5. After a short introduction to cell culture and biological assay methodology, the simulation routine to determine susceptibility-induced magnetic B-field distortions according to the theory explained in section 3.1.2 is described. Subsequently, the technical equipment of the employed NMR spectrometers, used pulse sequences, and applied acquisition parameters as well as processing schemes are listed. The description of the quantification strategy of mobile lipids is followed by remarks on the statistical evaluations, especially on the application of principal component analyses and correlation analyses.

4.1. Cell Culture and Biological Assays

Neural progenitor cell (NPC) culture was conducted as described by Karl *et al.* [Karl et al. 2005] and by Wachs *et al.* [Wachs et al. 2003]. Briefly, murine fetal forebrains or rat adult hippocampus/ subventricular zones were dissected, chopped and resuspended in neurosphere medium (Neurobasal, Invitrogen, USA) containing stem cell supplement (B27, Gibco, Invitrogen, USA) and growth factors (epidermal growth factor, fibroblast growth factor). Starvation of the cells was prevented by regular medium changes. After five days in culture, cells were harvested, washed with phosphate-buffered saline (PBS), singulated by enzymatic digestion of extracellular cell-adhesions (e.g. with trypsin or accutase) and resuspended in fresh medium. For elongated cell culture period studies, 8, 11 or 14 days elapsed until harvesting. For apoptosis induction, 50 – 100 µM Menadion (Sigma Aldrich, Germany) was added for five hours at culture day 5. In the case of TGF-β treatment, the medium contained 10 ng/ml = 0.4 nM TGF-β 1 (R&D Systems, USA) throughout the culturing period.

Commercially available african green monkey kidney fibroblast cell lines COS7 (American Type Culture Collection, USA) were cultured as described by Couillard-Després *et al.* [Couillard-Despres et al. 2004]. In case of rodent bone marrow-derived mesenchymal stem cells (MSC), the cell culture protocol published by Rivera *et al.* [Rivera et al. 2006] was adhered to. For apoptosis induction, 25 µM Menadion was added for 18 hours at control conditions to both COS7 and MSC cultures.

Three different immortalized human glioblastoma-derived tumor cell lines (GBM-TC), namely the commercially available cell line U87 (American Type Culture Collection, USA) and the on-site established cell lines HTZ-349 and HTZ-417 [Bogdahn et al. 1989], were cultured in medium containing fetal calf serum as described by Arslan *et al.* [Arslan et al. 2007] until

de visu post-confluence. In case of TGF-β treatment, the culture medium contained 0.4 nM TGF-β 1 or TGF-β 2, respectively.

Ten different on-site established human glioblastoma-derived brain tumor-initiating cell lines (BTIC) were cultured without addition of any serum, as described by Beier *et al*. [D. Beier et al. 2007]. TGF-β treatment was conducted the same way as for GBM-TC cultures.

Macrophage isolation and cell culture, as well as LDL isolation and modifications, were conducted by Dr. Margot Grandl, a former fellow of the Institute of Clinical Medicine of Prof. Schmitz, University of Regensburg [Grandl et al. 2006]. Briefly, human macrophages were derived from monocytes, which had been isolated by leukapheresis followed by counterflow elutriation. Phagocytic differentiation of monocytes to macrophages was conducted by culturing monocytes in macrophage serum-free medium (Invitrogen, Germany) with monocyte-colony stimulating factor (M-CSF, 50 ng/ml, R&D Systems, USA). After four days, macrophages were loaded with LDL-species for 48 hours followed by harvesting.

In addition to native low-density lipoproteins (LDL, 1.006 mg/ml – 1.063 mg/ml), enzymatically modified LDL (E-LDL, 40 µg/ml) and mildly oxidized LDL (Ox-LDL, 80 µg/ml) were used for LDL-loadings of macrophages. In case of E-LDL, LDL were treated with 6.6 µg/ml trypsin (Sigma, Germany) and 40 µg/ml cholesterylester hydrolase (Roche, Germany). Oxidation of LDL was conducted by dialyzation against 5 µM copper(II) sulfate followed by sterile filtration.

Fluorescent flow cytometry was employed to determine the cell cycle S-phase (DNA-binding DAPI), the percentage of viable cells (propidium iodide and annexin), and the percentage of CD133-positive cells (CD133 antibody), as decribed by Vollmann-Zwerenz *et al.* [Vollmann-Zwerenz et al. 2010] or Beier *et al.*[D. Beier et al. 2007].

Apart from flow cytometry, cell viability was further tested by a lactate dehydrogenase (LDH) assay (Promega, USA) or by counting stained vs. unstained cells in a Trypan-blue exclusion assay.

To determine the clonogenicity of the BTIC lines, single cell suspensions were seeded at a density of 10 cells per well in 96 well plates and numbers of free floating or adherent spheres were determined after 21-28 days.

4.2. Sample Preparation for NMR Spectroscopy

For NMR spectroscopy, 3 – 10 million cells (depending on the cell type-specific cell volume) were harvested from the cell culture flasks. In case of adherent cells, trypsin or accutase was used to detach the cells from the flask bottom. The harvested cells were centrifuged at 120 rcf, and the resulting cell pellet was resuspended in ca. 1 ml medium and transferred on ice to the NMR spectrometer site. For delayed spectroscopic measurements, 10 %

dimethyl-d6 sulfoxide (DMSO) was added to the resuspended cell pellet, and the suspension was slowly cooled down to -80° C, transferred on dry ice to the NMR spectrometer site, and stored at < -32° C until further processing. Prior to NMR spectroscopy, the frozen sample was thawed rapidly in a 37° C water bath. Both frozen and unfrozen samples were washed quickly twice by centrifugation at 350 rcf for five minutes at room temperature. The supernatant was discarded and the cell pellet was resuspended in 1 ml phosphate buffered saline (PBS).

In case of agarose embedding method, the final cell pellets were resuspended at 37° C in 200 µl – 600 µl liquid 1 % ultralow gelling point agarose (Sigma Aldrich, Germany) in PBS containing 10 % deuterium oxide (D_2O) and 40 µM dimethyl-silapentane-sulfonate (DSS). Depending on the cell pellet size, the agarose cell mixture was transferred either into a standard 5 mm NMR tube (600 µl, tube type 507, Norell Inc., USA) or into a 4.2 mm tube (400 µl, Hilgenberg, Germany) or into a 4.2 mm tube as three-layer design, i.e. 100 µl pure agarose below and above 200 µl agarose cell mixture. Subsequently, the sample was held in ice water for approximately 30 s for agarose gelling.

In case of sedimentation methods, the pellet was resuspended in 60 µl – 500 µl PBS containing at least 10 % D_2O and 40 µM DSS. The suspension was transferred either into a Shigemi 5 mm NMR tube with susceptibility-matched solid glass bottom (500 µl, Shigemi, USA) or into one of the in-house modified 1 – 2 mm tubes (ca. 60 µl – 150 µl). For the latter hollow plugs of Shigemi 5 mm NMR tubes were pruned manually such that the bottom of the plug cavity fit the lower edge of the sensitive coil volume.

The resulting suspension volumes within the sensitive coil area were approximately 200 µl for 5 mm tubes, 150 µl for 4.2 mm tubes, and 13 µl – 50 µl for modified Shigemi plugs with inner diameter of 1 mm – 2 mm.

4.3. Simulation of Susceptibility-Induced Magnetic B-Field Distortions

The simulation of field distortions was performed according to the fast Fourier-transformation method described in 3.1.1. Briefly, a three-dimensional matrix (200 x 200 x 200 pixels) of a sphere was created with susceptibilities of -8.3 ppm and -9.0 ppm inside and outside the sphere, respectively. These values resembled a typical but rather small susceptibility difference between the intracellular space and the extracellular phosphate buffered saline. The matrix of susceptibility values was Fourier-transformed (complex discrete fast Fourier transfrom) and then multiplied by $(1/3 - {k_z}^2/({k_x}^2+{k_y}^2 + {k_z}^2))$ with the coordinates in the spatial frequency domain k_i. After inverse Fourier-transformation, the magnetic B-field distribution in units of ppm was obtained from the real part of the complex outcome (the imaginary part was zero). Multiplying by 800 Hz/ppm yields the resonance frequency offset distribution in Hz. Setting $(1/3 - {k_z}^2/({k_x}^2+{k_y}^2 + {k_z}^2))$ to zero at $\vec{k} = \vec{0}$ assured that the simulated B-field distortions exhibited an average of zero. In other words,

only the B-field component was simulated that deviates from a magnetic B-field inside a homogeneous material with the average susceptibility. The B-field distortions were expressed in Hz, i.e. they were calculated for a specific NMR spectrometer resonance frequency, in this case 800 MHz.

Addionally to images of the central slice of the three-dimensional B-field distribution, also resulting intra- and extra-spheroid spectra were simulated by assuming a Lorentzian lineshape with a linewidth of 3 Hz for every voxel (i.e. a three-dimensional pixel) of the B-field distribution. After summation over all resulting Lorentzians the susceptibility-affected spectrum was contrasted with a 3 Hz Lorentzian. These simulations were performed for relative sphere diameters of 10 % to 100 % in steps of 5 %, resembling a huge range of interesting cellular densities from only $\pi/6000 \approx 0.05$ % to a maximum of $\pi/6 \approx 50$ %. The latter represents a close package of spheres (simple cubic arrangement) in contact with each other. Due to the fact that the digital Fourier transform acts on an image as if it was repeated periodically in every spatial direction, these regular cell packages could be simulated by solely processing images of one single sphere. The full widths at half maximum (FWHM) of each simulation were presented as a function of sphere diameter.

For the simulation of the intracellular magnetic B-field distortions, a two-dimensional model of an intracellular magnetic susceptibility distribution was drawn by hand assuming randomly shaped compartments with either -8.3 ppm or -9.0 ppm susceptibility. Adapted for the two-dimensional case, the same method was used as described above to calculate the field distortion map and the resulting susceptibility-affected spectrum.

4.4. NMR Spectroscopy – Technical Data

4.4.1. NMR Facility

All NMR-spectroscopic measurements were performed at ultra-stabilized high-resolution Bruker (Bruker BioSpin GmbH, Germany) Avance spectrometers resonating at 800 MHz (18.8 T) or 600 MHz (14.4 T). Both spectrometers were equipped either with Bruker TCI (800 MHz) or TXI (600 MHz) cryoprobes, pulsed-field gradient coils (max. gradient strength 0.535 T/m ± 0.01 T/m, determined with water reference sample) and a 32-coil shim system. Acquisition, processing and post-processing was conducted employing the NMR-spectroscopy software TopSpin (Bruker) Version 2.0 or 2.1.

4.4.2. Measurement Preparations

For at least five minutes prior to acquisition, the sample was allowed to equilibrilate with the spectrometer bore temperature which was set via the temperature control unit. For temporal stability, the magnetic B-field offset was kept constant by a lock unit operating on the deuteron resonance frequency of deuterium oxid which had been added to each sample

in a concentration of 10 %. Next, the oscillating circuit capacitors of the cryoprobe were adjusted to the spectrometer resonance frequency and to maximum absorption of the applied excitation power. The spatial homogeneity of the magnetic B-field within the sample was optimized by an automatic gradient-based optimization routine called TopShim, which is implemented in the TopSpin software. This procedure tries to minimize field inhomogeneities by iteratively changing the shim coil currents and monitoring the respective changes in the field profiles. Subsequently, the pulse length was adjusted to yield a 90° rotation of the magnetization by screening for the 360° zero crossing of the water resonance with a simple pulse-acquire pulse program (Bruker nomenclature: zg) and dividing the yielded pulse length by four. In a final step, the frequency offset of the water resonance was set to the center of the spectral width employing a presaturation pulse program (zgpr) and adjusting the frequency offset parameter to maximum water saturation.

4.4.3. Pulse Programs

All pulse programs used were upgraded with an excitation sculpting water suppression scheme [Hwang & Shaka 1995]. This procedure yielded maximum water suppression in combination with minimum effects on signals near the water resonance. In cases where additional water attenuation was mandatory, an additional adiabatic water presaturation was prefixed [Araníbar et al. 2006].

For one-dimensional NMR-spectroscopy, three different pulse programs were applied: A pulse-acquire scheme (Bruker nomenclature: zgesgp), which weights the signal only very slightly according to the gradient-based water suppression and thus provided virtually non-weighted and quantifiable control spectra; A T_2-weighting multiple spin-echo scheme known as Carr-Purcel-Meiboom-Gill sequence (cpmg1d), which – in contrast to the original T_2-sequence by Hahn – prevents evolution of J-coupling induced signal modulations and thus yields pure signal attenuation due to T_2-relaxation; A diffusion-weighting pulse sequence based on the stimulated echo approach with bipolar gradients and spoil gradients during the diffusion delay and the longitudinal eddy-current delay (ledbpgp2s1d) [Wu et al. 1995].

For two-dimensional NMR-spectroscopy, total correlation spectroscopy (TOCSY) pulse sequences provided by Bruker were employed, either without or with additional diffusion weighting (Bruker nomenclature: mlevesgpph and ledbpgpml2s1d, respectively).

The pulse program codes (Bruker language) of all modified pulse sequences are presented in Appendix section 8.2.

4.4.4. Acquisition Parameters

Unless otherwise stated in the text or figure captions of Results chapter 5, the acquisition parameters were as follows: Sweep width 12 kHz, 32K or 64K acquired FID-datapoints, acquisition time 1.4 s – 2.8 s, 90° hard pulse length 10 µs – 15 µs, presaturation power 45 dB – 55 dB, presaturation duration 0.5 s – 2 s, sinc-pulse shape of the adiabatic presaturation (length 10 ms, repeated 50 – 200 times), water-selective excitation sculpting pulse length 2 ms.

T_2-weighting: CPMG interpulse-delay 1 ms, CPMG echo-time 300 ms, i.e. 300 x 180°-pulse

Diffusion-weighting: diffusion gradients 4 ms – 10 ms (bipolar), maximum gradient strength 0.54 T/m, gradient shape: first half of sinus or rectangular, diffusion delay 50 ms – 200 ms, longitudinal eddy-current delay 5 ms, spoil gradients: 1 ms at 13 % or 17 of maximum gradient strength.

TOCSY: 8k and 512 time-domain datapoints in first and second dimension, respectively, mixing time 60 ms.

4.4.5. Processing and Post-Processing

The free induction decay (FID) of the one-dimensional data was multiplied by an exponentially decaying curve with a line broadening factor of 0.3 Hz to 3 Hz depending on the signal-to-noise ratio. After Fourier transformation, the resulting spectrum was phase- and baseline-corrected manually. The methyl signal of dimethyl-silapentane-sulfonate (DSS) was set manually to 0.0 ppm. If the DSS signal was attenuated below the noise level by diffusion-weighting, the same frequency offset was used as for the already DSS-standardized previous non-weighted spectrum.

In the case of TOCSY spectra, the raw data matrix was multiplied by a quadratic cosine bell in both dimensions to ensure a smooth convergence to zero at the end of the FID. After two-dimensional Fourier transformation the resulting spectra were phase-corrected manually in both dimensions and baseline-corrected automatically with a standard Bruker subroutine (abs) to the fifth polynomial order. The diagonal signal of methyl DSS was set to zero.

4.5. Mobile Lipid Quantification Strategy

The quantification of NMR-visible mobile lipid resonances consisted of three steps: First, the processed spectra were exported to ASCII-format and then imported in Matlab (The Mathworks, Germany). Second, employing the Matlab “Fitting Toolbox”, the spectral region between 1.5 ppm and 0.7 ppm was deconvolved by fitting with Gaussian-Lorentzian lineshapes. Overlapping peaks and multiplets of metabolites, amino acids, mobile proteins, mobile lipids, and impurities (agarose, ethanol and isopropanol) were included in this procedure. The fitting subroutine minimized the difference between the real data and the sum of the model peaks by simultaneously adjusting the amplitudes, chemical shifts, linewidths, j-coupling constants and Gaussian-Lorentzian ratios of every pre-defined resonance by applying the non-linear least squares method. Third, the resulting deconvolved peaks were integrated, and - serving as mobile lipid quantity according to the literature [Delikatny, Lander et al. 1996; Rosi et al. 2004; Iorio et al. 2003; Grande et al. 2006] – the mobile lipid methylene peak at 1.28 ppm was normalized to the sum of the macromolecular peaks between 1.1 ppm and 0.8 ppm, i.e. of the mobile lipid and mobile protein methyl resonances.

For further use after this PhD-thesis, the user-friendliness of the deconvolution program was improved by implementing a Microsoft Office Excel table-file, in which the user can manage her/ his own peak list including variable and inter-relating parameters such as chemical shifts, amplitudes, multiplet structures, j-couplings, linewidth, Gaussian-Lorentzian-ratios, each with start value and upper and lower fit boundaries. The source code of the program and an example of an Excel peak list file can be found in the Appendix section 8.3.

4.6. Statistical Evaluation

4.6.1. General Remarks

In all bar graphs the heights of the bars represent the statistical means and the error bars are equal to the standard deviation. Differences are considered significant, if the p-value is lower than 0.05 (one asterisk), highly signifcant for $p < 0.01$ (two asterisks) and extremely significant for $p < 0.001$ (three asterisks). If not stated otherwise, the significance level of a difference was tested with the unpaired two-tailored heteroscedastic Student's t-test.

4.6.2. Principal Component Analysis

For principal component analysis (PCA) the spectral region 4.20 – 0.70 ppm was used. Within this region, the following contaminants were excluded: DSS (1.80 – 1.72 ppm and 2.94 – 2.88 ppm), acetate (1.93 – 1.89 ppm) and DMSO (2.74 – 2.71 ppm). For each spectrum, 350 buckets (0.01 ppm bucket width) were integrated and scaled to the total intensity. Loadings, scores and explained variances were calculated using a Matlab (The MathWorks, Germany) standard PCA routine ("princomp").

4.6.3. Correlation Analyses

For multiple testing of correlations between highly variable spectral regions, named "regions-of-interest" (ROI), and other non-spectral data, e.g. biological assay outcomes, the spectra were normalized to the sum of intensities between 4.2 ppm and 0.7 ppm without the contaminant regions defined in 4.6.2, and Pearson's correlation coefficients were calculated between the integrals of the ROI and the non-spectral data. For Bonferroni correction, which must be applied to multiply tested correlations in order not to receive false-positive results, the significance level was changed from 0.05 to 0.05 divided by the number of testings, i.e. the number of ROI.

5. Results

In the following chapter the results of experiments concerning NMR spectroscopy of neural progenitor cells (NPC), glioblastoma multiforme-derived tumor cell lines (GBM-TC) and brain tumor initiating cells (BTIC) are presented. The first section deals with general aspects of cell suspension NMR spectroscopy focussing on NMR-visibility and extra- vs. intra-cellular discrimination. In the second section, the biological relevance of NMR-visible mobile lipids in brain-derived stem- and tumor cells is addressed. In the final section of this chapter, the results of a metabolomic pilot study are treated, in which NMR spectra of ten different BTIC cell lines were analyzed by statistical tools to uncover possible correlations to biological assay outcomes relevant for stem cell identification.

5.1. General Aspects of Cell Suspension NMR Spectroscopy

In this section, several results addressing the informative value of ^{1}H-NMR spectroscopy on cell suspensions are evaluated. The focus is on the comparison of different sample preparation methods, on consequences of susceptibility-induced magnetic B-field distortions, on the discrimination between extra- and intracellular molecules, and on NMR-visible macromolecules.

5.1.1. Typical Spectral Features and Resonance Assignment

In Fig. 5.1 the spectral range between 0.7 ppm and 4.2 ppm of a typical cell suspension NMR spectrum is shown. Sample properties and acquisition parameters are given in the caption. Roughly, the spectral features visible in Fig. 5.1 could be divided in two groups: First, sharp resonances with lineshapes and linewidths similar to that of the added internal standard, i.e. dimethyl-silapentane-sulfonate (DSS). Second, broad peaks with a typical linewidth of several tens of Hz, which are referred to as NMR-visible macromolecular peaks throughout this thesis. The assignment of resonances, also listed in Tab. 5.1, was verified by comparing chemical shift values, multiplet structures, J-couplings, and lineshapes with databases [Ulrich et al. 2008; Wishart et al. 2009] in the case of metabolites, amino acids and impurities, and with seminal literature concering mobile lipids [Al-Saffar et al. 2002; Barba et al. 1999; Cooper et al. 2001; Delikatny, Lander et al. 1996; Di Vito et al. 2001; Ferretti et al. 1999; Grande et al. 2006; Guidoni et al. 1987; Iorio et al. 2003; Luciani et al. 2009; Quintero et al. 2007; Rémy et al. 1997; Rosi et al. 1999] and mobile proteins [Behar et al. 1994; Behar & Ogino 1991; Behar & Ogino 1993; Kauppinen et al. 1992; Kauppinen et al. 1992; Kauppinen et al. 1993] in the case of NMR-visible macromolecules.

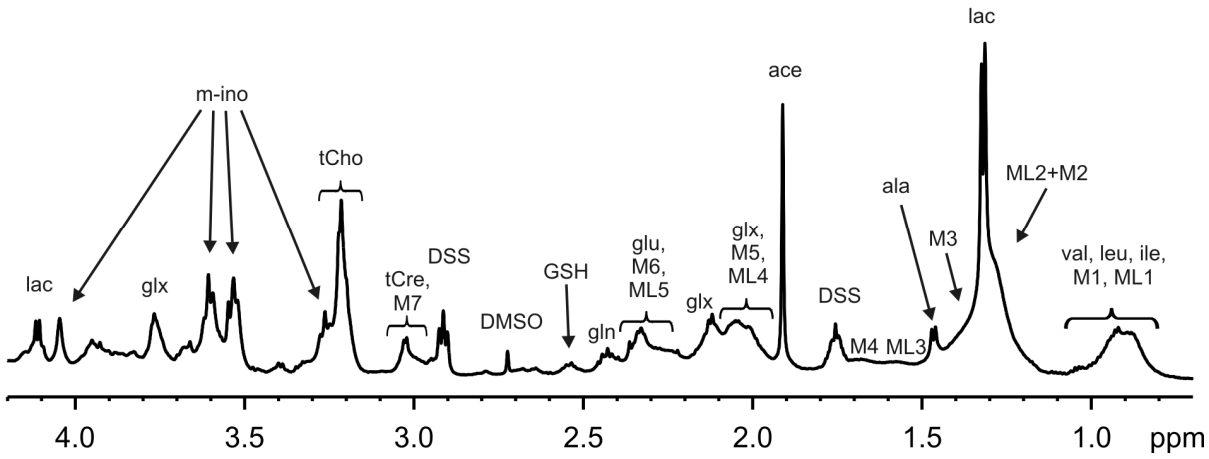

Fig. 5.1 Representative cell suspension NMR spectra with assignment. Averaged spectrum of 20 brain tumor-initiating cell (BTIC) samples. Assignment according to **Tab. 5.1**. Acquisition parameters: 3-5 million cells in 550 µl PBS containing 10% D_2O and 40 µM DSS, resuspended in 5 mm Shigemi tubes. T = 5° C, spectrometer frequency 600 MHz or 800 MHz, acquisition time 5 min, repetition time 4.75 s, water suppression: excitation sculpting plus presaturation. Spectra normalized to total intensity between 0.7 ppm – 4.2 ppm prior to averaging.

Chemical shift [ppm]	Compound name	Line shape	Abbreviation	Remarks
0.00	Dimethyl-silapentane-sulfonate	s	DSS	Added chemical shift standard
0.62	Dimethyl-silapentane-sulfonate	m	DSS	Added chemical shift standard
0.66	Cholesterolester	s	chol	Cyclopentane methyl group of cholesterol
0.80 – 0.95	Mobile lipid methyl groups	b	ML1	Terminal group of fatty acid chains in mobile lipids
0.80 – 1.00	Mobile protein branched chain amino acid residues	b	M1	
0.90 – 1.05	Branched-chain amino acids	m	BCAA	Valine, leucine and isoleucine
1.16	Isopropanol	d	isoprop	Cell culture impurity
1.17	Ethanol	t	ethOH	Cell culture impurity
1.17 – 1.27	Mobile protein threonine residues	b	M2	Minor contributions of mobile protein isoleucine residues
1.20 – 1.36	Mobile lipid methylene groups	b	ML2	Methylene groups neighbored by methylene groups within fatty acid chains
1.32	Lactate	d	lac	
1.33 – 1.50	Mobile protein alanine residues	b	M3	Minor contributions of mobile protein lysine and isoleucine residues
1.47	Alanine	d	ala	
1.52 – 1.62	Mobile lipid methylene groups	b	ML3	2^{nd} methylene group of fatty acid chains (near carboxyl group)
1.56 – 1.80	Mobile protein leucine, lysine and arginine residues	b	M4	
1.76	Dimethyl-silapentane-sulfonate	m	DSS	Added chemical shift standard
1.91	Acetate	s	ace	Impurity
1.91 – 2.15	Mobile lipid methylene groups	b	ML4	Methylene groups next to one (!) double bonded methine pair within unsaturated fatty acid chains
1.98 – 2.20	Mobile protein glutamine, glutamate and proline residues	b	M5	
1.95 – 2.20	Glutamine, glutamate, proline, glutathione	m	glx	
2.19 – 2.32	Mobile lipid methylene groups	b	ML5	1^{st} methylene group of fatty acid chains (next to carboxyl group)
2.24 – 2.39	Mobile protein glutamine, glutamate and proline residues	b	M6	
2.29 – 2.39	Glutamate	m	glu	Contributions of proline possible
2.40 – 2.50	Glutamine	m	gln	
2.50 – 2.60	Glutathione	m / b	GSH	
2.69	Dimethyl-sulfoxide	s	DMSO	Cell culture impurity
2.73 – 2.89	Mobile lipid methylene groups	b	ML6	Methylene groups surrounded by double bonded methine pairs within poly-unsaturated fatty acid chains
2.80 – 3.20	HEPES	m	HEPES	Cell culture buffer
2.9 – 3.05	Mobile protein residues	b	M7	Possible residues: cys, lys, phe, tyr; also contributions of GSH
3.00 – 3.06	Creatine compounds	s / b	tCre	Creatine and phosphocreatine
3.18 – 3.28	Choline compounds	s / b	tCho	Choline, phosphocholine (PC), glycerophosphocholine (GPC), phosphatidylcholine (PtdCho), and also possible contributions of mobile protein residues trp, arg, his
3.26	Myo-inositol	t	m-Ino	
3.30 – 4.80	Agarose	m / b	aga	
3.50 – 3.64	Myo-inositol	m	m-Ino	
3.72 – 3.79	Glutamine and glutamate	m	glx	
4.05	Myo-inositol	b	m-Ino	

Tab. 5.1 Spectral assignment of major NMR-visible compounds in cell suspension NMR spectroscopy. Abbreviations for column “lineshape”: s = singlet, d = duplet, t = triplet, m = multiplet, b = broad peak or multiplet. Single chemical shift values at maxima of peaks, chemical shift ranges between approx. 5 % intensity of maxima in case of multiplets and broad peaks. Abbreviations of compounds: Conventional 3-letter abbreviations for amino acids, most common abbreviations for metabolites, macromolecules and impurities.

5.1.2. Comparison of Homogeneous Embedding in Agarose and Cell Pellet Sedimentation

Two main sample preparation methodologies were investigated with respect to feasibility, resulting spectral resolution and sensitivity, and informational reliability. First, homogeneous embedding of cells in ultralow gelling-point agarose, either in one or in three layers (Fig. 5.2 A and C, respectively). Second, sedimentation of cells within special NMR tubes with enlarged solid glass bottoms matched in magnetic susceptibility to water, i.e. so-called Shigemi tubes, either as 5 mm diameter standard design (Fig. 5.2 D) or as in-house customized 1-2 mm diameter version (Fig. 5.2 B), the latter being rebuild from hollow plugs of 5 mm Shigemi tubes by cutting the plug bottom such that the plug hollow space fits the sensitive coil volume of the cryoprobe. Both Shigemi versions allowed positioning of the solid glass bottom near or even within the sensitive coil volume without severe magnetic B-field distortions, as confirmed by pre-measurements with pure water samples (data not shown).

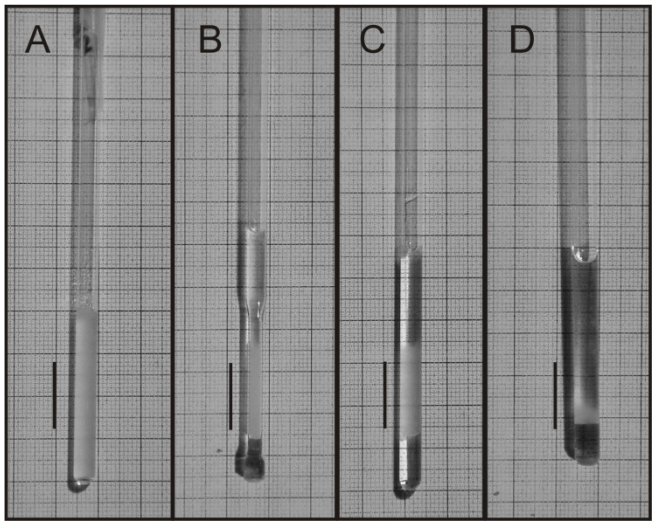

Fig. 5.2 Digital photographs of cell suspension samples representative for different sample preparation methods. (A) Homogeneous embedding with 1 % agarose in a 4.2 mm NMR tube (~ 220 µl within sensitive coil volume). **(B)** Sedimented cells in customized Shigemi plug, inner diameter ~ 1 mm (~ 13 µl within sensitive coil volume). **(C)** Same as in (A), but three layers of agarose, the middle one containing resuspended cells. **(D)** Sedimented cells in 5 mm Shigemi NMR tube (~ 300 µl within sensitive coil volume). Background: Millimeter scale. Additional vertical bars represent size and location of sensitive coil volume. Cell density corresponds to approx. 2 million GBM-TC or 10 million BTIC.

Typical spectra of the different sample preparation methods (Fig. 5.3) revealed major differences among the methodologies: First, embedding in agarose led to intense and complex signals in a wide spectral range (3.3 ppm – 4.2 ppm) due to agarose protons themselves. Second, in contrast to cells embedded in agarose and to sedimented cells in a 5 mm Shigemi tube, the Shigemi plug method resulted in a severe broadening of resonances that were normally sharp employing the other methods, e.g. the reference signal of DSS at 0.00 ppm and the lactate duplet at 1.32 ppm. This broadening effect was also observed for very high cell concentrations both in agarose samples and in 5 mm Shigemi tubes.

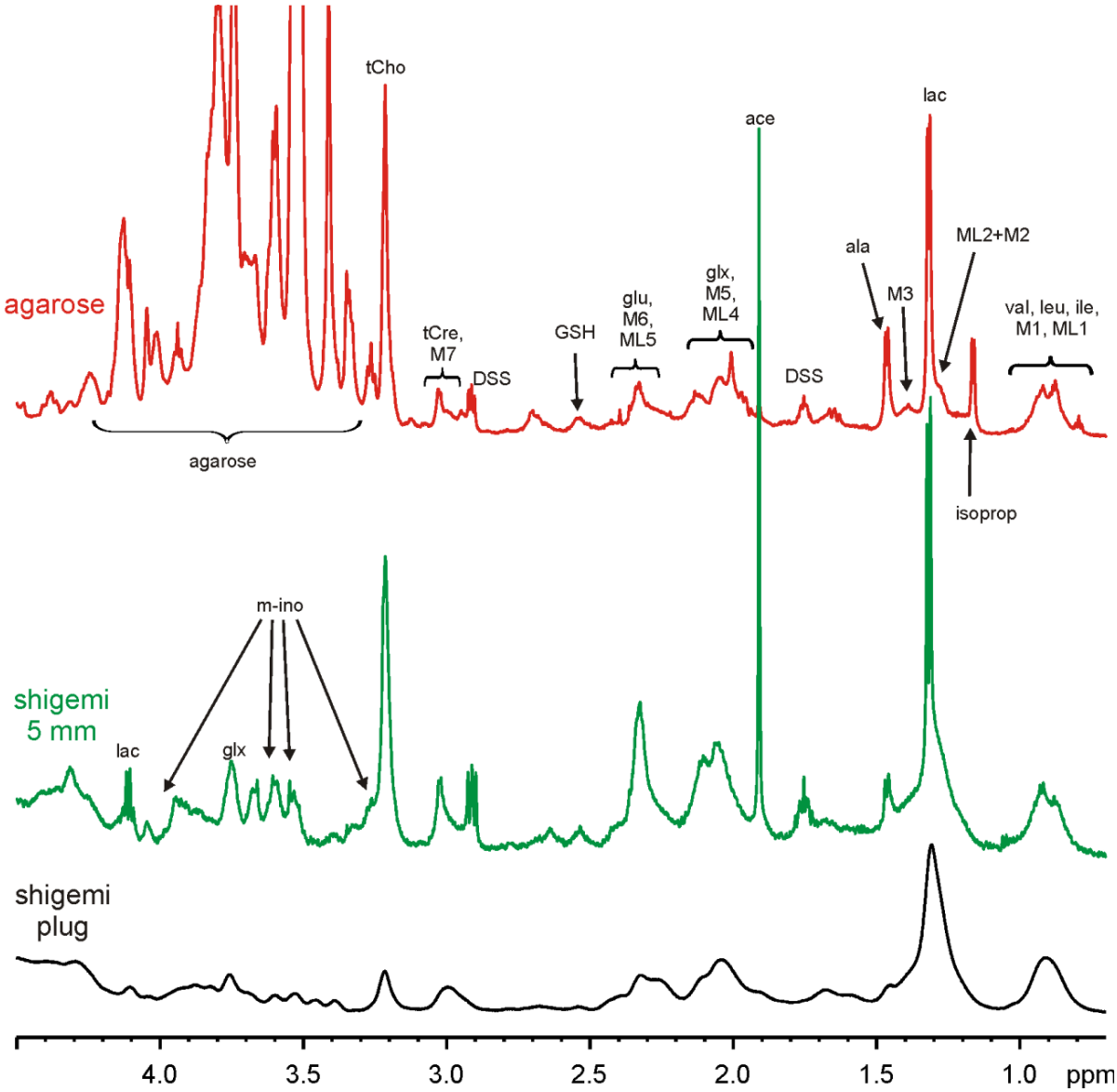

Fig. 5.3 NMR spectral comparison of sample preparation methods. (Top) Homogeneously embedded in agarose. 800 MHz, acquisition time 5 min, repetition time 4.75 s, water suppression: excitation sculpting plus presaturation. Approx. 5 million BTIC R40. **(Center)** Resuspended in 5 mm Shigemi tube. 600 MHz, acquisition time 5 min, repetition time 4.75 s, water suppression: excitation sculpting plus presaturation. 3.5 million BTIC R49. **(Bottom)** Sedimented within customized Shigemi plug. Spectrometer frequency 800 MHz, acquisition time 4 min, repetition time 3.75 s, water suppression: excitation sculpting. 15 million BTIC. T = 5° C. Note: Spectra were scaled to match in mobile protein intensity. Exponential line broadening 1 Hz. Assignment and abbreviations according to **Tab. 5.1**.

Occasionally, in case of sedimentation in 5 mm Shigemi tubes, a shift of the macromolecular resonances after sedimentation with respect to before sedimentation could be observed, especially – but not exclusively – when the automated shim optimization routine (topshim) was run simultaneously, i.e. after each measurement in a multiple series of measurements (Fig. 5.4). In contrast, sharp resonances were not affected. In Fig. 5.5 the corresponding field map of the magnetic B-field component parallel to the external field is plotted, revealing an offset of approximately 14 Hz throughout the volume of the sedimented cell pellet. This offset was inline with the spectral shift of macromolecular peaks (Fig. 5.4).

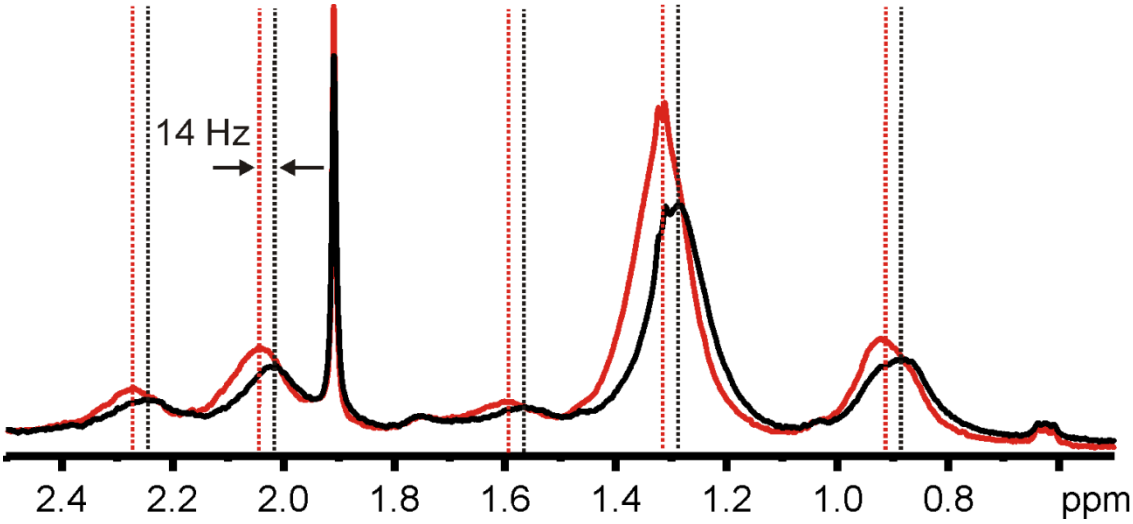

Fig. 5.4 Spectral changes during sedimentation and simultaneous automated shim optimization. (Black) Initial NMR spectrum. **(Red)** NMR spectrum after 2 h. Automated shim optimization (topshim) every 3 min during 2 h, i.e. 44 times. Frequency shift approx. 14 Hz. 5.6 million GBM-TC (HTZ-417) resuspended in 5 mm Shigemi tube in 500 µl PBS containing 50 µM DSS and 10 % D_2O. Acquisition time 2.3 min, repetition time 2.2 s, spectrometer frequency 600 MHz, T = 5° C, water suppression: excitation sculpting.

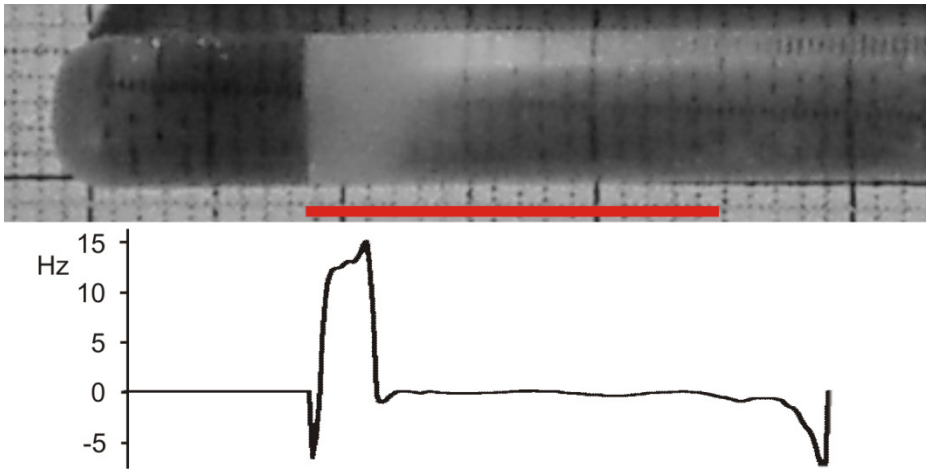

Fig. 5.5 Magnetic B-field changes during sedimentation and simultaneous automated shim optimization. (Bottom) Magnetic B-field map acquired with Bruker shim routine "topshim map" after 44 automated shim optimizations (topshim) every 3 min during 2 h, i.e. 44 times. 5.6 million GBM-TC (HTZ-417) resuspended in 5 mm Shigemi tube in 500 µl PBS containing 50 µM DSS and 10 % D_2O. Acquisition time 2.3 min, repetition time 2.2 s, spectrometer frequency 600 MHz, T = 5° C, water suppression: excitation sculpting. **(Top)** Representative digital photograph of 5 mm Shigemi tube with sedimented cells, rotated by 90° and scaled up to fit field map range. Red line: Size and position of sensitive coil volume. Background: Millimeter scale. Dark area: solid glass bottom, white area: sedimented cells.

In conclusion, the main outcome differences of the cell sample preparation methods were agarose signals in case of agarose embedding, broadened lines in case of dense pelleting in Shigemi plugs, and occasional resonance shifts in case of sedimentation inside 5 mm Shigemi tubes.

5.1.3. Simulation of Magnetic B-Field Inhomogeneities

The influence of inhomogeneous magnetic susceptibility distributions on cell density- and intracellular structure-dependent line broadenings in cell suspension NMR spectra was investigated by simulations of magnetic B-field distortions according to the theory introduced in section 3.1.2 employing the method described in section 4.3. The Matlab code is supplied in Appendix section 8.1.

5.1.3.1. Cell Density-Dependent Line Broadening

In Fig. 5.6 the effects of package density on lineshapes both inside and outside equally distributed spheres are illustrated.

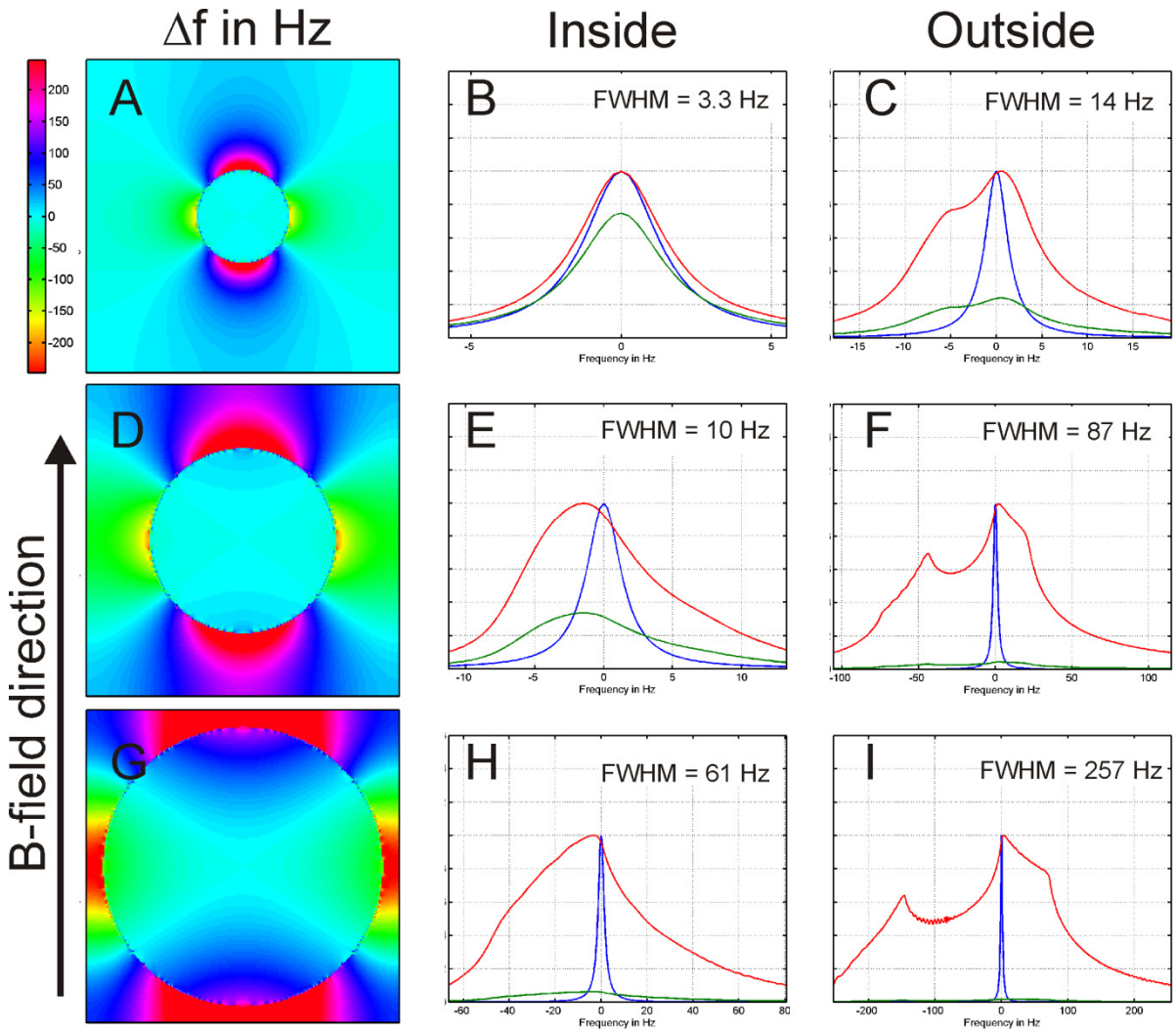

Fig. 5.6 Simulation of cell density-dependent magnetic B-field distortions. Spheres with homogeneous magnetic susceptibility -8.3 ppm placed in medium with susceptibility -9.0 ppm. **(A, D, G)** Color-encoded field distributions with package ratios 0.3 (A), 0.6 (D), 0.9 (G) (Package ratio: Sphere diameter divided by sphere distance center-to-center; ratio 0 would give a single sphere, ratio 1 a simple-cubic closed package). One color step corresponds to 5 Hz frequency difference. (2^{nd} and 3^{rd} column) Corresponding simulated spectra of volume inside **(B, E, H)** and outside **(C, F, I)** spheres (**blue**: control spectrum with 3 Hz linewidth for comparison, **green**: simulated spectrum, **red**: simulated spectrum scaled up to maximum intensity = 1). Resulting linewidths assigned. Reference frequency 800 MHz.

The simulated field maps for a susceptibility offset of 0.7 ppm between inside (e.g. fatty acid susceptibility: -8.3 ppm [Kuchel et al. 2003]) and outside the spheres (e.g. water, suceptibility: -9.0 ppm) revealed an expected dipole-induced distortion outside the sphere and almost no inhomogeneities inside the sphere in the case of low density package (Fig. 5.6 A), resulting in almost no broadening of an initial 3 Hz lineshape inside the sphere (Fig. 5.6 B) and a modest broadening outside (Fig. 5.6 C). However, increasing the density of the spheres yielded profound field distortions also inside the spheres (Fig. 5.6 D and G).

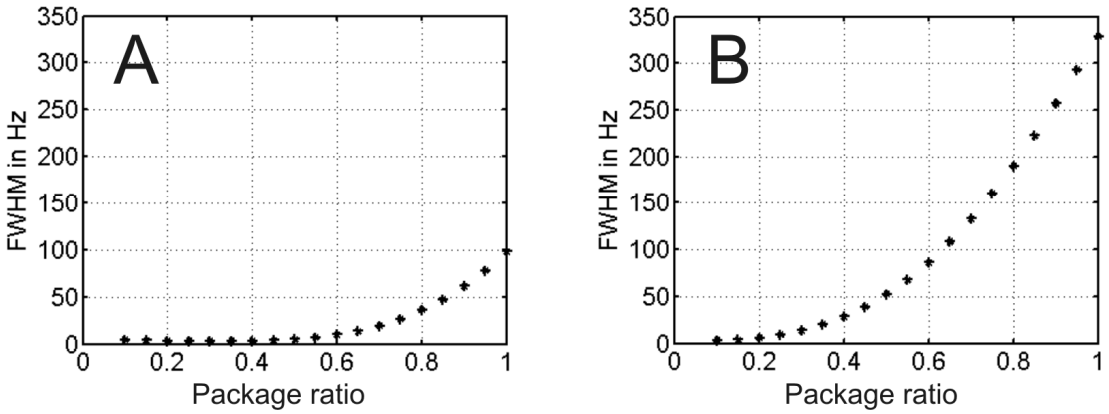

Fig. 5.7 Simulated line broadening as a function of cell density. Cell density dependent linewidths versus package ratio of diameter to distance (center-to-center) of spheres. (Ratio 0 would give a single sphere, ratio 1 a simple-cubic closed package). **(A)** Linewidth of volume inside sphere. **(B)** Linewidth of volume outside sphere. Spheres with homogeneous magnetic susceptibility -8.3 ppm placed in medium with susceptibility -9.0 ppm. Initial linewidth 3 Hz. Reference frequency 800 MHz.

At high package ratios this density-dependent effect broadened the assumed 3 Hz Lorentzians up to several tens of Hz inside (Fig. 5.7 A) and even hundreds of Hz outside (Fig. 5.7 B) the spheres.

The signal-to-noise ratio (SNR) is proportional to the concentration of a molecule and inversely proportional to the linewidth of its signal. Therefore, the SNR of a molecule inside the sphere relative to the SNR in pure solution (assuming 3 Hz linewidth) is the relative volume of intracellular and extracellular space divided by the line broadening factor (FWHM / 3 Hz). In Fig. 5.8, the relative SNR is plotted as a function of intracellular volume. The maximum of the relative SNR lays between 6.5 % and 8.5 % volume ratio, i.e. at package ratios (diameter to distance of the spheres) between 0.5 and 0.55. However, the maximum value of the relative SNR is below 4 %.

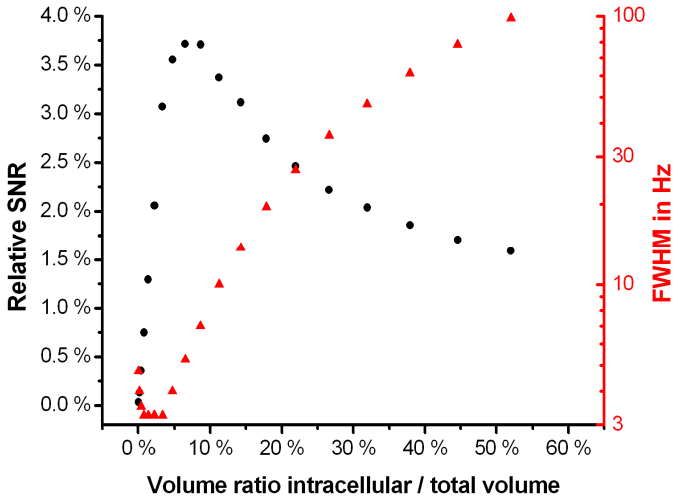

Fig. 5.8 Relative signal-to-noise ratio (SNR) of an intracellular resonance as a function of relative sphere volume. Relative SNR = relative intracellular volume divided by line broadening factor (FWHM / 3 Hz). **(Red)** Full width at half maximum (FWHM) of intracellular space (same values as in **Fig. 5.7 A**). Simulation of spheres with homogeneous magnetic susceptibility -8.3 ppm placed in medium with susceptibility -9.0 ppm. Initial linewidth 3 Hz. Reference frequency 800 MHz.

All linewidth were calculated for a resonance frequency of 800 MHz, but can be recalculated for other frequencies in a straightforward manner, since the dipole effects scale linearly with the applied magnetic B-field.

5.1.3.2. Influence of Intracellular Structures

In addition to the effect described in the previous section, the influence of intracellular magnetic susceptibility inhomogeneities was also estimated. For a coarse two-dimensional model of intracellular membrane structures (Fig. 5.9 A) with a magnetic susceptibility difference of 0.7 ppm between membrane (black, susceptibility of fatty acids: -8.3 ppm [Kuchel et al. 2003]) and cytosol (white, susceptibility of water: -9.0 ppm) the resulting magnetic B-field distribution gave rise to an additional broadening of approximately 180 Hz for a reference frequency of 800 MHz (Fig. 5.9 C). Note that all calculations are linear with the applied magnetic field.

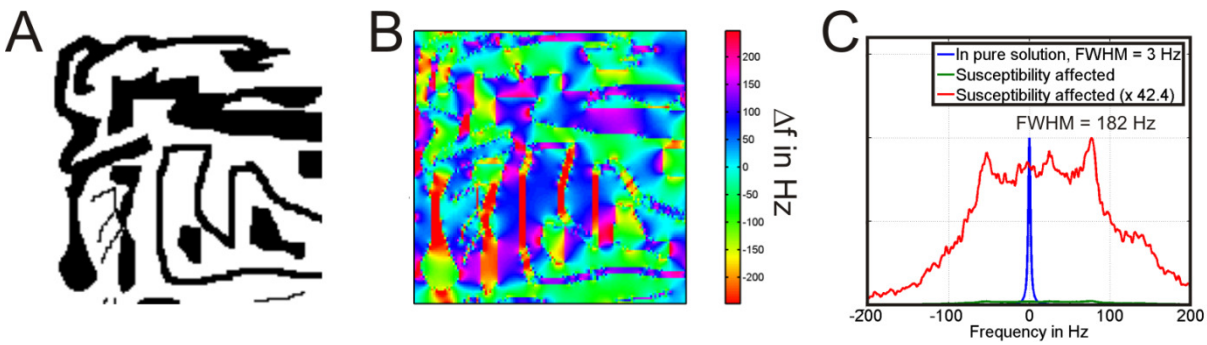

Fig. 5.9 Simulation of magnetic B-field distortions caused by intracellular magnetic susceptibility inhomogeneities. (A) Susceptibility distribution model. Black: susceptibility -8.3 ppm, white: susceptibility -9.0 ppm. **(B)** Color-encoded magnetic B-field distribution. One color step corresponds to 5 Hz frequency difference. **(C)** Corresponding simulated spectrum (**blue**: control spectrum with 3 Hz linewidth for comparison, **green**: simulated spectrum, **red**: simulated spectrum scaled up to maximum intensity = 1). Reference frequency 800 MHz.

Concluding this section, simulations of effects of magnetic susceptibility inhomogeneities on NMR spectra of cell suspensions resulted in package density- and structure-dependent line broadenings up to more than 100 Hz for susceptibility differences of 0.7 ppm between inside and outside or between membrane and cytosol, respectively.

5.1.4. Extra- and Intracellular Molecules

By their nature, cell suspension NMR spectra are weighted sums of extra- and intracellular contributions. In this section, experiences in different approaches of discrimination between these two contributors are reported.

5.1.4.1. Supernatant of Cell Suspension Samples

In case of the sample preparation method of sedimented cells in a 5 mm Shigemi tube, the major fraction of extracellular liquid can be separated after sedimentation by carefully collecting the supernatant. NMR spectra of both suspension and subsequently of supernatant (Fig. 5.10) revealed that almost all sharp resonances in suspension spectra were recovered in supernatant spectra. In contrast, broad peaks were not found in supernatant spectra.

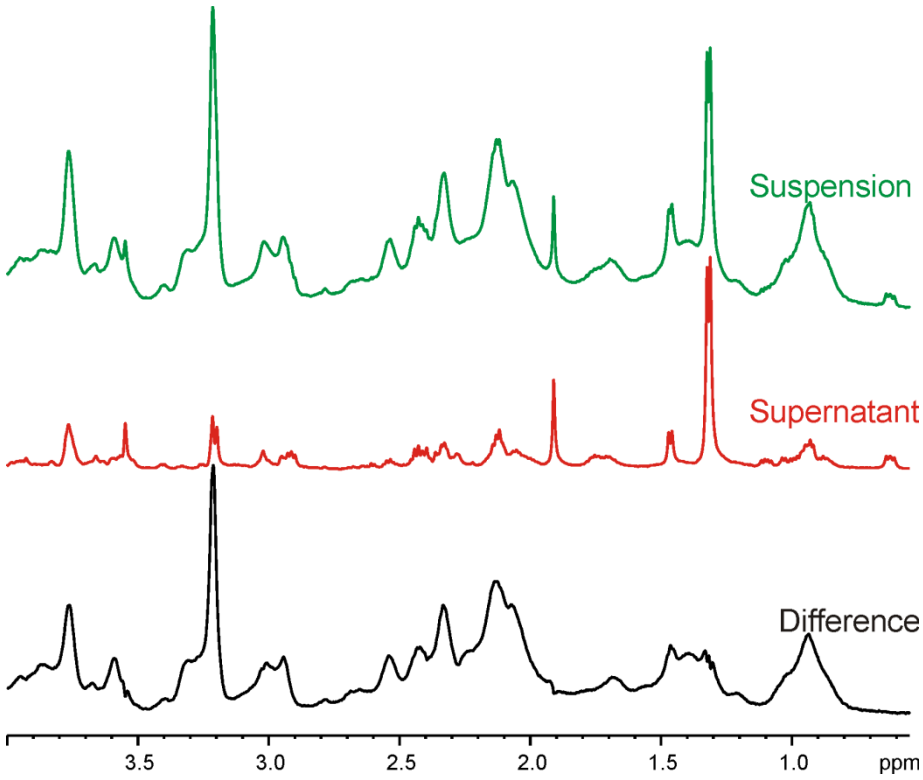

Fig. 5.10 Comparison of cell suspension NMR spectrum and subsequent NMR spectrum of supernatant. (Top) NMR spectrum of 5.1 million GBM-TC (U87) in 550 µl PBS containing 40 µM DSS and 10 % D_2O resuspended in 5 mm Shigemi tube. **(Center)** NMR spectrum of supernatant of sample after sedimentation. **(Bottom)** Difference of suspension (top, green) and supernatant spectra (center, red). T = 5° C, spectrometer frequency 600 MHz, acquisiton time 5 min, repetition time 4.75 s, water suppression: excitation sculpting plus presaturation.

5.1.4.2. Paramagnetic Contrast Agents

Estimated to selectively suppress signals of extracellular molecules via short-range relaxation enhancement, the effects of adding a paramagnetic contrast agent, gadopentatic acid (Gd-DTPA, Magnevist®, Bayer Schering, Germany, 500 mM), in different concentrations to cell suspensions was investigated. Fig. 5.11 reveals NMR spectral changes as a consequence of increasing the Gd-DTPA concentration. Sharp resonances, which were mainly assigned to the extracellular compartment (see previous section), were broadened but not suppressed. Additionally, also macromolecular peaks (e.g. M1+ML1 in Fig. 5.11 between 0.8 ppm and 1.1 ppm) were broadened although they were virtually not found in the extracellular supernatant (see previous section). Determination of the magnetic susceptibility of the used Gd-DTPA concentrations in phosphate-buffered saline (PBS) by means of the method described by Kuchel *et al.* [Kuchel et al. 2003] yielded values of -9.2 ppm, -9.0 ppm and -8.2 ppm for Gd-DTPA concentrations of 1:10'000 (50 µM Gd-DTPA), 1:1'000 (0.5 mM Gd-DTPA) and 1:200 (2.5 mM Gd-DTPA), respectively.

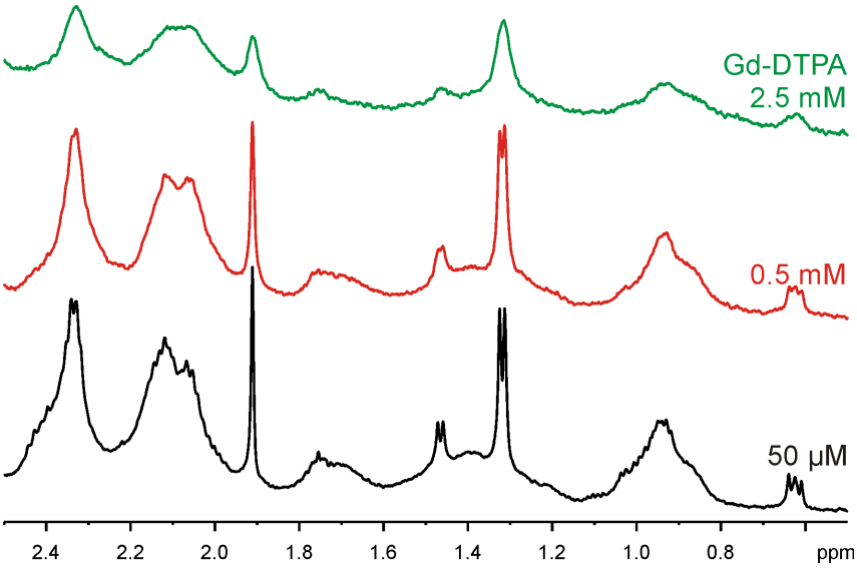

Fig. 5.11 Influence of additional paramagnetic contrast agent on cell suspension NMR spectra. NMR spectra of samples with different Gd-DTPA concentrations. (Bottom) ~1:10'000 Gd-DTPA = 50 µM, extracellular magnetic susceptibility χ_{mag} = -9.2 ppm. **(Center)** ~1:1'000 Gd-DTPA = 0.5 mM, χ_{mag} = -9.0 ppm. **(Top)** ~1:200 Gd-DTPA = 2.5 mM, χ_{mag} = -8.2 ppm. T = 5° C, spectrometer frequency 600 MHz, acquisition time 5:12 min:s, repetition time 4.85 s, water suppression: excitation sculpting plus presaturation. 7 million GBM-TC (HTZ-349) in 550 µl PBS containing 40 µM DSS and 10 % D_2O resuspended in 5 mm Shigemi tube.

Additional T_2-weighting experiments confirmed the relaxation enhancement effect of gadolinium in Gd-DTPA (Fig. 5.12). However, Gd-DTPA-induced signal attenuations upon T_2-weighting revealed that none of the sharp resonances were affected to a lesser extent than those of clearly extracellular molecules, e.g. cell culture/ cell handling impurities acetate (1.91 ppm) and formic acid (8.44 ppm). In other words, upon Gd-DTPA all NMR signals were strongly attenuated by T_2-weighting, and none of the signals showed a T_2-time that was longer than those of supernatant compounds.

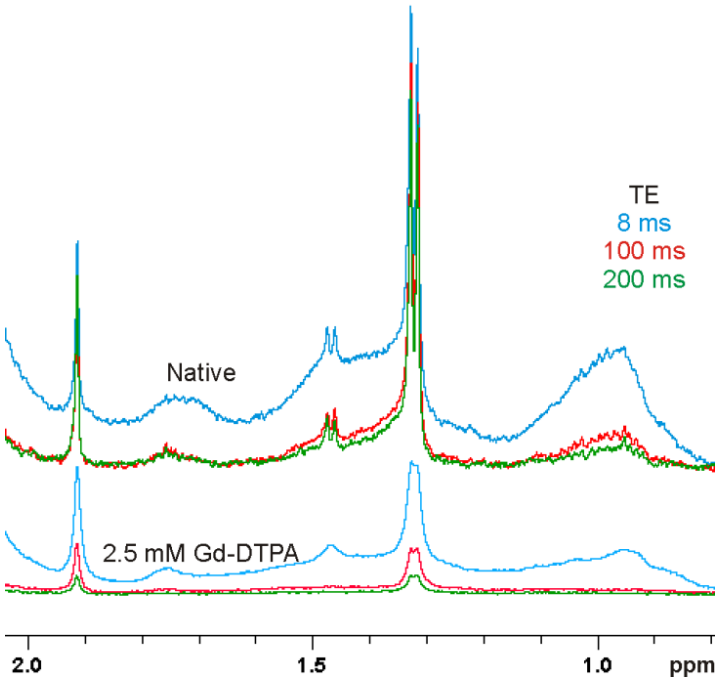

Fig. 5.12 Gd-DTPA-induced T_2-relaxation enhancement. T_2-weighted cell suspension NMR spectra. **(Top)** Native sample without Gd-DTPA. Acquisition time 1:20 min:s, repetition time 4.85 s + TE. **(Bottom)** Sample with Gd-DTPA concentration ~1:200 = 2.5 mM. Acquisition time 43 min, repetition time 4.85 s + TE. Different T_2-weightings are color-coded. CPMG spin-echo times are assigned. T = 5° C, spectrometer frequency 600 MHz, acquisition time 5:12 min:s, repetition time 4.85 s, water suppression: excitation sculpting plus presaturation. pulse program: Carr-Purcell-Meiboom-Gill spin-echo (cpmg1d), interpulse delay 0.5 ms. 7 million GBM-TC (HTZ-349) in 550 µl PBS containing 40 µM DSS and 10 % D_2O resuspended in 5 mm Shigemi tube.

Independent on the sample preparation method, the cell type, the relaxation weighting (T_1, T_2, $T_{1\rho}$) procedure, and the Gd-DTPA concentration, resonances with linewidths smaller than those of clearly extracellular components have never been detected.

Furthermore, Gd-DTPA-induced line broadenings also affected the water resonance. As a consequence, in almost all cases of Gd-DTPA concentrations 1:200 or above, i.e. 2.5 mM Gd-DTPA, water-suppression failed resulting in a severe loss of sensitivity. Only in a small subset of measurements detection of cellular signals was possible at all. Additionally, strong resonances of Gd-DTPA protons masked the spectral region between 3 ppm and 4 ppm.

5.1.4.3. Diffusion-Weighted Experiments

By theory (see section 3.1.3), diffusion weighting attenuates molecules that are small and diffuse in an unhindered manner to a greater extent than big or confined ones. Therefore, small metabolites, e.g. lactate, located within cellular compartments are thought to be distinguished from their extracellular counterparts through smaller apparent diffusion coefficients.

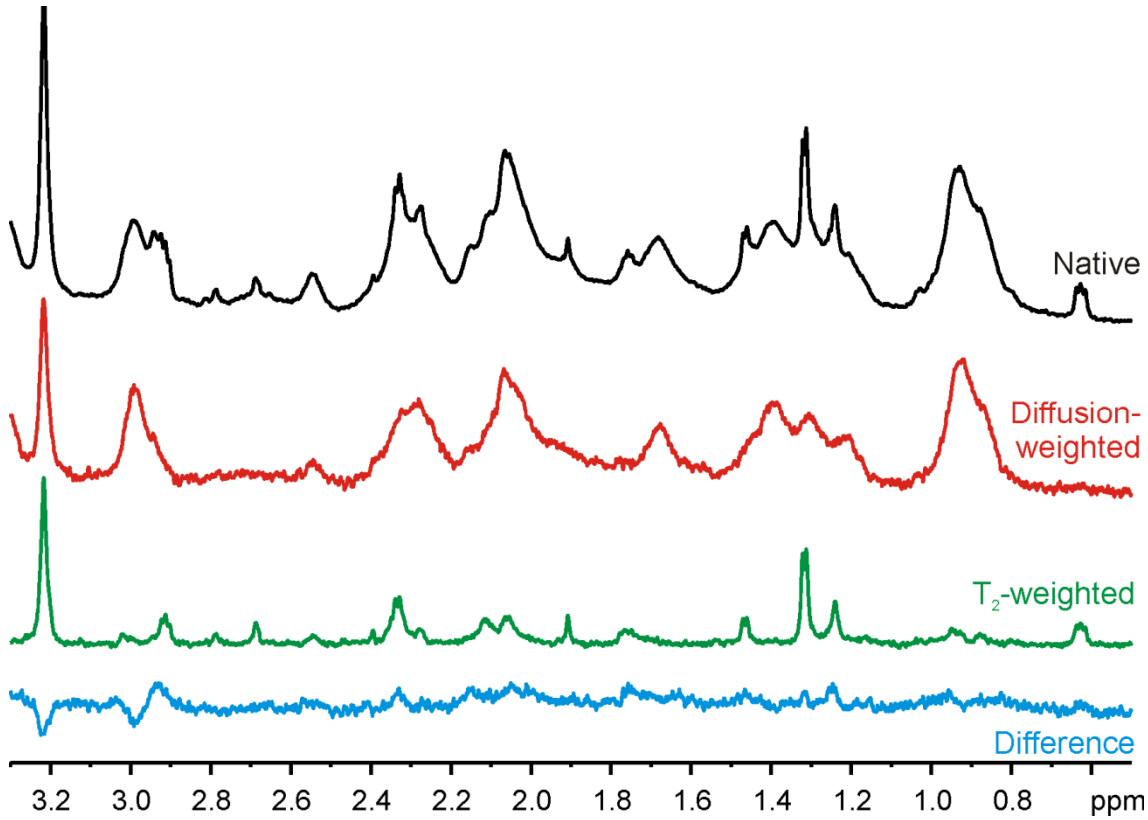

Fig. 5.13 Influence of diffusion weighting and relaxation weighting on cell suspension NMR spectra. (Top) Native spectrum without weighting. Acquisition time 4 min, repetition time 3.75 s, water suppression: excitation sculpting. **(2nd from top)** Diffusion weighted spectrum. b-value ($\gamma^2\delta^2g^2(\Delta - \delta/3 - \tau/2)$ as defined in section 3.1.3) = 1.1E10 s/m^2, Δ = 20 ms, δ = 6 ms, gradient strength 0.48 T/m, acquisition time 4 min, repetition time 1.9 s, water suppression: excitation sculpting, pulse program: bipolar pulsed field gradient stimulated echo with longitudinal eddy-current delay (ledbpgp2s1d) **(3rd from top)** T_2-weighted spectrum. TE 300 ms, 300 interleaved 180° pulses during TE, interpulse delay 1 ms, acquisition time 2 min, repetition time 3.75 s, water suppression: excitation sculpting, pulse program: Carr-Purcell-Meiboom-Gill spin-echo (cpmg1d). (**Bottom)** Difference of native, diffusion-weighted and T_2-weighted spectra. Note: Diffusion- and T_2-weighted spectra are scaled manually to yield a mininum residual difference. T = 5° C, spectrometer frequency 800 MHz. 5 million GBM-TC (HTZ-349) embedded in 600 µl 1 % agarose in PBS containing 50 µM DSS and 10 % D_2O resuspended in 5 mm NMR tube.

Fig. 5.13 shows a typical diffusion-weighted NMR spectrum, b-value = 1.1E10 s/m^2, together with the unweighted control spectrum and an additional, T_2-weighted spectrum, TE = 300 ms. By scaling these two weighted spectra manually, it was possible to cancel out almost all signals in the difference spectrum (control minus diffusion- and T_2-weighted) with a remarkable exception of choline compounds. Note the small, broad peak at 1.30 ppm in the diffusion-weighted spectrum, which is hardly distinguishable from the overlapping lactate duplet in the native spectrum.

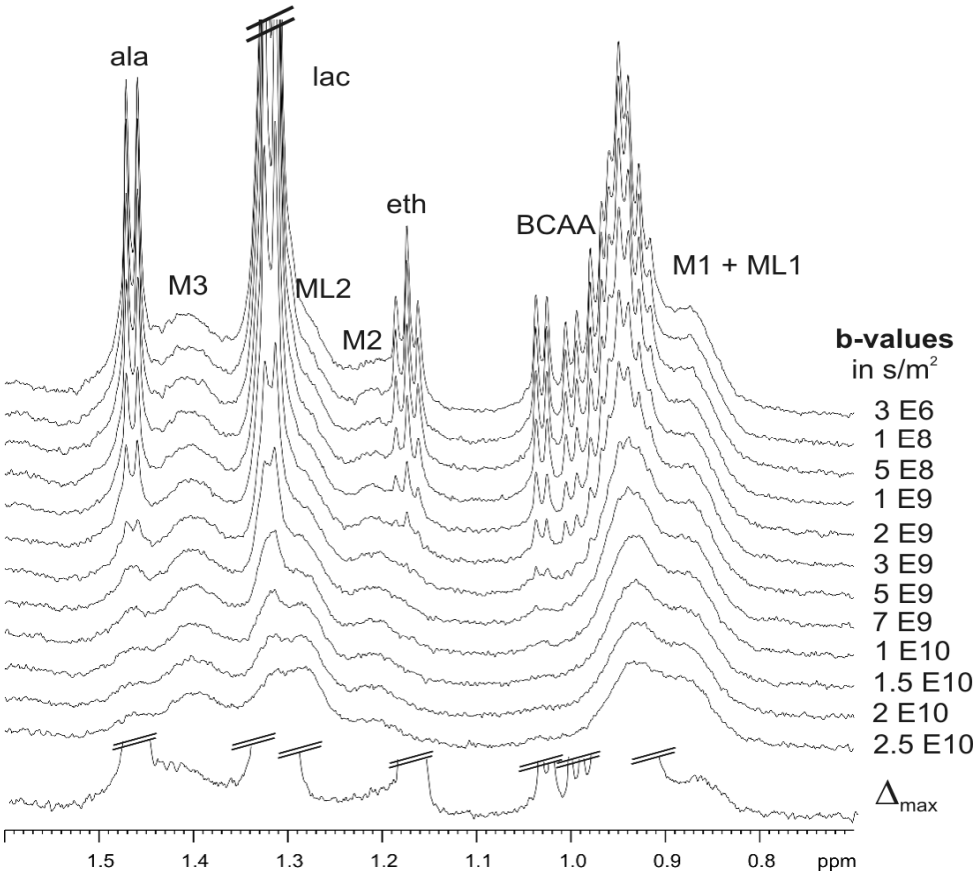

Fig. 5.14 Diffusion-ordered spectroscopy of cell suspension NMR spectra. Increasingly diffusion-weighted NMR spectra. b-values ($\gamma^2\delta^2g^2(\Delta - \delta/3 - \tau/2)$ as defined in section 3.1.3) are assigned to each spectrum at the right. Bottom spectrum: difference between weakest and heaviest diffusion weighting. Δ = 200 ms, δ = 4 ms, gradient strength 0.34 T/m, T = 5° C, spectrometer frequency 600 MHz, acquisition time 11:22 h:min, repetition time 5 s, water suppression: presaturation, pulse program: bipolar pulsed field gradient stimulated echo with longitudinal eddy-current delay (ledbpgppr2s). ~20 million GBM-TC (U87) in 550 µl PBS containing 40 µM DSS and 10 % D_2O resuspended in 5 mm Shigemi tube. Resonance assignment: Alanine (ala), mobile protein alanine residues (M3), lactate (lac), mobile lipid CH_{2n}-peak (ML2), mobile proteine threonine residues (M2), ethanol (eth), branched-chain amino acids valine, leucine, isoleucine (BCAA), mobile lipid and mobile protein CH_3 (M1+ML1).

In Fig. 5.14 increasingly diffusion-weighted NMR spectra of one cell suspension sample (GBM-TC U87) are depicted. While broad macromolecular resonances remained minimum 50 % of their original intensity at the heaviest diffusion weighting, sharp multiplets of alanine, lactate, ethanol and branched-chain amino acids were attenuated below the noise level. Remarkably, and in contrast to the ethanol triplet, at certain b-values, e.g. 1E10 s/m^2, at the position of alanine and lactate broader peaks remained after vanishing of the duplet structures.

The deconvolution procedure accounting for two components of each lactate and alanine, named “slow” and “fast” due to their slow and fast attenuation upon diffusion weighting, and subsequent exponential fitting of the deconvolved intensities versus b-values yielded diffusion coefficient values differing by a factor of approximately 2-3 between “slow” and “fast” components (Fig. 5.15). Note that for the “slow” components an additionally fit offset had to be used which resulted in 0.10 ± 0.005 and 0.18 ± 0.005 for lactate and alanine, respectively. While the “fast” components exhibited same linewidths as for the external standard DSS, i.e. 3 Hz, the “slow” components were significantly broader, i.e. 15 Hz. The “slow” components could never be found in diffusion weighting measurements of molecules

in solution, neither in control NMR spectra of cell culture medium nor in supernatant spectra (data not shown).

In this diffusion-ordered experiment, even the highest b-values were too small to substantially decrease NMR-visible macromolecular resonances. Consequently, diffusion coefficients of mobile lipid and mobile protein signals could not be determined.

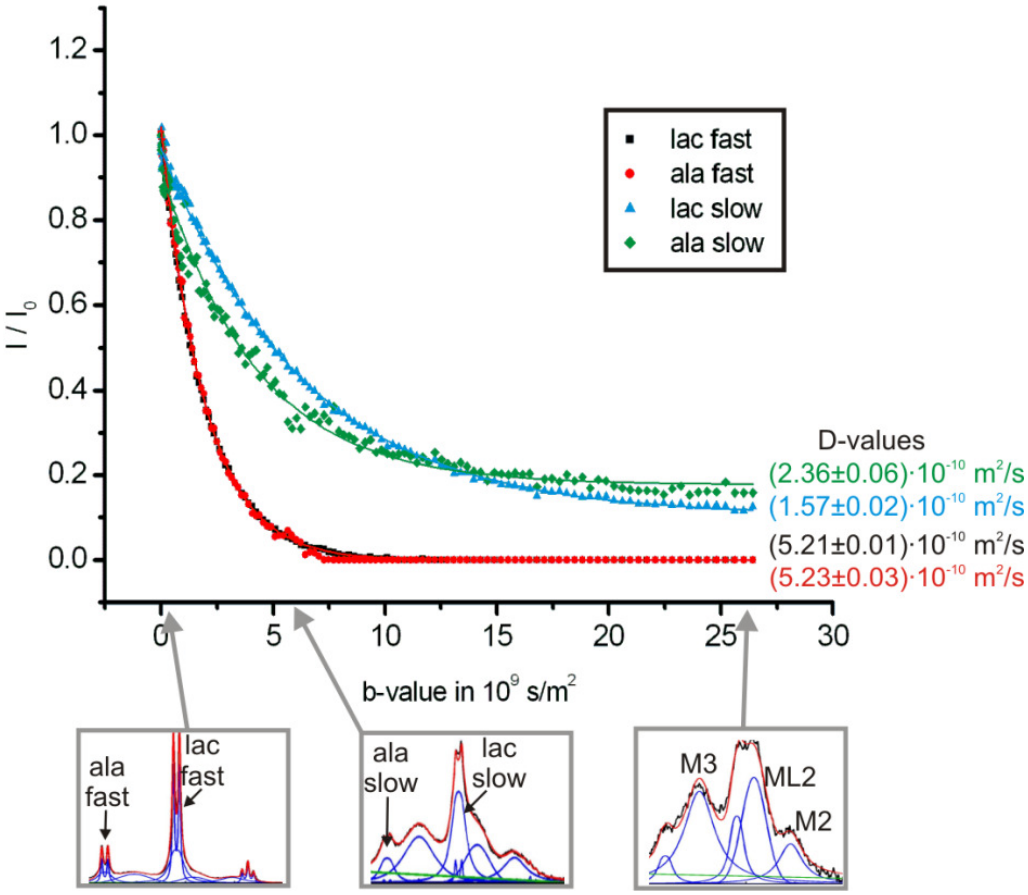

Fig. 5.15 Intra- and extracellular metabolite intensity attenuation by diffusion weighting. Integral values of the deconvolved NMR resonances of slowly and fast attenuated lactate and alanine components. b-values ($\gamma^2\delta^2g^2(\Delta - \delta/3 - \tau/2)$) as defined in section 3.1.3. Diffusion coefficients (exponential fitting plus constant) assigned at the right. Insets: Deconvolution outcomes 1.1 ppm – 1.4 ppm, scaled up to show full decomposition. DOSY parameters: Δ = 200 ms, δ = 4 ms, gradient strength 0.34 T/m, T = 5 °C, spectrometer frequency 600 MHz, acquisition time 11:22 h:min, repetition time 5 s, water suppression: presaturation, pulse program: bipolar pulsed field gradient stimulated echo with longitudinal eddy-current delay (ledbpgppr2s). ~20 million GBM-TC (U87) in 550 µl PBS containing 40 µM DSS and 10 % D_2O resuspended in 5 mm Shigemi tube.

In conclusion, diffusion weighting but not Gd-DTPA-induced relaxation enhancement was suitable to detect additional components which neither were found in supernatants nor could be assigned to macromolecules.

5.1.5. Characterization of NMR-Visible Macromolecules

In contrast to most NMR-visible small metabolites giving rise to sharp resonances, the identity and NMR-spectral characteristics of molecules generating broad but still evaluable peaks, so-called NMR-visible or “mobile” macromolecules, have not been clarified in detail yet (see section 3.1.4). Here, major results about the possibility to distinguish between the two subtypes of NMR-visible macromolecules, i.e. mobile lipids and mobile proteins, are presented.

5.1.5.1. Quantification by Deconvolution

In Fig. 5.16 typical NMR spectra of cell suspensions are shown, which differed in NMR-visible macromolecular composition ranging from mobile protein dominated spectra (green) to mobile lipid dominated spectra (red). Since almost all macromolecular resonances of one type were overlapped by corresponding resonances of the other type, a discrimination and robust quantification based on deconvolution strategies was not always possible, especially in cases of one species dominating the other one by far.

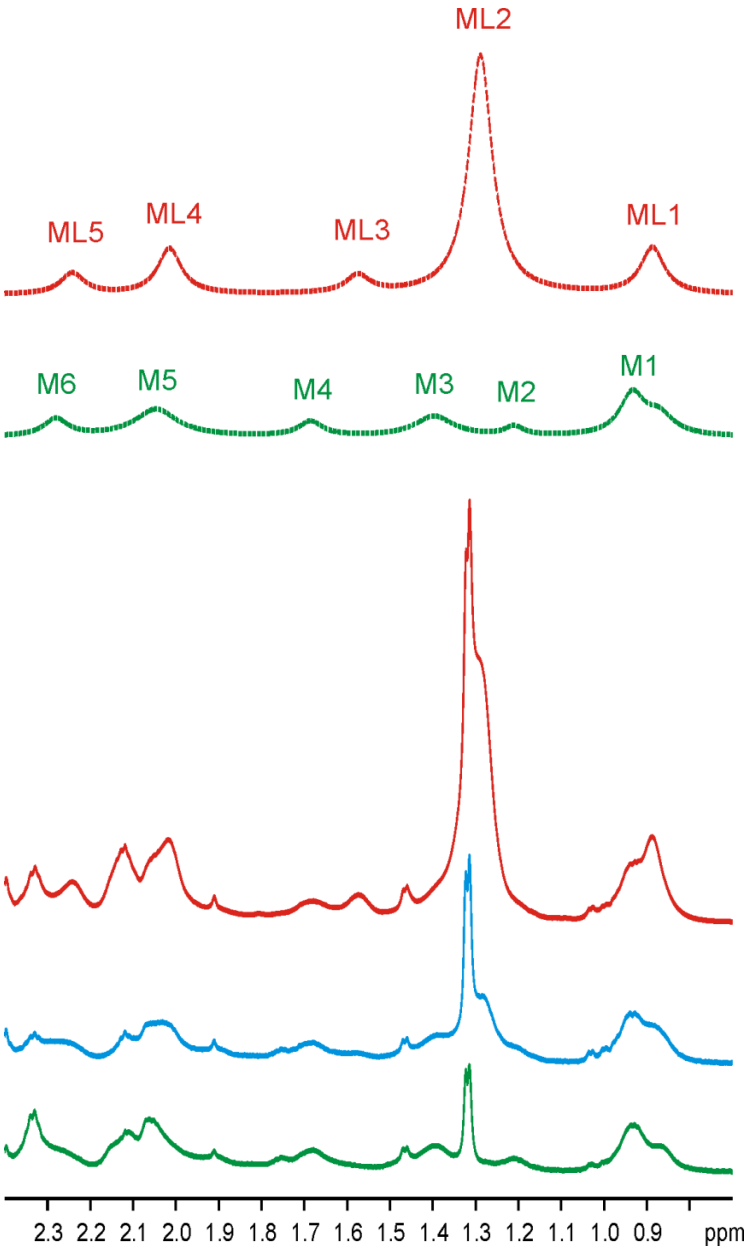

Fig. 5.16 Different compositions of NMR-visible macromolecules. Typical cell suspension NMR spectra showing different characteristics of macromolecular signals. **(Bottom)** ~10 million GBM-TC HTZ-349 without mobile lipid resonances. **(2nd from bottom)** ~10 million GBM-TC HTZ-417 with minor contributions of mobile lipids. **(3rd from bottom)** 11 million GBM-TC U87 with predominant mobile lipid intensities. **(Dashed lines) (2nd from top)** Simulated mobile protein spectrum consisting of 40 Hz Lorentzians at peptide random coil chemical shifts **[Wishart et al. 1995]** assigned with common mobile protein signal abbreviations. **(Top)** Simulated mobile lipid spectrum consisting of 40 Hz Lorentzians at published chemical shifts **[Hakumäki & Kauppinen 2000]** with common mobile lipid abbreviations. Parameters for recorded spectra: Acquisition time 5 min, repetition time 4.75 s, T = 5° C, spectrometer frequency 800 MHz, water suppression: excitation sculpting plus presaturation. GBM-TC in 550 µl PBS containing 40 µM DSS and 10 % D_2O resuspended in 5 mm Shigemi tube. Note: Spectra were scaled up to match in mobile protein resonance intensities.

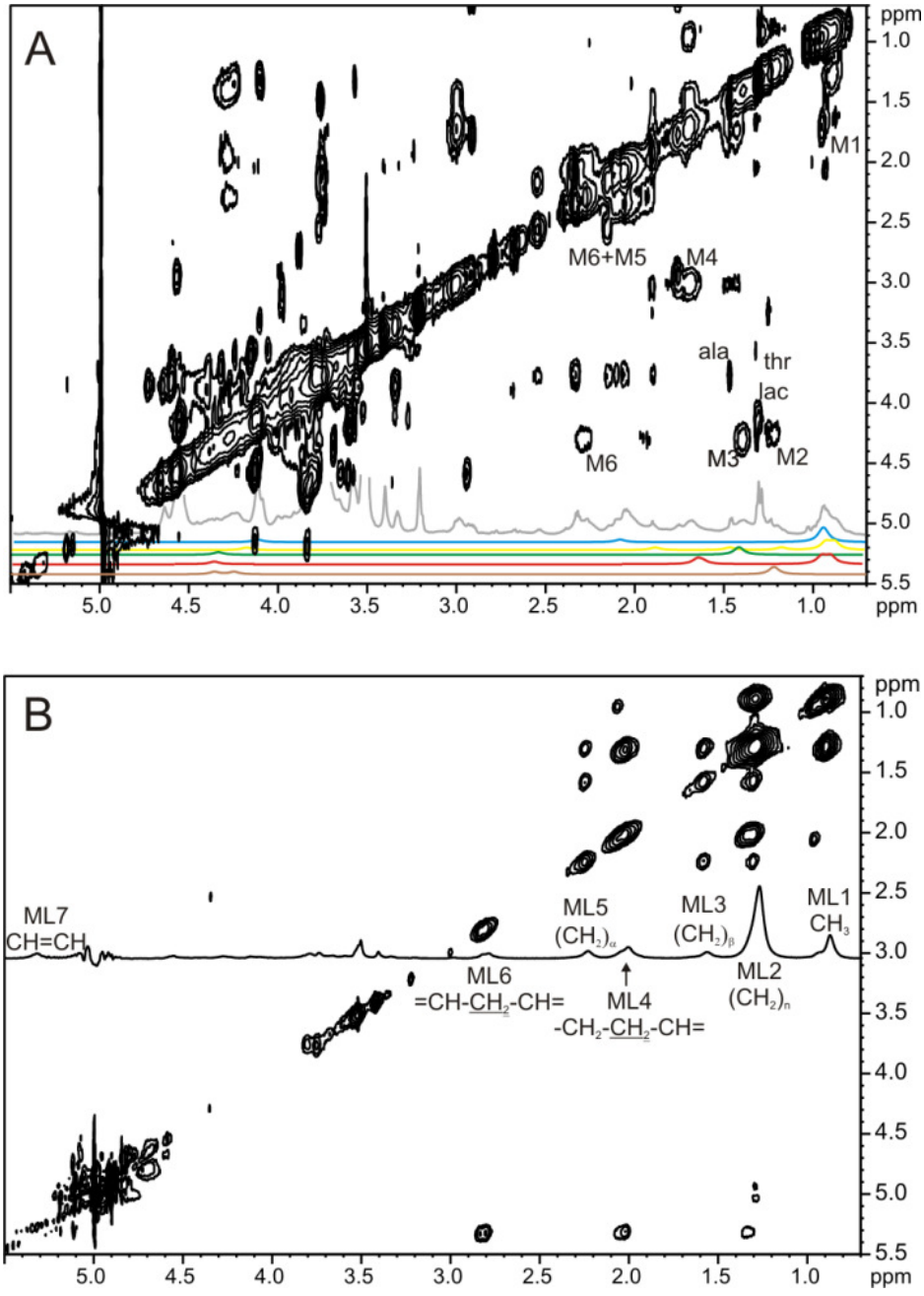

Fig. 5.17 Total correlation spectra (TOCSY) of cell suspensions. (A) Sample with predominant mobile protein resonances. Crucial crosspeaks assigned. Overlayed 1D-spectra (from top to bottom): 1D-projection of TOCSY (grey), simulated 40 Hz Lorentzian spectra at chemical shifts of random coil peptides **[Wishart et al. 1995]** of amino acid residues leucine (red), isoleucine (yellow), valine (blue), alanine (green), threonine (brown). Mixing time of TOCSY: 60 ms, acquisition time 256 x 1 min = 4:25 h:min, repetition time 1.93 s, 8K x 512 datapoints Fourier-transformed. 5 million GBM-TC (HTZ-349) in 600 µl 1 % agarose in PBS containing 50 µM DSS and 10 % D_2O resuspended in 5 mm NMR tube, water suppression: excitation sculpting. **(B)** Sample with predominant mobile lipid resonances. 2-10 million MSC in 600 µl 1 % agarose in PBS containing 50 µM DSS and 10 % D_2O resuspended in 5 mm NMR tube. 1D-spectrum: TOCSY projection assigned with common abbreviations for mobile lipid signals (ML1 – ML7). The corresponding chemical groups of fatty acid chains that give rise to ML1 – ML7 are also given. Mixing time of TOCSY: 60 ms, acquisition time 371 x 2.56 min = 15:50 h:min, repetition time 2.4 s, 8K x 512 datapoints Fourier-transformed. Additional diffusion weighting to suppress sharp metabolite resonances: b-value 1.5E10 s/m^2, Δ = 200 ms, δ = 6 ms, gradient strength 0.34 T/m, bipolar pulsed field gradient stimulated echo with longitudinal eddy-current delay. Pulse program: ledbpgpml2s192d, water suppression: WATERGATE. (A, B) T = 5° C, spectrometer frequency 800 MHz.

5.1.5.2. Discrimination between Mobile Lipids and Mobile Proteins

Since mobile protein resonances could be assigned to amino acid residues exhibiting chemical shifts similar to those of random coil peptides (see section 3.1.4), and mobile lipid resonances are caused by fatty acid chain protons, a discrimination between mobile lipids and mobile proteins should be possible on the basis of total correlation spectroscopy (TOCSY) crosspeaks. Fig. 5.17 displays two TOCSY spectra, one with predominant mobile protein resonances (Fig. 5.17 A), the other one with predominant mobile lipid resonances (Fig. 5.17 B). Apart from differences in agarose signal intensities, the most prominent differences were in rows between 4.0 ppm and 4.6 ppm (mainly mobile protein residue crosspeaks) and rows between 5.0 ppm and 5.6 ppm (mainly mobile lipid fatty acid chain crosspeaks).

In these spectral regions, even in the case of samples profoundly dominated by mobile lipid signals (Fig. 5.17 B), one-dimensional projections revealed underlying mobile protein resonances, e.g. M3 (Fig. 5.18).

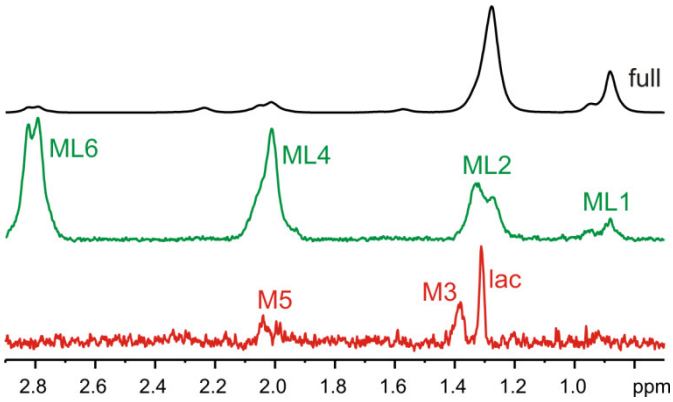

Fig. 5.18 TOCSY projections specific for macromolecular species. (Top) Full projection of rows of mobile lipid dominated TOCSY (**Fig. 5.17**). **(Center)** Pure mobile lipid signals. Projection of rows 5.0 ppm – 5.6 ppm, multiplied by 55. **(Bottom)** Pure mobile protein signals. Projections of rows 4.0 ppm – 4.6 ppm, multiplied by 200. Acquisition parameters given in **Fig. 5.17**.

In the following, mobile protein and mobile lipid resonances between 1.5 ppm and 0.7 ppm, i.e. M1, M2, M3, ML1 and ML2, were investigated with respect to relaxation and diffusion parameters. So-called pseudo-2D experiments, i.e. multiple one-dimensional measurements with increasing diffusion or relaxation weightings, were evaluated by assuming Gaussian-Lorentzians at chemical shift values tabulated in Tab. 5.1, by adjusting linewidths, Gaussian-Lorentzian-ratios, and – in the case of mobile protein resonances – intensity-ratios among each other manually, and by optimizing peak amplitudes with a Matlab fit routine for each weighting step.

Spin echo experiments (Carr-Purcell-Meiboom-Gill sequence) yielded T_2-values of 62.2 ± 0.5 ms, 146 ± 1 ms and 56.3 ± 0.2 ms for resonances MP (i.e. M1+M2+M3), ML1 and ML2, respectively (Fig. 5.19).

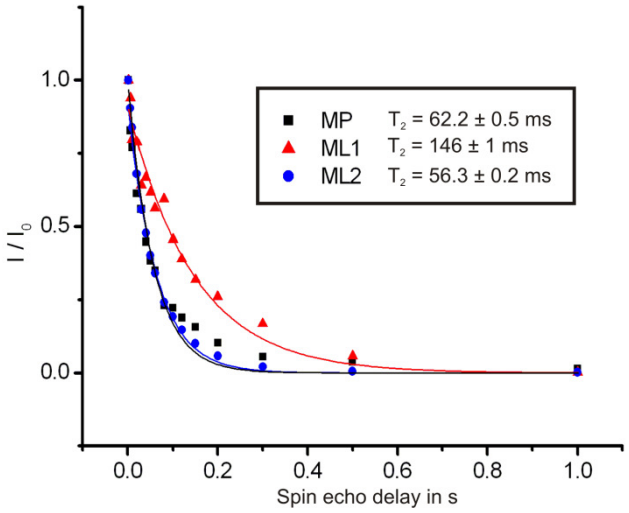

Fig. 5.19 Spin echo experiment to determine macromolecular T_2-values. Integral values of the deconvolved NMR resonances of mobile lipid and mobile protein residues against spin echo delay. Attenuation curves were fit by the function $I(TE) = I_0 \exp(-TE/T_2)$, yielded T_2-values are assigned in the legend. Acquisition time 3:33 h:min, repetition time 12.5 s + TE, T = 5 °C, spectrometer frequency 800 MHz, water suppression: Excitation sculpting plus presaturation, pulse program: Carr-Purcell-Meiboom-Gill spin-echo (cpmg). 7.9 million NPC embedded in ~200 µl 1 % agarose in PBS containing 50 µM DSS and 10 % D_2O (3-layer-method).

Fig. 5.20 displays the results of an inversion-recovery-based T_1-measurement. Again, the integral values of deconvolved resonances ML1, ML2 and MP (M1+M2+M3) are plotted. The individual recovery curves were fit by the function $I(TI) = I_0 (1-(1-\cos\alpha) \exp(-TI/T_1))$, i.e. allowing an inversion pulse flip angle α not equal to 180°. Although the inversion-recovery delay TI between the inversion pulse and the read-out 90° pulse was as little as 1 µs for the first experiment, and despite careful 90° pulse length determination (through the 360° zero-crossing of water), all macromolecular signals were significantly weaker in the first experiment compared to in the last experiments, i.e. compared to the fully relaxed situation after 7 s. This phenomenon led to an initial inversion pulse angle of 155° ± 2° as result of the fit routine. Obtained T_1-values were 0.54 ± 0.01 s for mobile protein resonances, and 0.87 ± 0.01 s and 0.70 ± 0.01 s for mobile lipid signals ML1 and ML2, respectively.

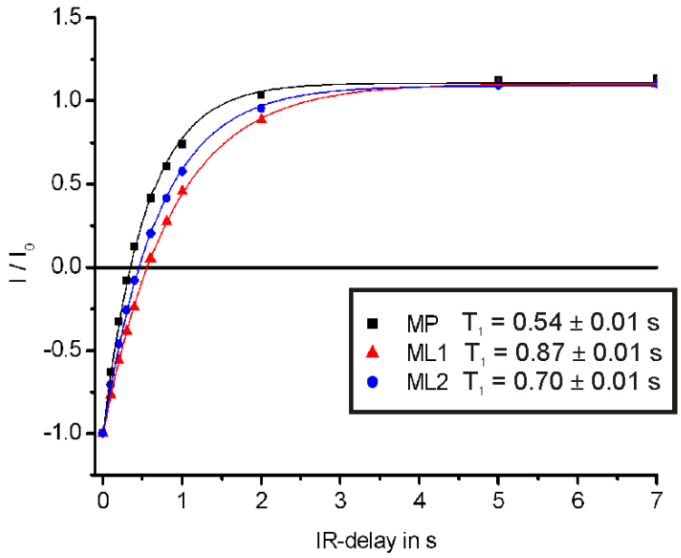

Fig. 5.20 Inversion recovery experiment to determine macromolecular T_1-values. Integral values of the deconvolved NMR resonances of mobile lipid and mobile protein residues against inversion recovery delay. Recovery curves were fit by the function $I(TI) = I_0 (1-(1-\cos\alpha) \exp(-TI/T_1))$, yielded T_1-values are assigned to the curves within the legend. Acquisition time 40 min, repetition time 4.4 s + TI, T = 5 °C, spectrometer frequency 800 MHz, water suppression: Excitation sculpting. 7.9 million NPC embedded in ~200 µl 1 % agarose in PBS containing 50 µM DSS and 10 % D_2O (3-layer-method).

Employing the zero-crossings of the inversion recovery experiment would allow specific signal nullings of mobile lipid resonances according to their difference in T_1-value with

respect to mobile protein resonances. However, intense negative amplitudes of overlapping small metabolite resonances, e.g. lactate, would render quantification virtually impossible.

In contrast, inversion recovery experiments with more than one inversion pulse are capable of simultaneously nulling signals within a whole range of T_1-values [de Graaf et al. 2006]. However, the different inter-pulse delays between the multiple inversion pulses have to be adjusted carefully. To configure these inter-pulse delays an optimizing routine was developed in Matlab that should give maximum ratios between the resonance of interest (here e.g. mobile proteins) and the unwanted signals of both mobile lipids and metabolites. Fig. 5.21 illustrates the simulated behavior of the magnetization in the direction of the applied magnetic B-field, i.e. in the z-axis, for a triple-inversion-recovery scheme, i.e. for a pulse sequence with three 180°-pulses followed by a 90°-readout pulse. At the fit optimum for the two inter-pulse delays and the read-out time-point, the relative amplitude of the resonance of interest (MP) was 0.05, but the relative amplitudes of signals exhibiting T_1-values between 0.7 s and 1.7 s were 0.007 or lower. Consequently, a relative attenuation of more than 7 should be gained to the cost of a loss in signal-to-noise ratio of 0.05.

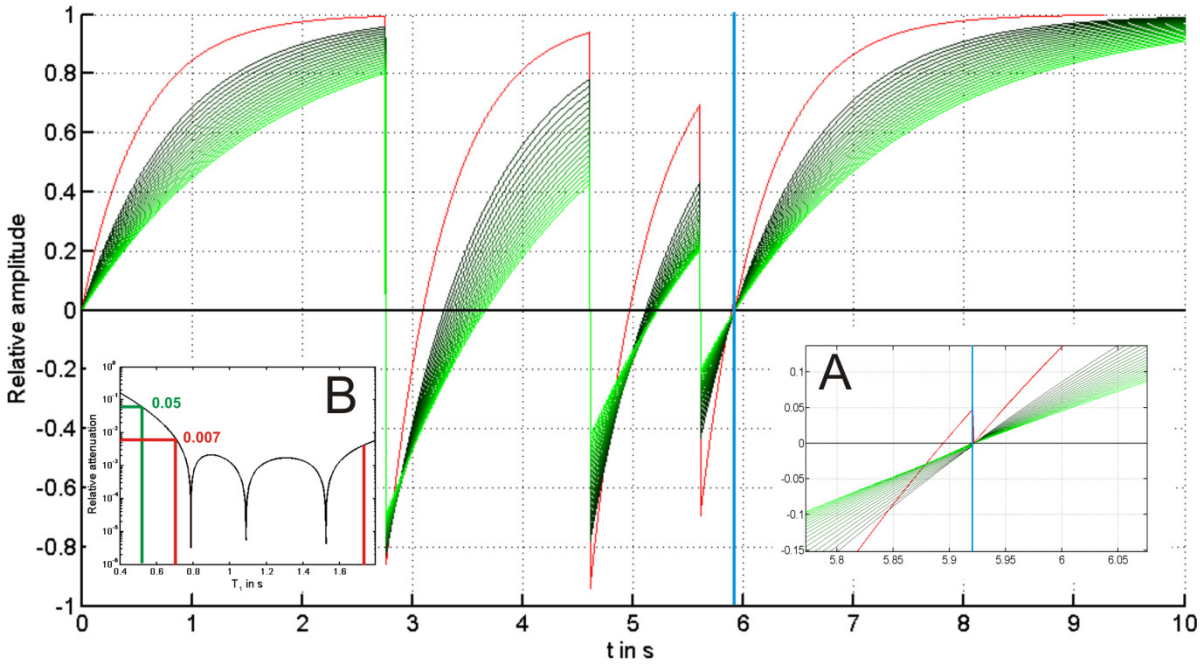

Fig. 5.21 Simulation of selective T_1-based attenuation by multiple inversion recovery pulse sequences. Magnetization dynamics in the direction of the external magnetic B-field throughout the triple inversion recovery sequence with inter-pulse delays of 1.85 s, 1.00 s, 0.31 s between three 180° pulses. Red curve for T_1 = 0.54 s, i.e. mobile proteins. Green curves for T_1-values between 0.7 s and 1.7 s, i.e. mobile lipids and metabolites. Blue line: 90° read-out pulse time-point. Inset **(A)**: Zoom into the time window of the 90° pulse. Inset **(B)**: Relative attenuation as a function of T_1-value for the obtained optimum inter-pulse delays. The green line marks the relative attenuation for T_1 = 0.54 s, i.e. of mobile proteins, the red lines enframe the T_1-value range of mobile lipids and metabolites.

Applying these simulated inter-pulse delays to a real triple-inversion-recovery experiment – and further simulated parameters to a double-inversion-recovery experiment – resulted in NMR spectra depicted in Fig. 5.22. When scaled up to match in mobile protein resonance intensities, a relative attenuation of mobile lipid (ML2 at 1.28 ppm, ML1 at 0.87 ppm) and

small molecule (e.g. lac at 1.32 ppm, isoprop at 1.16 ppm) signals was evident. However, the relative attenuation of ML2 to mobile protein signals was not 7:1 but only 3:1.

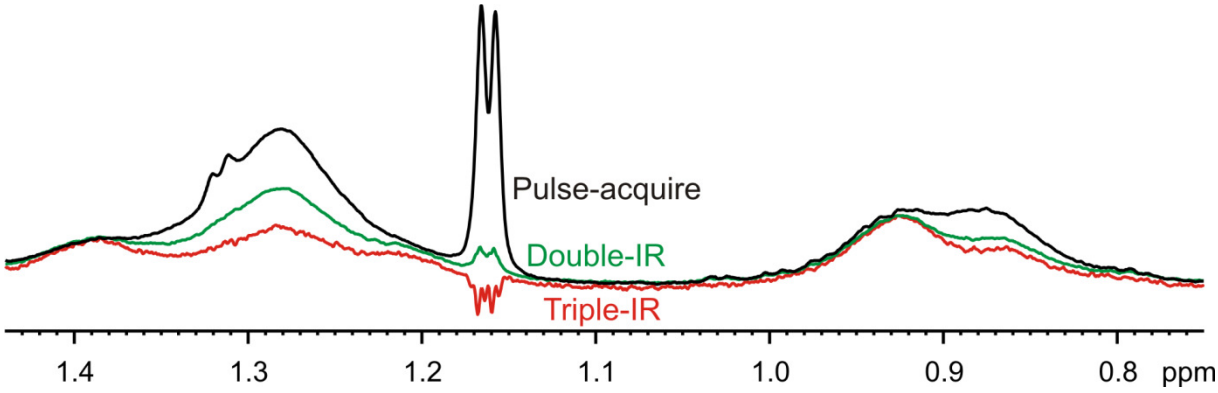

Fig. 5.22 Selective metabolites and mobile lipids attenuation by multiple inversion recovery (MIR) pulse sequences. (Black) Native pulse-acquire spectrum. Acquisition time 10 min, repetition time 9.4 s. **(Green)** Double inversion recovery spectrum, inter-pulse delays 1.71 s and 0.52 s. Acquisition time 42 min, repetition time 5.0 s. **(Red)** Triple inversion recovery spectrum, inter-pulse delays 1.85 s, 1.00 s and 0.31 s. Acquisition time 50 min, repetition time 5.9 s. MIR-spectra were scaled up to match in intensity at mobile protein resonances. T = 5 °C, spectrometer frequency 800 MHz, water suppression: excitation sculpting. 7.9 million NPC embedded in ~200 µl 1 % agarose in PBS containing 50 µM DSS and 10 % D_2O (3-layer-method).

If mobile lipids and mobile proteins exhibit different apparent diffusion coefficients, diffusion-ordered spectroscopy (DOSY) should also faciliate discrimination between these two NMR-visible macromolecular species. Fig. 5.23 unveils that diffusion weighting experiments at very high b-values (gradient coil-limited) yielded an attenuation of mobile protein resonances M1, M2, M3 (referred to as “MP” due to a fixed intensity ratio between M1, M2, M3 during the deconvolution routine), but almost no changes in mobile lipid peaks ML1 and ML2. Fit by an exponentially decaying function, the mobile protein attenuation curve gave an apparent diffusion coefficient of (8 ± 1)E-12 m^2/s. Due to the non-decreasing mobile lipid signals, diffusion coefficients of ML1 and ML2 could not be determined.

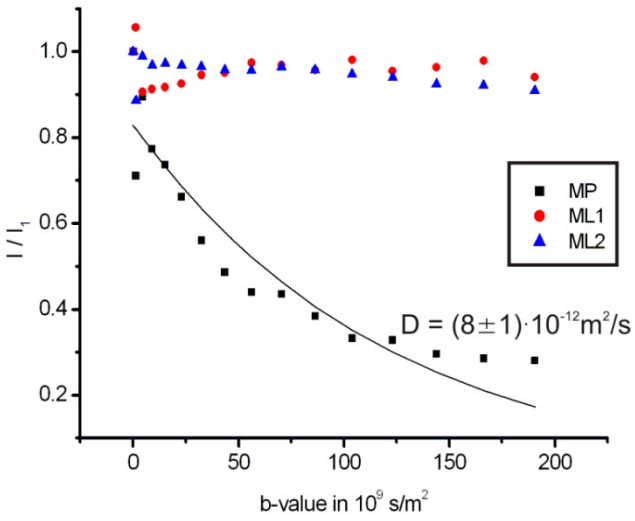

Fig. 5.23 Extensive diffusion weighting to determine diffusion coefficients of NMR-visible macromolecules. Integral values of the deconvolved NMR resonances of mobile lipid and mobile protein residues against b-values. Attenuation curve for mobile proteins was fit by an exponentially decaying function, extracted diffusion coefficient assigned. DOSY parameters: Δ = 100 ms, δ = 10 ms, maximum gradient strength 0.535 T/m, T = 5 °C, 800 MHz, acquisition time 16 x 50 min = 13:33 h:min, repetition time 11.5 s, water suppression: excitation sculpting plus presaturation, pulse program: bipolar pulsed field gradient stimulated echo with longitudinal eddy-current delay (ledbpgp2s). T = 5° C, spectrometer frequency 800 MHz, 7.9 million NPC embedded in ~200 µl 1 % agarose in PBS containing 50 µM DSS and 10 % D_2O (3-layer-method).

Exploiting this difference in diffusion coefficients between mobile lipid and mobile protein resonances, a substraction of a very extensively diffusion-weighted spectrum from a moderately diffusion-weighted spectrum yielded a quasi mobile lipid-free spectrum exhibiting typical features of mobile protein resonances (Fig. 5.24).

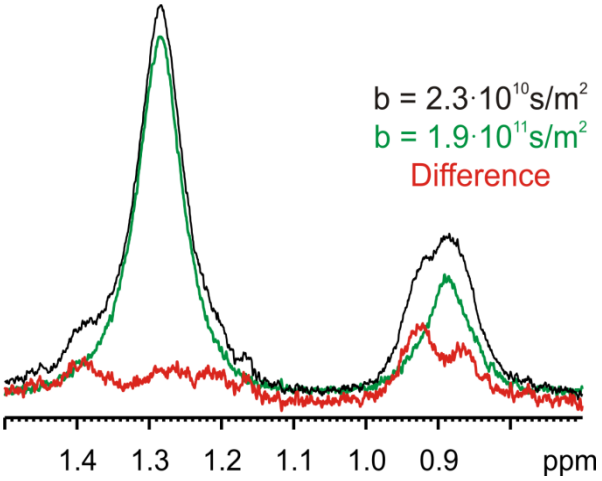

Fig. 5.24 Extensive diffusion weighting to discriminate NMR-visible macromolecules. Moderately and heavily diffusion-weighted NMR spectra plus difference spectrum, b-values assigned. DOSY parameters: Δ = 100 ms, δ = 10 ms, maximum gradient strength 0.535 T/m, acquisition time 16 x 50 min = 13:33 h:min, repetition time 11.5 s, water suppression: excitation sculpting plus presaturation, pulse program: bipolar pulsed field gradient stimulated echo with longitudinal eddy-current delay (ledbpgp2s). T = 5° C, spectrometer frequency 800 MHz, 7.9 million NPC embedded in ~200 µl 1 % agarose in PBS containing 50 µM DSS and 10 % D_2O (3-layer-method).

In Fig. 5.25 the two mobile protein enhancement methods, triple-inversion-recovery (Fig. 5.22) and diffusion weighting (Fig. 5.24) were compared. Diffusion weighting yielded a more pronounced suppression of mobile lipids and small molecule signals. However, for the same number of collected free induction decays (FID), the signal-to-noise ratio (SNR) of the diffusion-weighted difference spectrum was approximately only one third of that obtained by triple-inversion-recovery.

A comparison of the theoretically expected SNR-attenuations of mobile protein resonances with respect to native pulse-acquire spectra gives a value of 0.05 for triple-inversion-recovery (see above and Fig. 5.21) and also about 0.05 for diffusion weighting, the latter being derived as follows:

- factor 0.5 due to stimulated echo loss,
- factor 0.5 due to subtraction (intensity is halved, but noise level remains constant),
- factor ($\exp(-Db_1) - \exp(-Db_2)$) = 0.61 due to an already diffusion-weighted minuend and a not fully mobile protein-free subtrahend,
- factor $\exp(-(\Delta-\delta+LED)/T_1)$ = 0.87 due to T_1-weighting during mixing time (= diffusion time Δ minus duration of bipolar gradient δ) and longitudinal eddy-current delay (LED) of the pulse program "bipolar pulsed field gradient stimulated echo with longitudinal eddy-current delay" (ledbpgp2s),
- factor $\exp(-2\delta/T_2^J)$ = 0.37 due to T_2^J-weighting during the times between the first and the second 90° pulse, and between the third and the forth 90° pulse (mainly twice the bipolar gradient duration δ) of the pulse program (*vide supra*). Using T_2^J instead of T_2 takes into account that - in contrast to within the CPMG sequence - during the spin echo time of the diffusion weighting sequence also J-couplings evolve. These J-coupling phase modulations lead to faster attenuations in case of inhomogeneously broadened resonances. T_2^J of mobile protein resonances was estimated by a conventional spin echo measurement (90° - TE/2 – 180° - TE/2 – acquisition) to about 20 ms, i.e. significantly shorter than T_2 = 62.2 ms ± 0.5 ms (see Fig. 5.19).

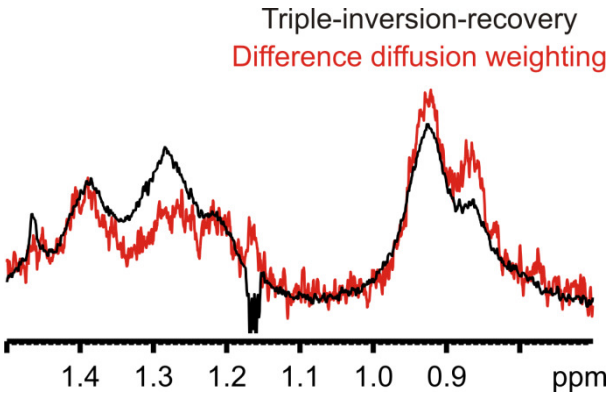

Fig. 5.25 Comparison of methods to discriminate mobile proteins from mobile lipids. (Red) Difference spectrum of diffusion weighting with b-values 1.9E11 s/m^2 and 2.3E10 s/m^2. Parameters given in Fig. 5.24 caption. **(Black)** Delay-optimized triple-inversion-recovery spectrum. Parameters given in Fig. 5.22 caption. Spectra normalized to match in mobile protein intensity.

Concluding the results concerning characterization and discrimination of NMR-visible macromolecules, classical deconvolution strategies for overlapping resonances of different macromolecular species, i.e. mobile lipids and mobile proteins, lost their robustness if one species dominated several fold. In TOCSY spectra, certain non-diagonal regions were specific for mobile proteins and mobile lipids, respectively. Due to differences in relaxation and diffusion behavior among these NMR-visible macromolecules, selective acquisition and evaluation schemes were analyzed for their ability to enable discrimination. Both delay-optimized triple-inversion-recovery and extensive diffusion-weighting allowed selective attenuation of mobile lipid intensities with respect to mobile protein intensities. However, for both methods the SNR loss was at least 95 % compared to conventional pulse-acquire spectra.

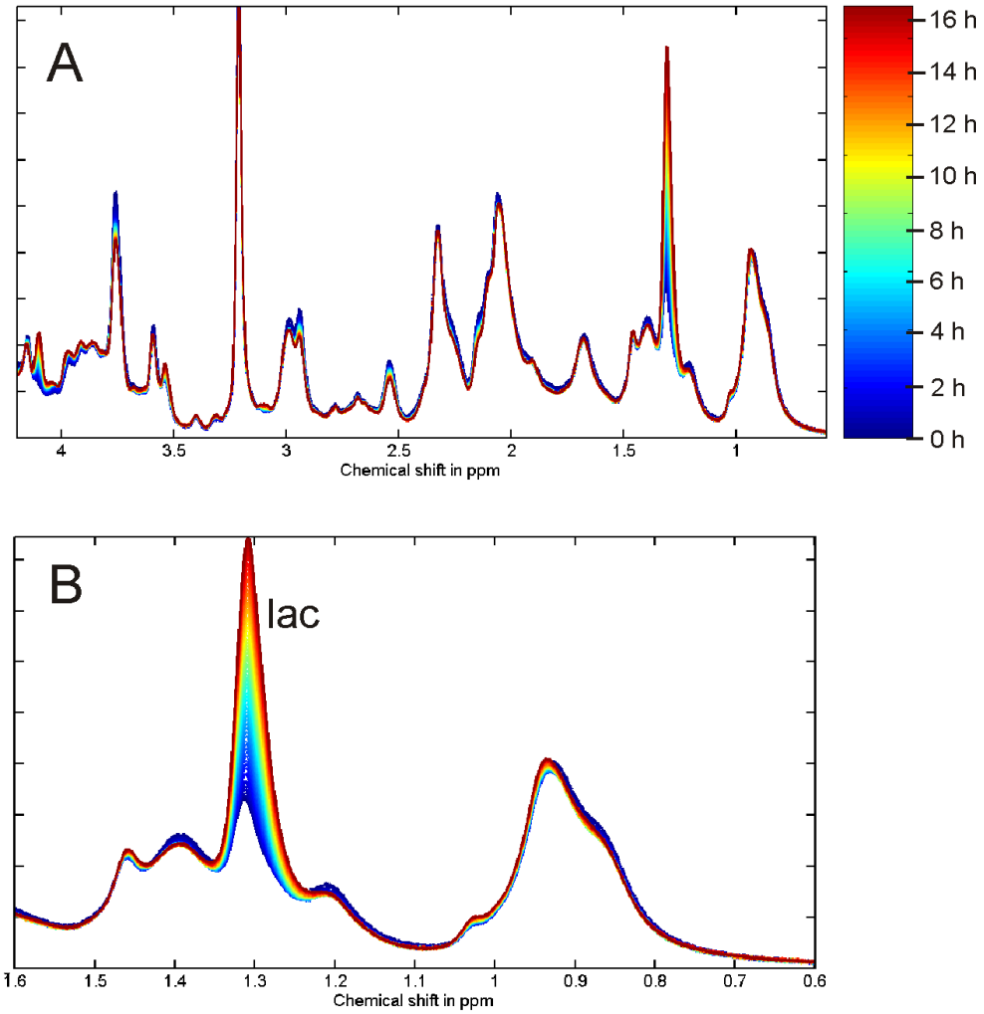

Fig. 5.26 Time-resolved NMR spectra of long-term measurement at 5° C. (A) Time course of NMR spectral changes. Time points are color-coded. Acquisition time 4:28 min:s, repetition time 4.2 s. T = 5° C, spectrometer frequency 800 MHz, water suppression: excitation sculpting. ~5 million GBM-TC (HTZ-349) sedimented in Shigemi plug with 80 µl PBS containing 50 µM DSS and 10 % D_2O. **(B)** Same as (A) but zoomed into lactate region.

5.1.6. Temperature Effects in Time-Resolved Long-Term Measurements

Since NMR tubes are highly unphysiological environments for living cells, e.g. with respect to oxygen and nutrition supply, the effects of long-term measurements on NMR spectra of cell suspensions were investigated at two different temperatures (5° C and 37° C). In order to be able to compare the results, identical samples, i.e. 5 million GBM-TC (HTZ-349) in customized Shigemi plugs, and similar acquisition parameters were employed.

At 5° C (Fig. 5.26) most resonance intensities remained virtually constant for at least 16 hours. Minor exceptions were slight decreases of GSH (2.55 ppm), glx (3.75 ppm) and mobile proteins. The only major change exhibited lactate (1.31 ppm) which increased linearly to about five times the initial intensity.

In contrast, at 37° C (Fig. 5.27) the majority of resonances increased rapidly and vigorously. In addition, also signs of mobile lipids could be detected. In this cell line mobile lipid resonances have never been detected at 5° C, but the resonances obtained here by heating showed indeed similar chemical shift values of typical ML1, ML2 and ML3 signals at 5° C. This finding rendered statements about pure lactate somewhat doubtful. Therefore, the sum of lactate and ML2 was investigated. In Fig. 5.28, the temporal evolution of the deconvolved signals of free alanine, mobile protein M1 – M3, and the sum of lactate and mobile lipid ML2 is depicted. Alanine (and other amino acids, data not shown) increased quasi linearly until the end of the experiment, at which the alanine concentration was ten times its starting value. In contrast, lactate and mobile lipids showed an initial increase, but reached a saturation level already after 2-3 h. As expected from Fig. 5.27, mobile protein signals did not change significantly.

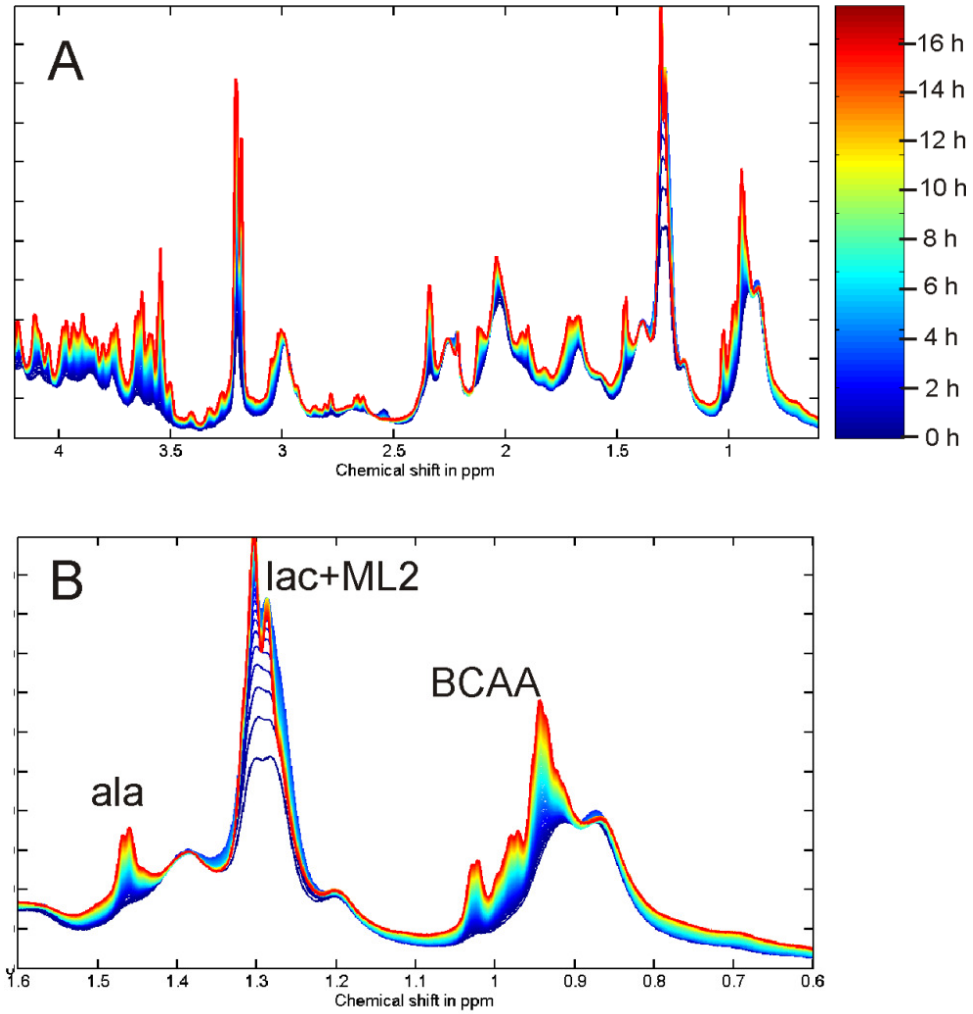

Fig. 5.27 Time-resolved NMR spectra of long-term measurement at 37° C. (A) Time course of NMR spectral changes. Start time points are color-coded. Acquisition time 4 min, repetition time 3.75 s. T = 37° C, spectrometer frequency 800 MHz, water suppression: excitation sculpting. ~5 million GBM-TC (HTZ-349) sedimented in Shigemi plug with 80 µl PBS containing 50 µM DSS and 10 % D_2O. **(B)** Same as (A) but zoomed into lactate region.

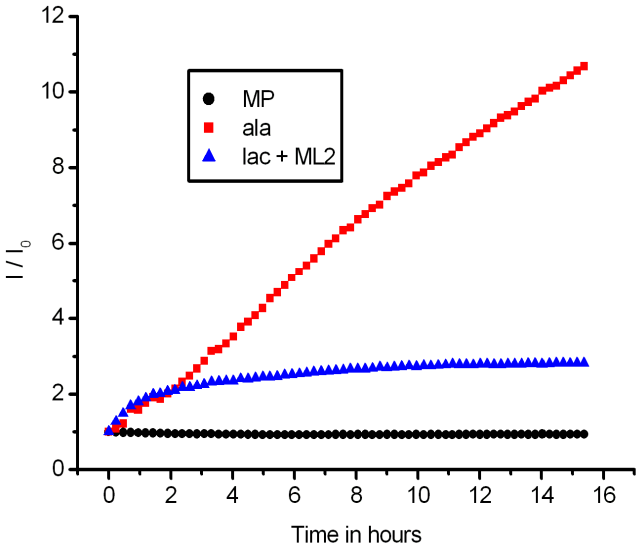

Fig. 5.28 Time course of deconvolved NMR signals of long-term measurement at 37° C. "MP": Mobile protein peaks M1 – M3. "ala": Free alanine. "lac + ML2": Sum of lactate and mobile lipid peak ML2. Acquisition time 4 min, repetition time 3.75 s. T = 37° C, spectrometer frequency 800 MHz, water suppression: excitation sculpting. ~5 million GBM-TC (HTZ-349) sedimented in Shigemi plug with 80 µl PBS containing 50 µM DSS and 10 % D_2O.

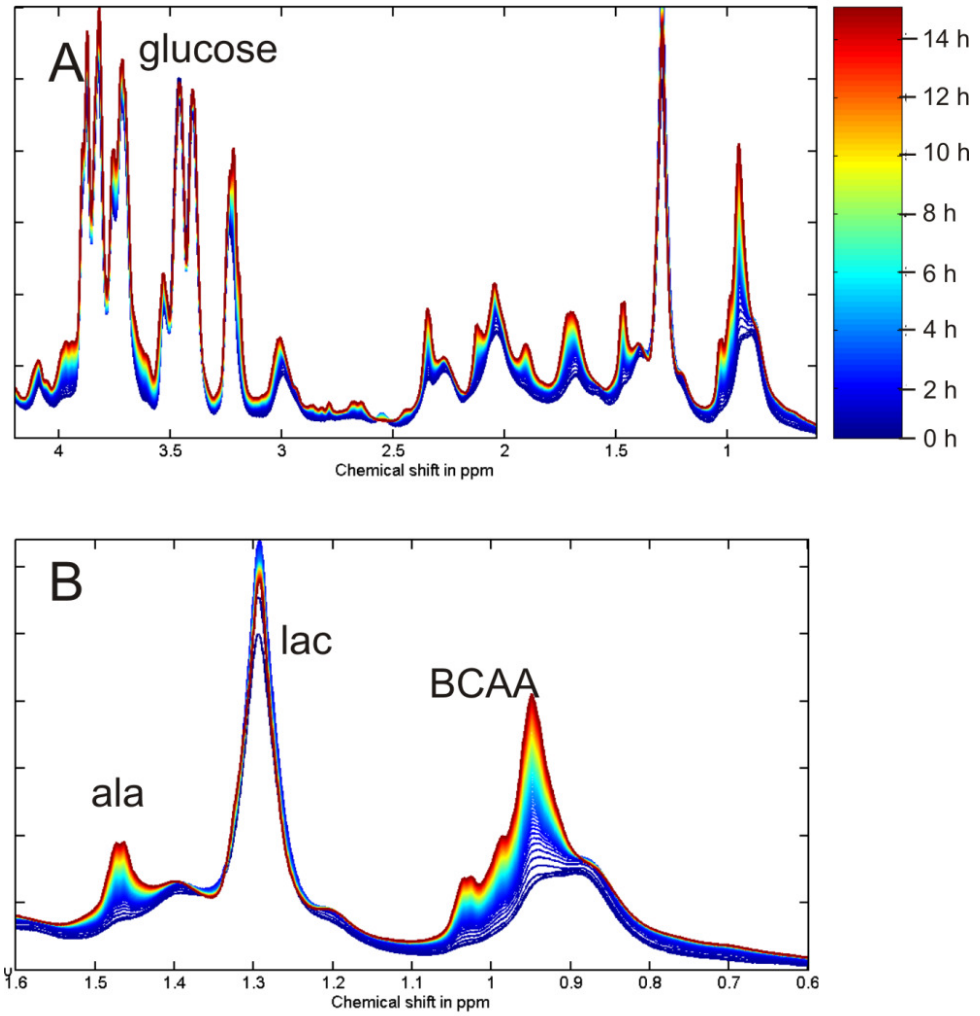

Fig. 5.29 Time-resolved NMR spectra of long-term measurement at 37° C with 25 mM glucose. (A) Time course of NMR spectral changes. Time points are color-coded. Acquisition time 4 min, repetition time 3.75 s. T = 37° C, spectrometer frequency 800 MHz, water suppression: excitation sculpting. ~5 million GBM-TC (HTZ-349) sedimented in Shigemi plug with 80 µl PBS containing 50 µM DSS, 25 mM glucose and 10 % D_2O. **(B)** Same as (A) but zoomed into lactate region.

The same experiment but with addition of 25 mM glucose (Fig. 5.29) yielded similar results regarding amino acid signal increases, but here unambiguous signs for mobile lipids were missing. Also the lactate peak did not increase significantly. Importantly, glucose signals did not decrease, i.e. there was no glucose consumption by the cells.

Notably, when switching the temperature from 5° C to 37° C and back to 5° C (Fig. 5.30), mobile lipid signals (at positions of ML1, ML2 and ML3) appeared and increased rapidly at 37° C and decreased again at 5° C, but did not disappear completely. This irreversibility was observed most strikingly in case of ML1 in diffusion-weighted spectra (marked with green arrows in Fig. 5.30).

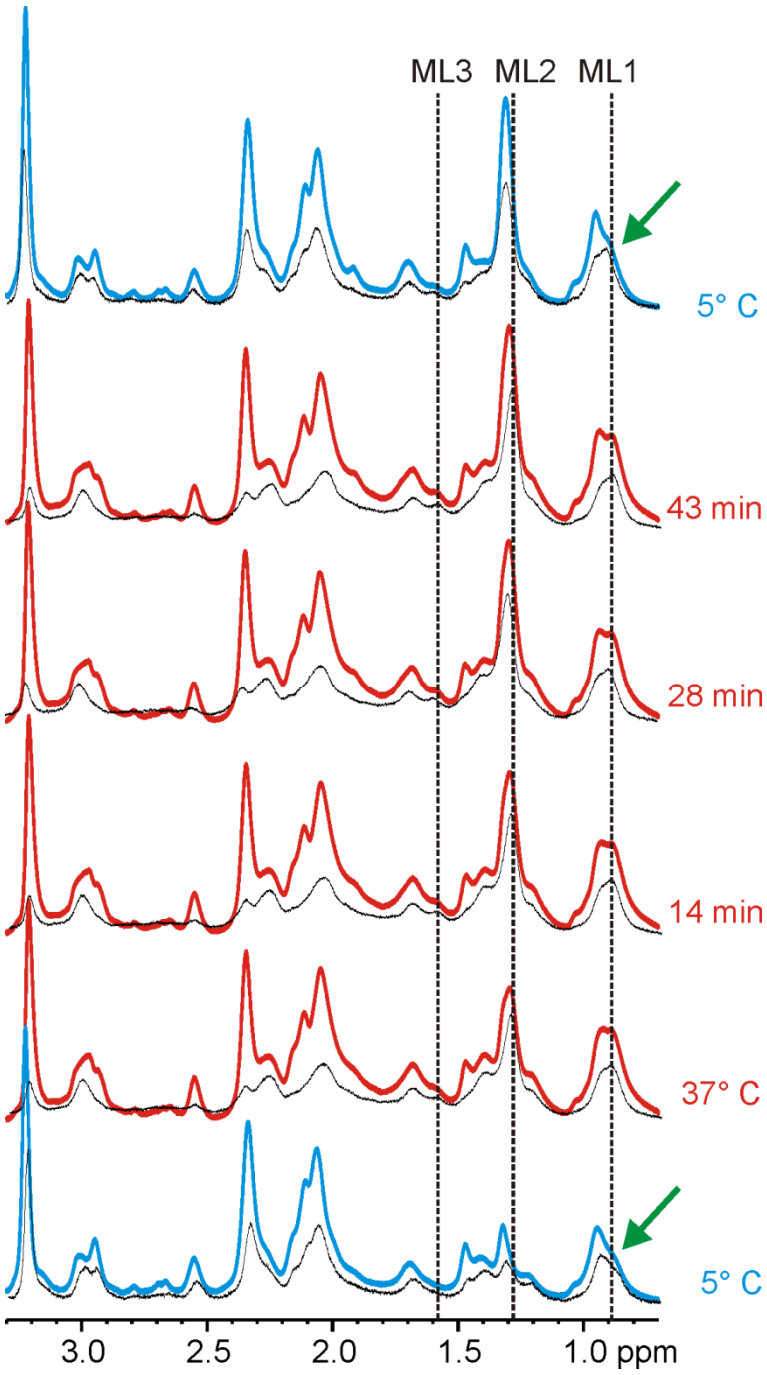

Fig. 5.30 Temperature effects after rapid heating from 5° C to 37° C and back. (Blue and red) Pulse-acquire NMR spectra. Acquisition time 4 min, repetition time 3.75 s. (Black) Corresponding diffusion-weighted spectra. Time axis from bottom to top. Mobile lipid resonances ML1 - ML3 assigned. Green arrow indicates irreversibly heat-induced signal ML1. Acquisition time 2:54 min:s, repetition time 1.9 s. b-value 1.1E10 s/m^2, Δ = 20 ms, δ = 6 ms, gradient strength 0.48 T/m, pulse program: bipolar pulsed field gradient stimulated echo with longitudinal eddy-current delay (ledbpgp2s1d), spectrometer frequency 800 MHz, water suppression: excitation sculpting. ~5 million GBM-TC (HTZ-349) sedimented in Shigemi plug with 80 µl PBS containing 50 µM DSS and 10 % D_2O.

Concluding the results of long-term NMR spectroscopy of cell suspensions, at 5° C the NMR-spectral alterations with time were mainly limited to an increase in lactate in the order of five times the initial value within 16 hours. In contrast, at 37° C severe increases in free amino acid resonances and appearances of lipid signals could be observed even in cell lines reproducibly lacking mobile lipids at 5° C. These temperature-induced lipid resonances did not disappear completely by recooling to 5° C. Additional glucose was not consumed by the cells but prevented strong mobile lipid and lactate increases.

5.2. Mobile Lipids in Brain-Derived Stem- and Tumor Cells

In the following section the focus is on results that shed a little more light on the interrelation between NMR-visible mobile lipid signals and biological aspects, in particular cell culture conditions and viability on the one hand, and stem cell identity on the other hand. Depending on the study, rodent fetal neural progenitor cells (NPC), bone marrow-derived mesenchymal stem cells (MSC), COS7 fibroblasts, and adult human glioblastoma multiforme (GBM)-derived cell lines were used, the latter being both cultured in medium containing serum (GBM-tumor cells, GBM-TC) and in serum-free medium (brain tumor initiating cells, BTIC).

5.2.1. Dependence on Culturing Period and Apoptosis

In this study the NMR-visible mobile lipid content of NPC was investigated. The appearance of these mobile lipids as well as their possible connection to cell culture confluence and apoptosis was analyzed and compared to results obtained in other cell lines. Cell culture and biological assays were performed by Sonja Plötz (LDH-assay, cell culture), Monika Krampert (Menadion treatment), and Francisco Rivera (MSC cell culture), all previous members of the group.

In Fig. 5.31 phase-contrast micrographs of cultured NPC are shown. During culture periods that are established for stem cell investigations under physiological conditions, i.e. until day 5 in culture, small cell clusters formed, so-called “neurospheres” characteristic for NPC culture.

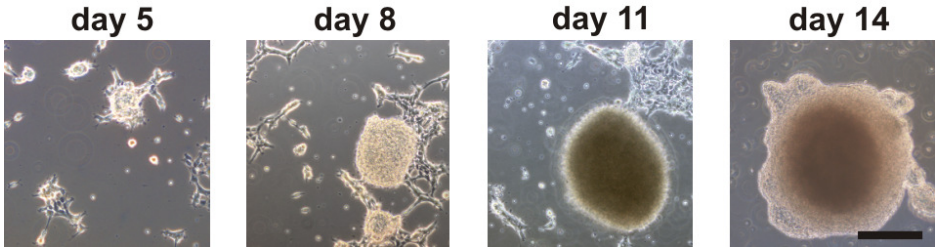

Fig. 5.31 Phase-contrast micrographs of NPC at different days in culture. Scale bar: 200 µm.

Under this established physiological cell culture conditions, virtually no mobile lipid signals could be detected in cell suspension NMR spectra (Fig. 5.32, bottom spectrum). However, when the culture period was elongated from 5 days to 8, 11 and up to 14 days, neurospheres grew continuously up to 0.5 mm in diameter (Fig. 5.31) and cell culture phenotypes transformed from log-phase via confluence to post-confluence. In parallel, mobile lipid resonances (e.g. ML2) appeared and increased continuously.

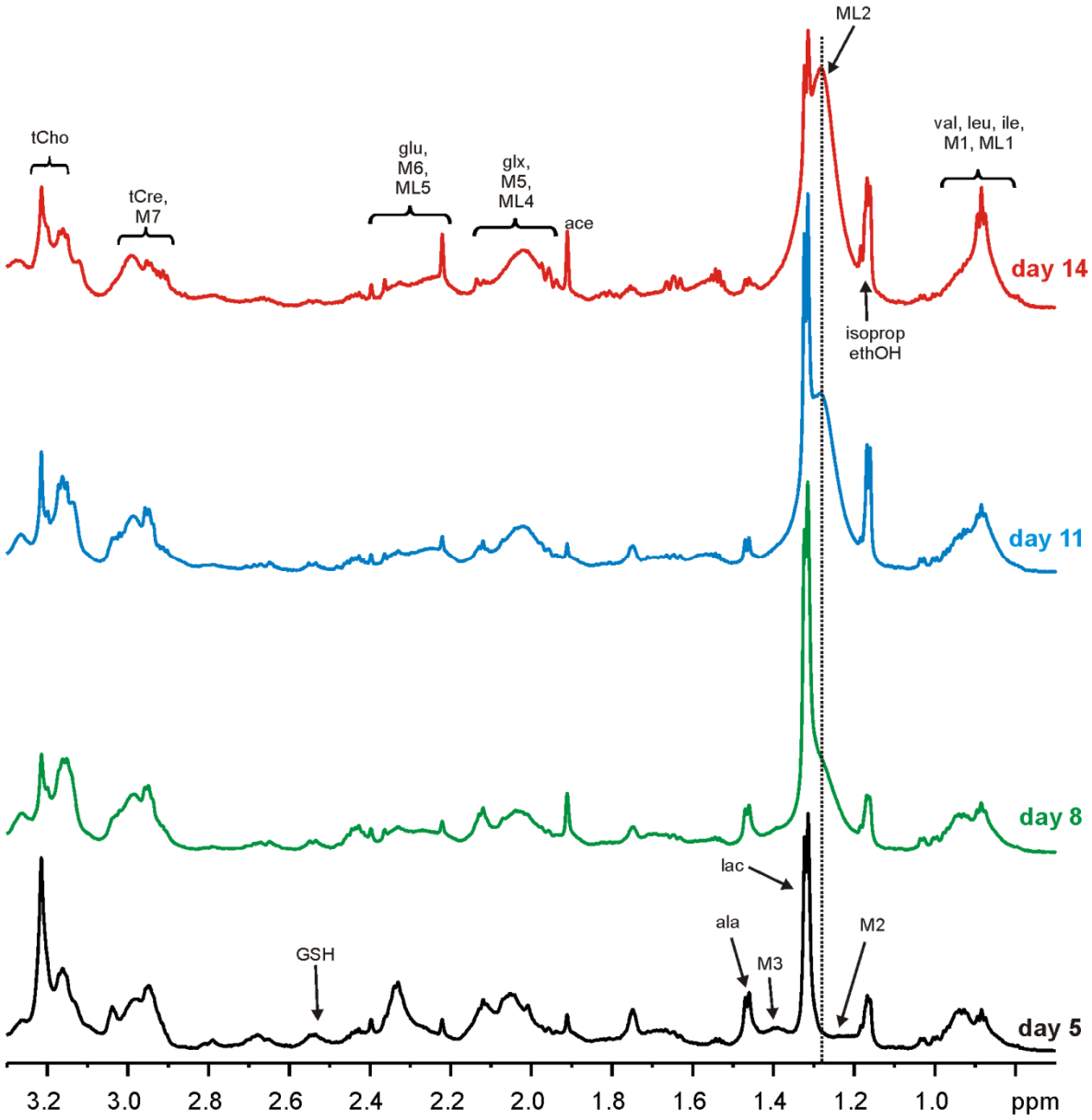

Fig. 5.32 NMR spectral changes during elongated culturing. NMR spectra of NPC at day 5, 8, 11 and 14 in culture. Dotted line: Mobile lipid ML2 resonance. Scaled up to match in mobile protein intensity. Acquisition time 5 min, repetition time 4.75 s, T = 5° C, spectrometer frequency 800 MHz, water suppression: excitation sculpting plus presaturation. 10-20 million NPC embedded in 600 µl 1 % agarose in PBS containing 40 µM DSS and 10 % D_2O. Assignment and abbreviations according to **Tab. 5.1**.

The quantification of the mobile lipid signals was conducted as described in section 4.5 and yielded highly significant increases during elongated culturing of NPC (Fig. 5.33 A). This phenomenon could also be reproduced in other cell lines, namely in COS7 fibroblasts, which constituted non-neural and non-stemlike control cells, and in MSC, which served as a non-neural stem cell control (Fig. 5.33 B). Notably, mobile lipid resonances have never been found in freshly disected murine fetal forebrains.

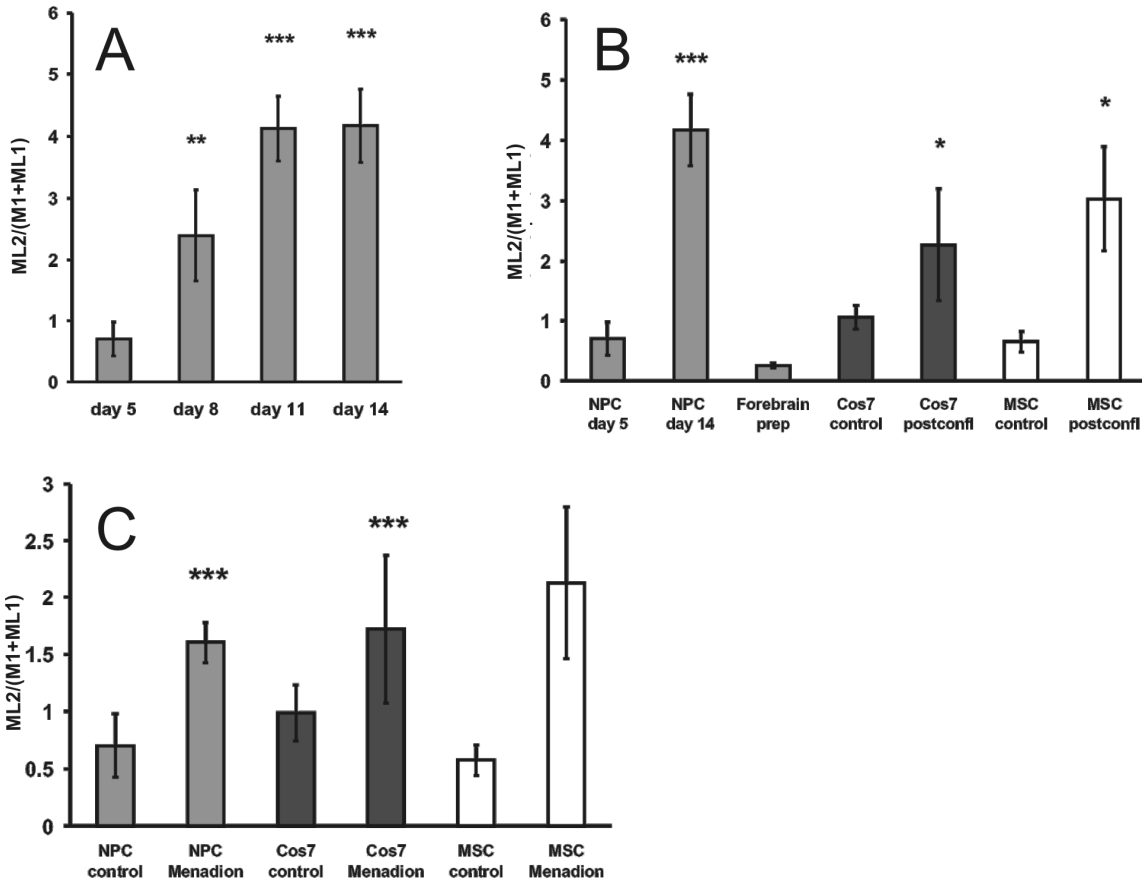

Fig. 5.33 Mobile lipid dependence on culturing period, cell type, and apoptosis. Quantified mobile lipid resonance ML2/(M1+ML1). **(A)** Dependence on culturing period. NPC at day 5, 8, 11 and 14 in culture. (N ≥ 4) **(B)** Dependence on cell type. NPC (N ≥ 3), COS7 fibroblasts (N = 6), MSC (N = 3), each both at *de visu* pre- and postconfluence, and freshly prepared fetal forebrains (N = 3). **(C)** Mobile lipid increase during induction of apoptosis by Menadion. Control conditions: Day 5 for NPC (N ≥ 4), *de visu* pre-confluence for COS7 cells (N = 6) and MSC (N ≥ 2) . All cells embedded in 600 µl 1 % agarose in PBS containing 40 µM DSS and 10 % D_2O. Statistical means (bar heights) and standard deviations (error bars) depicted. Student's t-test significance levels: * $p < 0.05$, ** $p < 0.01$, *** $p < 0.001$.

In parallel to the NPC measurement series, cell death was quantified via detection of lactate dehydrogenase (LDH) within the cell culture. A correlation coefficient of 0.74 was obtained between NMR-detected mobile lipids and biological LDH assay outcomes.

In vitro induction of apoptosis by treatment with Menadion under control conditions (e.g. at day 5 for NPC) also resulted in mobile lipid increase (Fig. 5.33 C). Although these apoptosis-linked mobile lipid increases were smaller than those obtained upon postconfluence, at least in NPC and COS7 cells the changes were statistically highly significant.

5.2.2. Modulations upon TGF-β Treatment

This section deals with alterations in confluence-induced mobile lipid contents caused by treatment with two subclasses of transforming growth factor β, namely TGF-β1 and TGF-β2. Examined cell lines were grown until *de visu* confluence was reached in the untreated control samples. Cell culture and biological assays were performed by Dr. Arabel Vollmann-

Zwerenz (flow cytometry), Birgit Jachnik (cell culture) and Petra Leukel (cell culture), all members of the group.

The results of this study are summarized in Fig. 5.34. Decreases in mobile lipid content upon TGF-β treatment were found in NPC and in one GBM-TC line, HTZ-417. Whereas this decrease was tested significant in GBM-TC HTZ-417, in NPC the content of mobile lipids varied profoundly between the reproducing measurement series, thus solely yielding an (almost significant) trend ($p = 0.055$) in case of TGF-β1 treatment. In contrast, the BTIC line R49 exhibited an increase of mobile lipids upon TGF-β treatment, which was calculated to be statistically highly significant in case of TGF-β2. Regarding the other two investigated GBM-TC lines, HTZ-349 distinguished itself by a general absence of mobile lipids, whereas in GBM-TC U87 mobile lipids could be detected under every condition, but variations upon TGF-β treatment were small if at all.

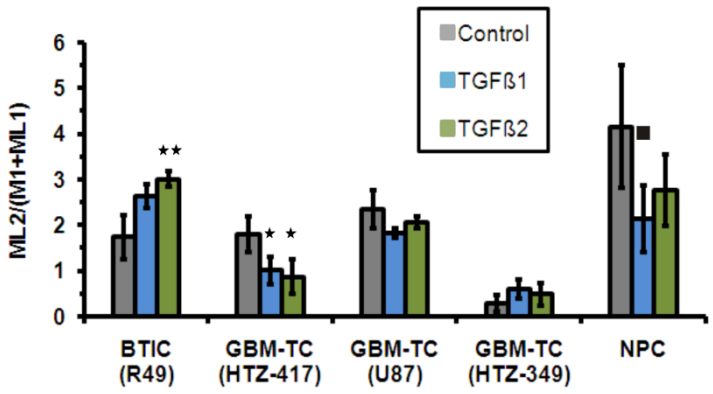

Fig. 5.34 Mobile lipid dependence on transforming growth factor TGF-β 1 and 2 treatment. Quantified mobile lipid resonance ML2/(M1+ML1). 3-10 million BTIC (N = 4), GBM-TC (U87: N = 2, HTZ-349: N = 3, HTZ-417: N = 4) or NPC (N = 4) resuspended in 10 µl – 50 µl PBS with 50 µM DSS and 10 % D_2O and sedimented in costumized Shigemi plugs. T = 5° C, spectrometer frequency 600 MHz or 800 MHz, acquisition time 3.2-4.3 min, repetition time 3-4 s, water suppression: excitation sculpting. Statistical means (bar heights) and standard deviations (error bars). Student's t-test significance levels: ■ $p = 0.055$, * $p < 0.05$, ** $p < 0.01$, *** $p < 0.001$.

Notably, despite the different response of BTIC R49 and GBM-TC HTZ-417 to TGF-β treatment, the mobile lipid content in both cell lines was linked negatively to the percentage of cells in cell cycle S-phase (Fig. 5.35) as determined by parallel flow cytometry on DNA-content. Linear regression yielded correlation coefficients of -0.51 and -0.79 for BTIC R49 and GBM-TC HTZ-417, respectively, the latter being statistically significant.

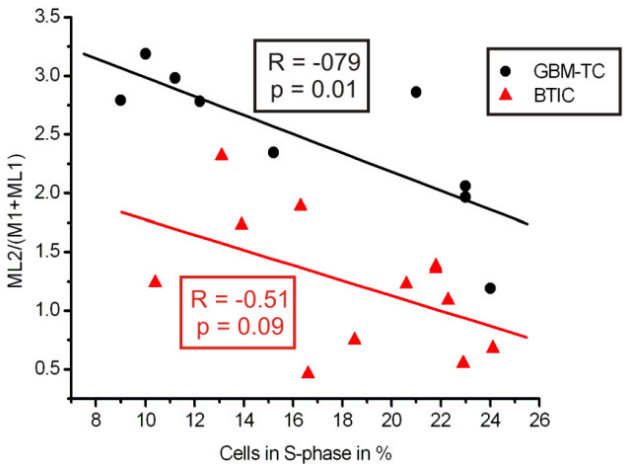

Fig. 5.35 Mobile lipid dependence on percentage of S-phase cells. Quantified mobile lipid resonance ML2/(M1+ML1) plotted against percentage of cells in cell cycle S-phase (determined by fluorescence-activated cell sorting on DNA-content). (Black) GBM-TC HTZ-417. (Red) BTIC R49.

5.2.3. Correlations to Stemness

In this section, the results of a study are presented which addressed a possible link between NMR-visible mobile lipid resonances and stemness of BTIC. Cell culture and biological assays were performed by Dr. Christoph Beier (flow cytometry, clonogenicity assay), Marc Bettschneider (flow cytometry, clonogenicity assay, cell culture) and Birgit Jachnik (cell culture, clonogenicity assay), all former or current members of the group.

Ten different BTIC lines were investigated in two measurement series, e.g. N = 20, by cell suspension NMR spectroscopy and in parallel by biological assays addressing proposed BTIC-specific features, i.e. the expression of the surface marker CD133 on the one hand, and cloning efficacy (the ability to form new clones from single cells) on the other hand. The former was quantified by means of flow cytometry, the latter by a clonogenicity assay, both introduced in Methods section 4.1.

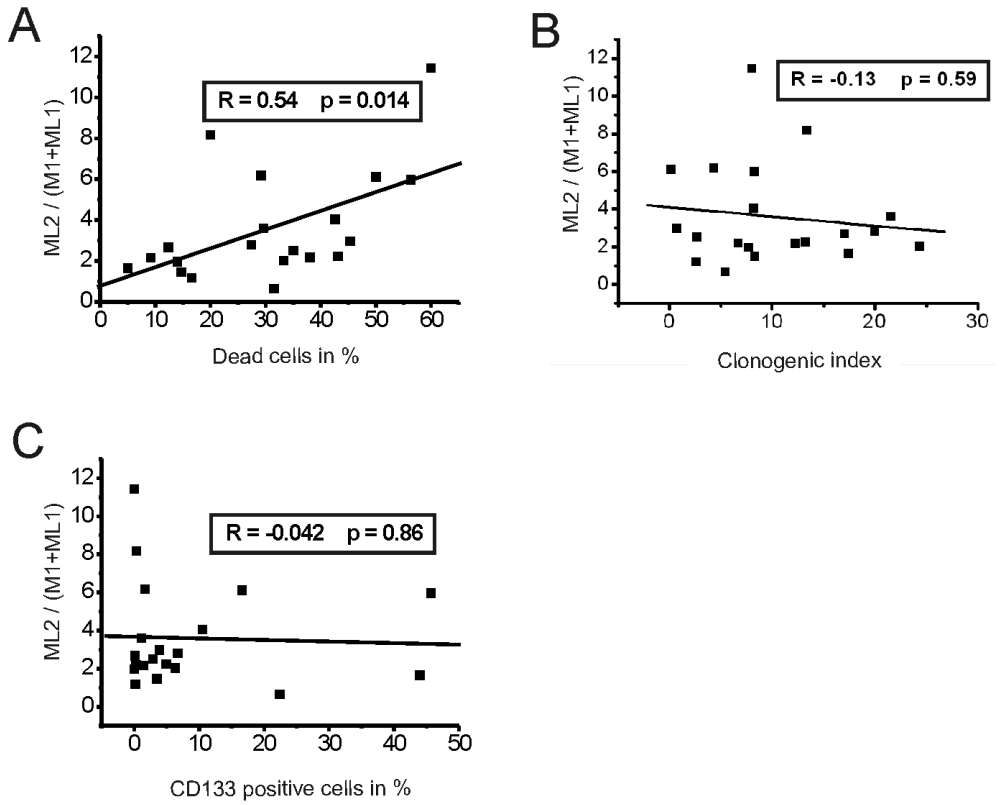

Fig. 5.36 Mobile lipid dependence on stemness and cell death in BTIC. Quantified mobile lipid peak ML2/(M1+ML1) of 20 BTIC spectra (20 samples, 2 x 10 different BTIC lines) plotted against biological assay outcomes. **(A)** Percentage of dead cells. **(B)** Clonogenic index. **(C)** Percentage of CD133 positive cells. Solid lines represent linear regression, correlation coefficients (R) and corresponding p-values assigned. 3-5 million cells in 550 µl PBS containing 40 µM DSS and 10 % D_2O resuspended in 5 mm Shigemi tube. Acquisition time 5 min, repetition time 4.75 s, T = 5° C, spectrometer frequency 600 MHz or 800 MHz, water suppression: excitation sculpting plus presaturation.

From Fig. 5.36 B and C the absence of significant correlations between mobile lipids and clonogenic index, i.e. the percentage of clone-forming cells in %, as well as to the percentage of CD133-positive cells is evident. Additionally, the percentage of dead cells within the sample was measured in parallel by flow cytometry (propidium iodide). A significant positive linear connection with a correlation coefficient of 0.54 was found (Fig. 5.36 A).

Concluding this part of the results chapter, in Tab. 5.2 the findings of mobile lipid measurements in brain-derived stem- and tumor cells and control cells (MSC, COS7 fibroblasts) are summarized.

Mobile lipids	**Throughout**	**Increase by postconfluence**	**Increase by apoptosis (Menadion)**	**Changes upon TGF-β**	**Correlation to cell death**	**Correlation to S-phase**
NPC	no	yes	yes	decrease	yes, positiv	n.d.
GBM-TC HTZ-417	no	yes	n.d.	decrease	n.d.	yes, negative
GBM-TC HTZ-349	no	no	n.d.	no	n.d.	n.d.
GBM-TC U87	almost	heterogeneous	n.d.	n.s., decrease	n.d.	n.d.
BTIC R49	yes	yes	n.d.	increase	n.d.	yes, negative
BTIC in general	no	n.d.	n.d.	n.d.	yes, positive	n.d.
COS7 fibroblasts	no	yes	yes	n.d.	n.d.	n.d.
MSC	no	yes	n.s.	n.d.	n.d.	n.d.

Tab. 5.2 Summarized results of mobile lipids in brain-derived stem- and tumor cells and control cells. n.d. = not determined, n.s. = not significant (trend), "BTIC in general" = without discriminating between different BTIC lines.

5.3. Mobile Lipids in LDL-Loaded Macrophages

In this section, the results of a small study on macrophages are presented, in which changes in NMR-visible lipid content upon loading with low-density lipoproteins (LDL) were investigated. Apart from native LDL, also enzymatically degraded LDL (E-LDL) and LDL oxidized by copper(II) sulfate (Ox-LDL) were used for LDL-loading. A short overview of this treatment including references is given in section 4.1.

The first part of this section deals with NMR spectra of pure LDL samples, i.e. native LDL, E-LDL and Ox-LDL. In the second part, NMR-visible influences of LDL-loading on NMR spectra of macrophage suspensions are described.

LDL-extractions, macrophage cell culture, LDL-loadings, cell harvesting and determination of LDL protein contents was conducted by Dr. Margot Grandl, a former fellow of the Institute of Clinical Medicine of Prof. Schmitz, University of Regensburg.

5.3.1. NMR-Visibility of Fatty Acid Moieties of LDL-Species

In Fig. 5.37, representative NMR spectra of LDL samples are depicted. Native LDL (black) showed prominent lipid signals, even at 0.66 ppm, i.e. at the chemical shift of the cyclopentane methyl group of cholesterol (chol). However, in NMR spectra of Ox-LDL (green), lipid resonances were very weak, and in spectra of E-LDL (red), lipid signals could not be detected at all. It is important to note that the NMR spectra were scaled to the protein content (apoB) within LDL that was determined before (!) degradation or oxidation. In other words, the scaling of the NMR spectra is according to the total amount of lipids within LDL before enzymatic or oxidative treatment.

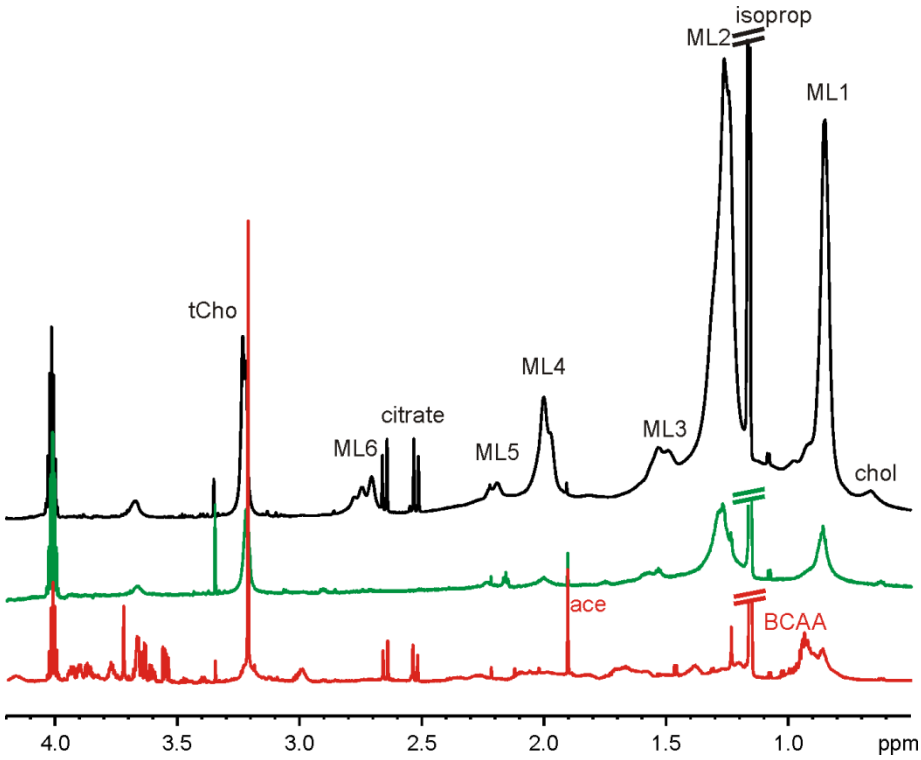

Fig. 5.37 Representative NMR spectra of LDL-species. (Black) Native LDL, 2.8 mg protein per ml. **(Green)** Ox-LDL, 0.9 mg protein per ml. **(Red)** E-LDL, 2.0 mg protein per ml. Spectra scaled according to protein density. 500 µl LDL suspension plus 50 µl 0.5 µM DSS in D_2O, T = 25° C, spectrometer frequency 800 MHz, acquisition time 8:16 min:s, repetition time 7.75 s, water suppression: 5 s presaturation at 45 dB power (1d noesy pulse program: noesygppr1d). Abbreviations according to **Tab. 5.1**.

Especially in NMR spectra of E-LDL, also mobile protein resonances M1 – M7 could be determined. However, in contrast to native LDL and Ox-LDL, clearly detectable amino acid signals, e.g. of valine, leucine, isoleucine (BCAA) and alanine (ala), point to a partial degradation of proteins in E-LDL samples. Furthermore, only in the case of E-LDL, the spectral region of choline compounds (tCho) was dominated by a sharp resonance, whereas for native and oxidized LDL, a broad peak was visible.

5.3.2. NMR Spectra of Macrophages Loaded with LDL, Ox-LDL, and E-LDL

In Fig. 5.38, representative NMR spectra of macrophage suspensions are presented. Native macrophages (black) were compared to LDL-loaded ones, either loaded with native LDL (green), Ox-LDL (red) or E-LDL (blue). NMR spectra of native macrophages showed typical features of cell suspension NMR spectra, which have already been described in detail in section 5.1.1, notably also mobile lipid resonances. In case of LDL-loading with native and oxidized LDL, the spectral appearance remained constant despite a slight increase in mobile lipid signals upon native LDL, and a general macromolecular line broadening upon Ox-LDL (note: copper sulfate is paramagnetic). However, all investigated macrophage samples that had been loaded with E-LDL (N=3) showed a very prominent increase of mobile lipids, at least ten times higher than without LDL-loading or with native / oxidized LDL-loadings.

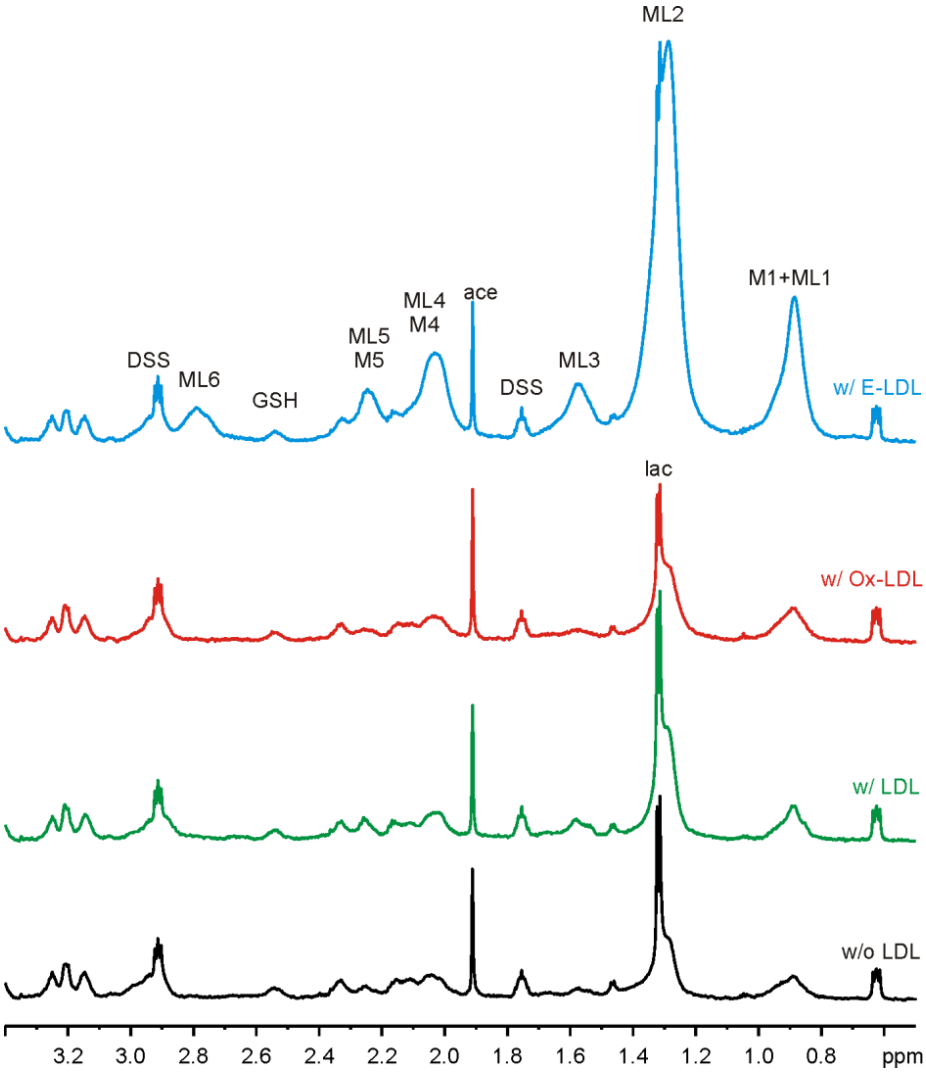

Fig. 5.38 NMR spectra of macrophage suspensions. (Black) Native macrophages without LDL loading. **(Green)** Macrophages loaded with native LDL. **(Red)** Loaded with Ox-LDL. **(Blue)** Loaded with E-LDL. 3 – 10 million macrophages resuspended in 550 µl PBS containing 10% D_2O and 40 µM DSS, T = 5° C, spectrometer frequency 800 MHz, acquisition time 5 min, repetition time 4.75 s, water suppression: excitation sculpting plus presaturation. Abbreviations according to **Tab. 5.1**. Spectra scaled up to match in mobile protein intensity.

Apart from the profound increase in mobile lipid content upon loading with E-LDL, additional changes in the relative intensities of the mobile lipid resonances were determined (Fig. 5.39). Normalized to the spectral region of ML2, a clear relative increase of the signal ML6 was found. Thus, the saturation degree changed from a partial monounsaturation (ML6 not detectable, but peak at 5.3 ppm not vanishing) to a considerable polyunsaturation (ML6 high and peak at 5.3 ppm increased).

In conclusion of the results on mobile lipids in macrophages and their induction by loading with different LDL-species, in NMR spectra of native LDL and to a minor extent of Ox-LDL, lipid resonances were detected, however, the induction of mobile lipids in macrophages loaded with native LDL or Ox-LDL was only marginal. In contrast, E-LDL did not show any lipid resonances, but it induced a profound increase of mobile lipids in macrophages that had been loaded with E-LDL. Additionally, also the saturation degree of fatty acid chains of mobile lipids changed upon loading with E-LDL, from a minor mono-unsaturation to a clear poly-unsaturation. Further robust quantitative analyses were not possible, since (1) both

macromolecular and metabolite lineshapes varied considerably between the measurement series (N=3), and (2) at least in one NMR spectrum there was clear evidence of cholesterol/cholesterol-ester, which would urge for an incorporation of the cholesterol resonances in the deconvolution procedure, which in turn has not been established yet. In addition, a model-free quantification method, e.g. based on integration, would neither yield reliable results, since almost all peaks of interest overlapped with a myriads of further peaks that – to make things even worse - varied much in intensity between the measurement series.

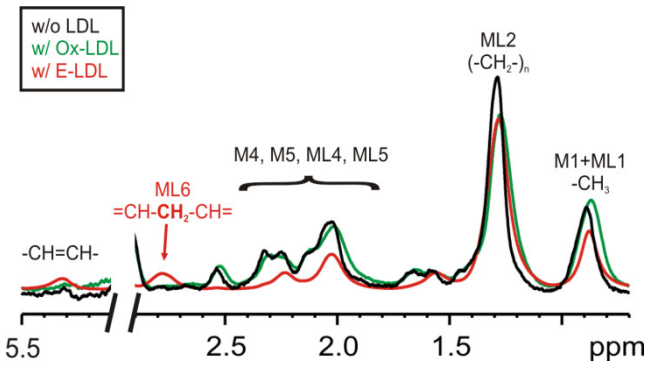

Fig. 5.39 Different saturation degree of mobile lipid fatty acids in macrophages upon loading with E-LDL. Diffusion-weighted NMR-spectra of native and Ox-LDL/E-LDL-loaded macrophages. Scaled to fit in intensity in the spectral range of ML2. **(Black)** Native macrophages. **(Green)** Macrophages loaded with Ox-LDL. **(Red)** Loaded with E-LDL. 3 – 10 million macrophages resuspended in 550 µl PBS containing 10% D_2O and 40 µM DSS. Diffusion-weighting: b-value 1.1E10 s/m^2, Δ = 20 ms, δ = 6 ms, gradient strength 0.48 T/m, pulse program: bipolar pulsed field gradient stimulated echo with longitudinal eddy-current delay, T = 5° C, spectrometer frequency 600 MHz, acquisition time 3:38 min:s, repetition time 1.7 s, water suppression: excitation sculpting. Abbreviations according to **Tab. 5.1**.

5.4. Statistical Analyses of NMR-Signatures and Biological Assay Outcomes of Brain Tumor Initiating Cells

In the following section the results of a biomarker screening pilot study are presented. In this study, NMR spectra of brain tumor initiating cells (BTIC) were compared to biological quantities relevant for stem cell characterization, i.e. clonogenicity and CD133, and to the percentage of cell death, by means of statistical analyses, i.e. principal component analysis and correlation analyses.

Cell samples, NMR-spectral data and biological assay outcomes were those already presented in section 5.2.3, but the evaluation was altered from a classical investigation of one single NMR-spectral resonance, i.e. ML2, to analyses of the total spectral range between 0.7 ppm and 4.2 ppm in order to screen for possible biomarker resonances or resonance patterns specific for stemness.

Already mentioned in section 5.2.3, cell culture and biological assays were performed by Dr. Christoph Beier (flow cytometry, clonogenicity assay), Marc Bettschneider (flow cytometry, clonogenicity assay, cell culture) and Birgit Jachnik (cell culture, clonogenicity assay), all former or current members of the group.

Ten different BTIC lines were investigated in two measurement series, e.g. N = 20, by cell suspension NMR spectroscopy and in parallel by biological assays addressing proposed BTIC-specific features, i.e. the expression of the surface marker CD133 on the one hand, and the ability to form new clones from single cells on the other hand. The former was quantified by means of flow cytometry, the latter by a clonogenicity assay, both introduced in section 4.1.

5.4.1. Principal Component Analysis

In Fig. 5.40 the outcomes of the principal component analyses of the twenty NMR spectra of ten different BTIC-lines are presented. From the scores plot of the first and second principal components (PC) broken down to the individual BTIC lines (Fig. 5.40 A), relatively small distances among the duplets of each BTIC line could be observed. In other words, PCA detected that NMR spectra of the first and the second sample of each BTIC line were considerably similar. Additionally, in a subset of samples with percentages of viable cells higher than 60 %, i.e. omitting six samples in which more than 40 % of the cells were dead (N = 6), the scores plot of PC 1 and 3 broken down to high and low clonogenicity, i.e. higher and lower than the median (10.32 %), yielded a moderated clustering (Fig. 5.40 B), in which low clonogenicity samples showed higher PC 1 and/or PC 3 values. Clusterings in other scores plots, neither in other principal components nor broken down to CD133 or cell death, were not found for the first five principal components. The loadings plot (Fig. 5.40 C) revealed that PC 1 was dominated by mobile lipid resonances (contributing negatively), choline compounds (tCho) and myo-inositol (m-Ino) intensities (both contributing positively).

The main contributors to PC 2 were the spectral region between 2.0 ppm and 2.5 ppm (negative), tCho (negative) and m-Ino (positive). PC 3 almost exclusively reflected lactate content.

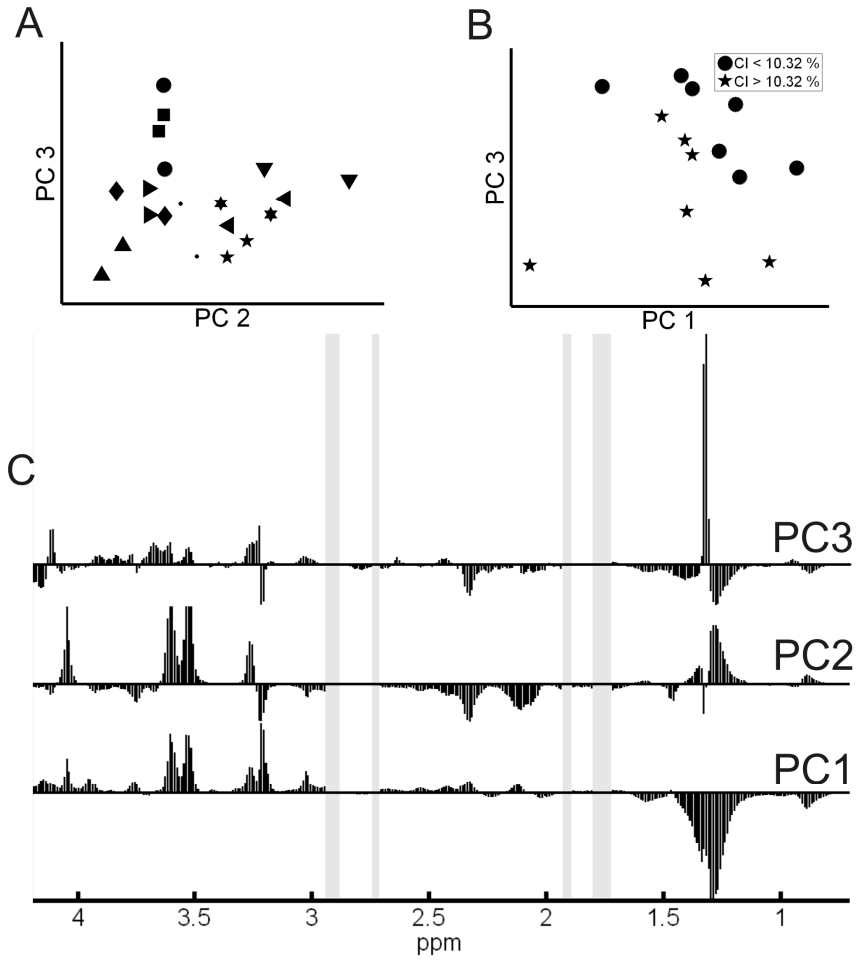

Fig. 5.40 Principal component analysis (PCA) of 20 BTIC NMR spectra. (A) Scores plot (PC3 vs. PC2) broken down to 10 BTIC lines. Each symbol type represents one specific cell line. **(B)** Scores plot (PC3 vs. PC1) broken down to samples with high (stars) and low (circles) clonogenicity, i.e. clonogenic index higher and lower than median. Note that cells with viability lower than 40 % were excluded, i.e. 6 samples. "CI" = clonogenic index. **(C)** Loadings of the first three principal components (PC). Gray haze: Excluded regions dominated by DSS and impurities (acetate and DMSO). Bucket width 0.01 ppm, normalized to total intensity between 0.7 ppm – 4.2 ppm.

5.4.2. Correlation Analyses to Clonogenicity, CD133 and Cell Death

Two approaches were followed to analyze possible correlations between NMR-spectral features and biological assay outcomes: First, calculating Pearson's correlation coefficients between the biological values and the NMR-spectral intensities at every single frequency datapoint. In Fig. 5.41 these frequency-resolved correlation coefficients are plotted together with the individual NMR spectra of each sample. Regarding cell death, highest positive correlations were found at chemical shift values dominated by mobile lipid resonances, e.g. ML1, ML2, ML3, ML5 and ML6. In the case of clonogenic index, major positive correlations were located at frequencies of alanine (ala) and between 2.1 ppm and 2.4 ppm, whereas a major negative correlation region coincided with the m-Ino-dominated interval. The most

striking correlation coefficients to CD133 were determined around 1.0 ppm and 1.4 ppm. However, the only two samples with a CD133-positive fraction higher than 23 %, BTIC lines R40 and R54 in the first measurement series, were extreme outliers both with respect to their high percentage of CD133-positive cells (44.0 % and 45.7 % compared to an average of 4.6 % for the other 18 samples) and regarding their NMR-spectral macromolecular lineshapes, which resembled the findings of an occasional frequency shift of the NMR-visible macromolecule resonances during sedimentation presented in detail in section 5.1.2. Especially in case of the sample R54 of the first series, additional broad shoulders at the left side of mobile lipid peaks, e.g. ML1 and ML2, could be detected (brown arrows in Fig. 5.41). Omitting these two NMR spectra eliminated the major positive correlations to CD133, e.g. at 1.0 ppm and 1.4 ppm, leaving glutathione as the dominant positive contributor to CD133 correlations (data not shown).

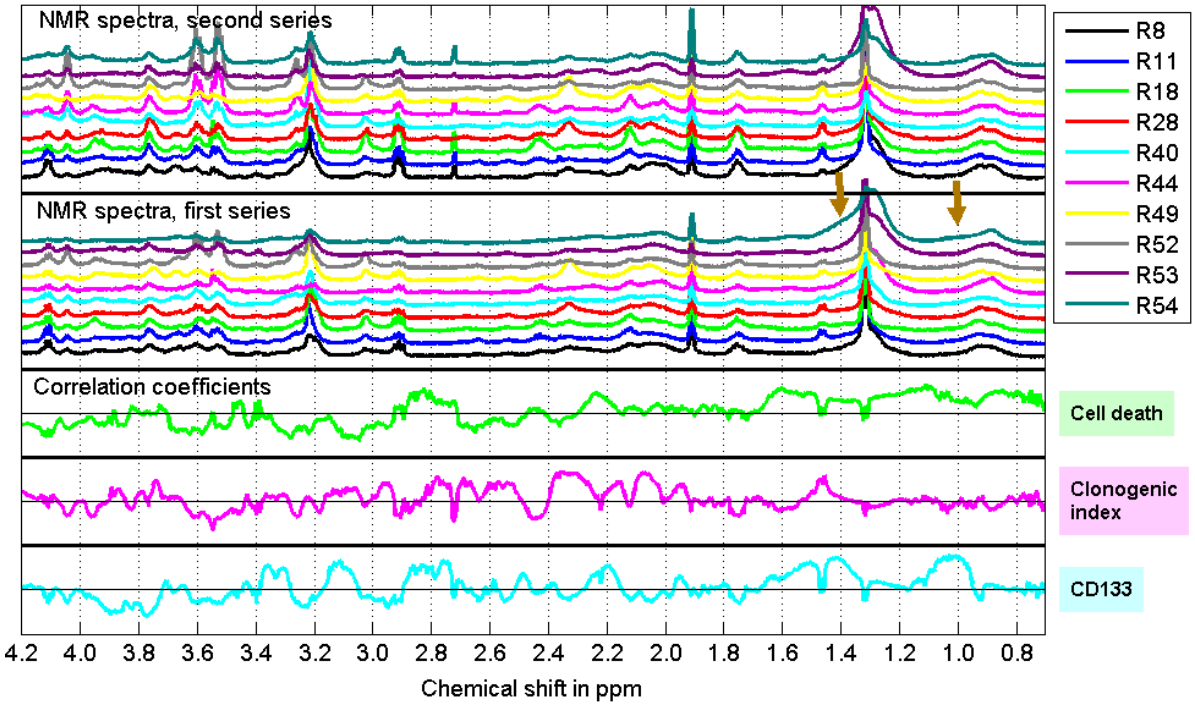

Fig. 5.41 Frequency-resolved correlation coefficients between NMR-spectral intensities and biological data. (Top) NMR spectra of ten different BTIC lines (color-coded, N = 2), normalized to total intensity between 0.7 ppm and 4.2 ppm. 3 - 5 million cells in 550 µl PBS containing 40 µM DSS and 10 % D_2O resuspended in 5 mm Shigemi tube. Acquisition time 5 min, repetition time 4.75 s, T = 5° C, spectrometer frequency 600 MHz or 800 MHz, water suppression: excitation sculpting plus presaturation. Brown arrows mark suspected mobile lipid resonances possibly frequency-shifted during sedimentation. **(Bottom)** Pearson's correlation coefficients of percentage of dead cells, clonogenic index and percentage of CD133-positive cells to NMR-spectral intensities. R = 0 is marked by the thin black line of each correlation curve. Two vertical units correspond to -1 < R < +1.

The second approach to analyze possible correlations between NMR spectra and biological assay outcomes consisted of a manual definition of spectral regions-of-interest (ROI) which showed high variabilities among the measurement series (Fig. 5.42) and subsequently calculating Pearson's correlation coefficients between the integrated intensities of the ROI and biological data. 14 ROI were defined, whose spectral intervals, dominantly contributing molecules and correlation coefficients (R) as well as statistically tested p-values are tabulated in Tab. 5.3. However, only the correlation between the spectral region 2.38 ppm – 2.28 ppm and clonogenicity remained significant after a Bonferroni correction for multiple testing at a significance level $p < 0.05$.

In conclusion of the results of statistical analysis of NMR-signatures and biological data, principal component analysis revealed a relative similarity between NMR spectra of the same BTIC line, but failed to uncover NMR-spectral patterns that would allow discrimination between samples with high and low values of clonogenic index, CD133 and cell death, respectively. Only in one scores plot a moderate clustering of samples according to their clonogenic index was detectable. Frequency-resolved correlation analysis yielded some connections between spectral regions and biological data, but also demonstrated problems when dealing with a small sample cohort with unbalanced properties (especially regarding CD133 data) and NMR-spectral lineshape heterogeneities (e.g. sedimentation problems). Analyzing manually defined regions-of-interest (ROI) that showed high variabilities between the samples, resulted in a couple of significant correlations between those ROI and biological assay outcomes, but only one correlation that was significant after Bonferoni correction, i.e. the connection between the spectral region dominated by glutamate, mobile protein M6 and mobile lipid ML5 resonances (2.28 ppm – 2.38 ppm) and clonogenicity.

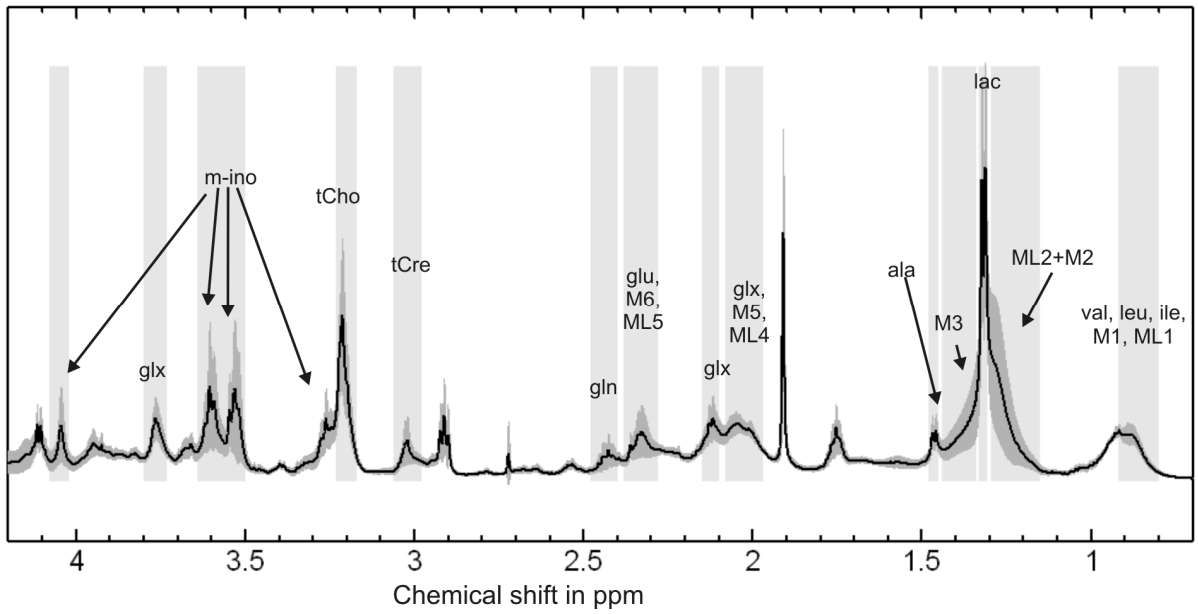

Fig. 5.42 Variations in NMR spectra of BTIC suspensions. Statistical mean (solid black line) and standard deviation (dark grey) of 20 BTIC spectra (20 samples, 2 x 10 different BTIC lines). Bright grey haze: Regions-of-interest (ROI) with high variation. Assignments: Predominant compounds within respective ROI. Spectra scaled to total intensity between 0.7 ppm – 4.2 ppm prior to averaging. 3 - 5 million cells in 500 µl PBS containing 40 µM DSS and 10 % D_2O resuspended in 5 mm Shigemi tube. Acquisition time 5 min, repetition time 4.75 s, T = 5° C, spectrometer frequency 600 MHz or 800 MHz, water suppression: excitation sculpting plus presaturation.

ROI limits in ppm	Contributing molecules	R- and p-values to clonogenic index	R- and p-values to CD133	R-and p-values to cell death
0.80 – 0.92	ML1, M1	n.s.	n.s.	R = 0.52, p = 0.019
1.15 – 1.295	ML2, M2	n.s.	n.s.	R = 0.43, p = 0.059
1.305 – 1.33	lac	n.s.	n.s.	n.s.
1.34 – 1.44	M3, ML2	n.s.	R = 0.55, p = 0.012	n.s.
1.45 – 1.48	ala	R = 0.53, p = 0.015	n.s.	n.s.
1.97 – 2.08	glx, M5, ML4	R = 0.51, p = 0.023	n.s.	n.s.
2.10 – 2.15	glx	n.s.	n.s.	n.s.
2.28 – 2.38	glu, M6, ML5	**R = 0.65, p = 0.002**	n.s.	n.s.
2.40 – 2.48	gln	n.s.	n.s.	n.s.
2.98 – 3.06	tCre	n.s.	n.s.	n.s.
3.17 – 3.23	tCho	n.s.	n.s.	n.s.
3.50 – 3.64	m-Ino	n.s.	n.s.	n.s.
3.73 – 3.80	glx	n.s.	R = -0.54, p = 0.014	n.s.
4.02 – 4.08	m-Ino	n.s.	n.s.	n.s.

Tab. 5.3 Pearson's correlation coefficients between NMR-spectral ROI and biological assay outcomes. Abbreviations of contributing molecules according to **Tab. 5.1**. R-values = correlation coefficients, p-values = outcomes of statistical t-test, n.s. = correlation not significant, i.e. $p > 0.05$. (Yellow) Significant correlation at level $p < 0.05$ after a Bonferroni correction.

6. Discussion

In the following chapter the results presented in chapter 5 are discussed regarding their informational content and compared to findings published by other groups. The first section of this chapter deals with methodological problems of NMR spectroscopy of cell suspensions, followed by approaches to illuminate the nature of NMR-spectral features typical for NMR spectra of cell suspensions. In the second section the findings about mobile lipids in Neural Progenitor Cells (NPC) and Brain Tumor-Initiating Cells (BTIC) are discussed. Mobile lipids are also focused on in the third section, however here, their appearance in macrophages upon loading with low-density lipoproteins (LDL) is reviewed. Finally, the outcomes of statistical analyses are discussed in terms of possible identification of new biomarkers for stemness.

6.1. On the NMR-Visibility of Intracellular Metabolites and Macromolecules in NMR Spectra of Cell Suspensions

In contrast to NMR spectroscopy of dissolved molecules, e.g. from cell culture supernatants or cell lysates, the question of the NMR-visibility of molecules in NMR spectra of suspensions of whole cells is far more fundamental and complex. As already pointed out in chapter 3.1, the interior of cells is by no means a dilute, homogeneous and isotropic environment that would allow molecules to tumble freely and diffuse in an unhindered way [Luby-Phelps 2000]. Additionally, in cell suspensions the extracellular space, i.e. the supernatant, constitutes a major if not even predominant part, whose ingredients also contribute to the NMR spectrum [Duarte et al. 2009]. Moreover, different cellular compartments as well as the whole cell compared to the supernatant might have different magnetic properties, i.e. magnetic susceptibilities [Azanza et al. 1993; Jin 2010; B. E. Kashevskii et al. 2006; Philp et al. 2004; Kuchel & Bulliman 1989]. A heterogeneous distribution of magnetic susceptibilities in turn has an effect on the magnetic field probed by NMR spectroscopy (see section 3.1.2), which further complicates the interpretation of NMR spectra of cell suspensions.

Nevertheless, a variety of NMR signals could be assigned to molecules, both based on the comparison of chemical shifts, lineshapes, multiplet structures to values from databases [Ulrich et al. 2008; Wishart et al. 2009] and published data on cell suspension NMR spectroscopy regarding mobile lipids [Al-Saffar et al. 2002; Barba et al. 1999; Cooper et al. 2001; Delikatny, Lander et al. 1996; Di Vito et al. 2001; Ferretti et al. 1999; Grande et al. 2006; Guidoni et al. 1987; Iorio et al. 2003; Luciani et al. 2009; Quintero et al. 2007; Rémy et al. 1997; Rosi et al. 1999] and mobile proteins[Behar et al. 1994; Behar & Ogino 1991; Behar & Ogino 1993; Kauppinen et al. 1992; Kauppinen et al. 1992; Kauppinen et al. 1993], and by identification of intramolecular magnetization transfers (TOCSY cross peaks). How the NMR-visibility of these assigned signals as well as the ability to discriminate between them and to quantify them depends on the sample preparation, cell density, temperature, relaxation- and diffusion weighting. These aspects are discussed in the following sections.

6.1.1. Dependence on Sample Preparation Methodology

NMR spectroscopy of cell suspensions requires a sophisticated sample preparation method simply because few minutes after resuspending cells in a standard NMR, virtually all cells would have sedimented to the bottom of the tube, i.e. out of the sensitive coil volume, and thus would not contribute to an NMR signal. Unfortunately, both filling a standard NMR tube with an cell pellet size of 500 µl, which would be needed in a 5 mm tube, or acquiring data with a sufficient signal-to-noise ratio during the short time frame before sedimentation [Manganas et al. 2007], was virtually not possible. The reason is the small number of cells which is gained from stem cell culture (3 – 10 million cells per sample). Therefore, the cell numbers per sample were at least one order of magnitude lower than published cell numbers [Al-Saffar et al. 2002; Delikatny, Lander et al. 1996].

Two approaches were followed to circumvent this obstacle. First, embedding the cells in ultralow gelling-point agarose, and second, utilizing susceptibility-matched NMR-tubes (Shigemi) that allowed the positioning of the solid glass bottom of the tube near or even within the sensitive coil volume. In the latter case, the cells could sediment within the coil volume.

In both cases, typical features of NMR spectra of whole cells could be observed, namely sharp singlets and multiplets of metabolites (e.g. lactate, alanine, typically 2-5 Hz linewidth) and of impurities (e.g. isopropanol) as well as broad peaks (ca. 30-100 Hz) of NMR-visible macromolecules, i.e. mobile lipids and/or mobile proteins. Only in case of in-house modified Shigemi tubes with inner diameter of 1 – 2 mm, wherein the sedimented cell pellet comprised the whole height of the sensitive coil volume, narrow lineshapes could not be detected at all. Instead, the peaks of e.g. lactate, alanine and of the internal standard DSS were significantly broadened, typically about 20 Hz. Despite the advantage of a high ratio of intracellular to extracellular volume for a dense pellet that fills the height of the coil volume, the additional line broadening discredited this sample preparation method.

Comparing the two remaining methods, namely embedding in agarose and sedimentation within a 5 mm Shigemi tube, the most obvious difference was the presence or absence of intense agarose signals between 3.3 ppm and 4.7 ppm, which masked an information-rich spectral region including peaks of e.g. choline, myo-inositol, glycine and glucose. Attempts to substract NMR spectra of pure agarose in order to recover these metabolites failed because

the spectral pattern of agarose was not stable regarding internal relations of chemical shifts and intensities. Therefore, at first appearance, the Shigemi method seemed advantageous to the agarose method. However, the fact that the formation of a dense pellet broadened the lineshapes in a 1 – 2 mm Shigemi tube suggests that this line broadening mechanism also plays a role within a sedimented pellet in a 5 mm Shigemi tube, but might be masked by the predominant signals of the rather homogeneous supernatant above the sedimented pellet. In addition, the standard automated shimming routine ("topshim") sometimes gave a magnetic B-field difference of 10 Hz – 20 Hz at the site of the small sedimented cell pellet with respect to the rest of the NMR tube that was solely filled with supernatant. Accordingly, an additional shift of all broad signals about this field difference could be observed. However, the frequencies of sharp resonances did not change. Two conclusions can be drawn from this finding: First, inhomogeneous cell distributions can induce field inhomogeneities that lead to non-uniform spectral shifts. In turn, these shifts might cause misinterpretations of the NMR spectra, especially when a deconvolution approach is employed to separate overlapping macromolecular peaks on the basis of Gaussian-Lorentzians at distinct chemical shifts. Second, the fact that sharp peaks did not shift upon a magnetic B-field difference at the site of the cell pellet suggests that protons within the cell pellet did not give rise to sharp peaks. This result fits the results obtained in 1 – 2 mm Shigemi tubes, wherein the whole sensitive coil volume was filled by the cell pellet, and sharp resonances could neither be detected. In other words, there is evidence that the formation of a cell pellet inhibits detection of sharp resonances that originate from within the cell pellet. This finding urges for an investigation of cell density-dependent effects on the linewidth, e.g. susceptibility-induced magnetic B-field distortions, which is addressed in the following section. Moreover, the question arose if, on the one hand, intracellular molecules were detectable at all, and if they could be discriminated from extracellular molecules on the other hand. This will be discussed in section 6.1.3.

6.1.2. Dependence on Cell Density and Susceptibility Differences

As discussed in the previous section, at high cell densities, e.g. in a sedimented cell pellet, sharp resonances could not be observed. Therefore, a link between cell density and the line broadening was assumed. In principle, line broadening effects can be classified in two phenomena, homogeneous and inhomogeneous broadenings, as pointed out in section 3.1.3. The most obvious mechanism for a line broadening due to an increased cell density might be a specific inhomogeneous effect: Magnetic B-field distortions that are induced by heterogeneous magnetic susceptibility distributions (see section 3.1.2).

Cells are inhomogeneous mixtures of substances, e.g. cytoskeleton proteins, lipid membranes, organelles, DNA etc., that partially exhibit different magnetic susceptibilities. For example, water has a susceptibility of -9.0 ppm [Kuchel et al. 2003], but the susceptibility of pure cell membranes (of red blood cells) is -1.4 ppm [Azanza et al. 1993]. Therefore, a match of intracellular and extracellular susceptibility seems rather unlikely. Comparing the rare data from the literature, the magnetic susceptibility of cells, e.g. HeLa (immortalized cervical cancer cell line) cells, ranges from -6.5 ppm [B. E. Kashevskii et al. 2006] to -9.0 ppm [Jin 2010], omitting special cases like deoxygenated red blood cells (ca. -6 ppm, [Kuchel & Bulliman 1989; Jin 2010]) that contain high amounts of paramagnetic deoxyhemoglobin.

Assuming a difference in susceptibility between inside and outside the cells, it is very likely that the magnetic B-field within the cell suspension is inhomogeneous.

For some geometries, analytical solutions of susceptibility-induced B-field distributions were published [Kuchel et al. 2003; Durrant et al. 2003; Kuchel & Bulliman 1989], and it could be shown that in isolated spherical objects, whose surface can be expressed by a polynomial of second degree in cartesian coordinates, e.g. ellipsoids, the magnetic B-field inside those objects is constant [Kuchel et al. 2003]. However, outside these objects, the magnetic B-field is heavily distorted. For a sphere, these distortions are just the same as for a magnetic dipole located at the center of the sphere [J. D. Jackson 1962]. To the author's best knowledge there are no published data on how these dipolar field distortions affect the interior of additional spheres that neighbour the first sphere. An estimation on this effect could allow conclusions on density-dependent B-field distortions and thus on density-dependent line broadenings. Therefore, in this dissertation, a Fourier-based method [J. P. Marques & Bowtell 2005; Salomir et al. 2003; K. M. Koch et al. 2006] was applied to simulate these cell density-dependent effects due to additional dipolar fields. As already noted in section 3.1.2, discrete Fourier-based approaches, e.g. the discrete Fast Fourier Transform (FFT), have one big advantage in case of periodic problems that comes "for free": The discrete algorithm treats images of objects as if they were repeated periodically in all dimensions. Hence, density- or distance-dependent problems can be mimicked by solely varying the volume ratio of the object and the image. At least, this statement is true for a simple cubic lattice-like periodic arrangement of objects.

As an input for the B-field simulation, a three-dimensional image of a sphere with magnetic susceptibility -8.3 ppm placed in medium with susceptibility -9.0 ppm was constructed, and the sphere diameter was varied at constant image size, thus mimicking different distances between the periodic spheres. The outcome of these simulations revealed a remarkable effect: For big distances between the spheres, i.e. at least twice the sphere diameter, the additional line broadening of an initial 3 Hz resonance from within the sphere was negligible. However, at closer packages, the line broading became more and more profound, resulting in linewidths of more than 30 Hz for distances of 1.25 times the sphere diameter and even 100 Hz for a close package with sphere - sphere contact. In other words, a magnetic susceptibility difference of 0.7 ppm would be sufficient to obscure the duplet structure of e.g. the lactate resonance at 1.32 ppm already at a filling factor of 15 % (i.e. the ratio of intracellular to extracellular volume). Since this effect is linear with susceptibility difference, it can also be inferred that for a closed package, i.e. spheres stacked upon each other, the susceptibility difference would have to be even smaller than 0.08 ppm to observe the duplet structure of lactate.

Various additional broadening effects were ignored by this crude estimation. However, some of them are crucial, and hence should also be mentioned: First, if cells are not spheres but spheroids, e.g. ellipsoids, the interior B-field strength of a single cell is indeed constant (*vide supra*), but in contrast to a sphere the interior B-field of a spheroid exhibits an offset that depends on the orientation of the spheroid with respect to the external applied B-field [Kuchel & Bulliman 1989]. Assuming an isotropic distribution of orientations, for both oblate and prolate spheroids with an axis ratio of 1:2, the additional line broadening would be approximately $\Delta\chi/4$, i.e. 140 Hz and 16 Hz for $\Delta\chi$ of 0.7 ppm and 0.08 ppm, respectively, for a throughout presumed 800 MHz spectrometer frequency. Therefore, even in cases of very low cell densities and very low susceptibility differences between the cells and the

surrounding medium, non-spherical cells tilted randomly with respect to the external B-field would impede high resolution NMR spectroscopy. Again, for $\Delta\chi$ = 0.08 ppm and an ellipsoid axis ratio of 1:2, the duplet structure of intracellular lactate should be obscured solely due to the fact that the cells are prolate or oblate and orientated randomly. Additionally, in general "real" cells are shaped irregularly, which might result in a further line broadening.

Second, the cells might be distributed inhomogeneously, e.g. packed in clusters, called "neurospheres" in case of neural progenitor cells and tumor-initiating cells [Lie et al. 2004; D. Beier et al. 2007], which further complicates the estimation of magnetic B-field distortions and resulting line broadenings. Third, each cell might exhibit a different susceptibility, e.g. dependent on its individual iron content [Jin 2010], which can be up to ten times the average value in iron-rich so-called "magnetic" subpopulations of tumor cells [Jin 2010].

Fourth, and this point was also estimated within this dissertation, the intracellular magnetic susceptibility distribution might be inhomogeneous. As already mentioned in 3.1.3, the interior of cells is a crowded mixture of lipid membranes, cytoskeleton proteins, cytosol, organelles, DNA, etc.. In principle, all these different compartments might have different magnetic susceptibilities. For instance, the magnetic susceptibility difference between fatty acids and water is 0.7 ppm [Kuchel et al. 2003]. Applying this susceptibility difference to a crude two-dimensional model of intracellular membrane structures, the Fourier-based simulation showed very severe magnetic B-field distortions and an additional line broadening of almost 180 Hz. Unfortunately, there is virtually no literature on magnetic susceptibilities of subcellular structures, but the influence of cytoplasmic proteins on the magnetic susceptibility can be estimated: Assuming a cytoplasmic protein concentration of 0.25 g/ml [Luby-Phelps 2000], a mass susceptibility of "non-magnetic" proteins of -7.4 ppm ml/g [Cerdonio et al. 1985] and an average protein density of 1.4 g/ml [Fischer et al. 2004], and applying the formula for the susceptibility of a mixture

$$\chi_{mix} = \xi_w \chi_w + \xi_p \chi_p \qquad 6.1$$

with the volume fractions ξ_i and the "pure" susceptibilities χ_i, a cytoplasmic susceptibility of -9.3 ppm is obtained.

Concluding this line of argument, the differences of magnetic susceptibility among the cellular compartments and thus also between intracellular and extracellular space are in the order of magnitude of 10^{-7}. These differences might lead to severe line broadenings in the order of magnitude of 10 Hz - 100 Hz in case of high cell densities, inhomogeneous cell shapes and orientations, and additionally because of the intracellular inhomogeneities. These findings raise doubts whether high resolution NMR spectroscopy within cells is possible at all.

Nevertheless, a method to distinguish between intra- and extracellular contributions to NMR spectra of cell suspensions might faciliate quantification of intracellular metabolites and molecules. Approaches to that aim are discussed in the next section.

6.1.3. Approaches to Discriminate between Intracellular and Extracellular Molecules

As mentioned earlier, NMR spectra of cell suspensions are *per se* mixtures of contributions from intracellular and extracellular molecules. Additionally, in low density suspensions, which are favoured as argued in the last section, the extracellular volume exceeds the intracellular volume several fold. Therefore, a robust identification and quantification of intracellular resonances urges for sophisticated acquisition strategies beyond "native" pulse-acquire NMR spectroscopy.

To estimate the contributions of the extracellular compartment to the NMR spectra of cell suspensions, the pure supernatant was collected and investigated subsequent to NMR spectroscopy of the sedimented cell pellet. In agreement to published findings of another group [Duarte et al. 2009], all sharp resonances (sharp meaning a linewidth smaller than 10 Hz) of the suspension spectra were retained quantitatively in the supernatant spectra. This finding is again in line with the previous indications that cell pellets do not give rise to highly resolved resonances. In contrast, broad signals e.g. of NMR-visible macromolecules were not found in NMR spectra of subsequent supernatants. Therefore, mobile lipids and mobile proteins can be assumed to reside within the cell pellet.

The first approach to disentangle intracellular signals from the predominant extracellular contributions was to use a gadolinium chelate (Gd-DTPA) to selectively attenuate supernatant resonances by its strong paramagnetism. The idea was that Gd-DTPA should not enter the cells, and thus should only affect extracellular molecules by an enhanced T_1-relaxation [Reuben 1971; Weinmann et al. 1984]. Unfortunately, resonances that were not affected by additions of Gd-DTPA could not be identified. On the one hand, all resonances were broadened, on the other hand, all T_2-values were decreased. A possible reason for the non-specificity of these Gd-DTPA effects could be the penetration of Gd-DTPA into the cells. However, this issue could not be clarified yet. Additionally, it is worth noting that ^{1}H-NMR spectroscopy of cell suspensions requires an effective water suppression, and that the profound line broadening of the water resonance due to Gd-DTPA impeded the water suppression dramatically, which led to distorted baselines and signal-to-noise ratios that were decreased by several orders of magnitude. This in turn rendered NMR spectroscopy of cell suspensions with Gd-DTPA virtually impossible, at least for Gd-DTPA concentrations of 2.5 mM or higher.

The second approach to discriminate extra- and intracellular contributions emploited the possibly different diffusion coefficients of cytoplasmic and supernatant molecules. In addition to NMR-visible macromolecular peaks and sharp resonances of small molecules, further broad resonances could be identified with chemical shifts e.g. of alanine and lactate. The diffusion coefficients of the molecules that gave rise to these additional, broader resonances were 2-3 times smaller than those extracted from the overlapping sharp resonances. As mentioned in section 3.1.3, within cells it is likely that the diffusion of metabolites is smaller than in pure solution. Therefore, the finding of two lactate or alanine components with different (apparent) diffusion coefficients would be in agreement with intra- and extracellular lactate or alanine molecules. However, at this stage it could not be proven that the lactate or alanine components with a hindered diffusion were *de facto* intracellular. Another reason for second metabolite components with smaller diffusion

coefficients and additional line broadenings could simply be that within the sedimented cell pellet extracellular molecules were also affected by a hindered diffusion, i.e. the cells as obstacles, and by susceptibility-induced B-field distortions around the cells, respectively. In contrast, for cell suspensions embedded in agarose the last reason does not account, because the cells in agarose are distributed homogeneously without any formation of cell pellets. However, a broad peak at 1.31 ppm (i.e. very close to the lactate duplet frequency) could also be observed in diffusion-weighted NMR spectra of agarose samples.

To the author's best knowledge, there is only one publication about discrimination between extracellular and intracellular signals by diffusion weighting [Van Zijl et al. 1991]. Herein, it could be shown that in cells that were embedded in agarose and perfused with medium (0.77 ml/min), already at diffusion weightings of $7.7 \cdot 10^9\, s/m^2$ (b-value) all extracellular contributions are attenuated below the noise level. In comparison to Van Zijl's finding, the diffusion-weighted NMR spectra presented in this dissertation did not show any sharp resonances at this b-value, again suggesting (but not proving!) that highly resolved resonances did not originate from intracellular molecules.

In conclusion, several results indicated that highly resolved resonances in NMR spectra of cell suspensions originated from extracellular molecules, and that mild diffusion weighting, but not addition of Gd-DTPA, unveiled second, linebroadened metabolite signals that most probably stemmed from the cell interior.

6.1.4. Estimation of a Detection Limit for Intracellular Metabolites

The results discussed in the previous sections 6.1.1 - 6.1.3 raise the question if NMR spectroscopy of cell suspensions is capable of detecting intracellular small metabolites at all. Unfortunately, two cell density-dependent obstacles cannot be avoided simultaneously: First, line broadening due to magnetic B-field distortions at high cell concentrations, and second, at low cell densities, small signal intensities of intracellular molecules vs. predominant extracellular signals. The signal-to-noise ratio (SNR), which is crucial for detectability, is proportional to the concentration. However, the SNR is also inversely proportional to the linewidth. Therefore, the relative SNR can be estimated by deviding the relative concentration by the line broadening factor. For instance, assuming a linewidth of 3 Hz for a molecule in solution. If the same molecule was inside cells, whose volumes solely constituted 10 % of the sample volume, and if the line broadening inside these cells resulted in a 12 Hz linewidth (i.e. line broadening factor 4), then the relative SNR would be $10\%/4 = 2.5\%$.

The simulations of the magnetic B-field distortions resulted in a maximum SNR for a sphere concentration of 6.5 % - 8.5 % (volume ratios between intracellular and extracellular space). At this maximum, the relative SNR of intracellular molecules was below 4 %, and the linewidth was 5 Hz – 7 Hz for a susceptibility difference of 0.7 ppm at 800 MHz reference frequency. Notably, for this sphere concentration, the relative SNR of extracellular molecules was ten times smaller than that of intracellular molecules. Assuming a lower detection limit of 10 µM in pure solution, according to this estimation, molecules with an intracellular concentration above 0.25 mM could be detected.

However, as already discussed in section 6.1.2, cells are neither homogeneous nor perfect spheres. Randomly orientated oblate or prolate ellipsoids (axis ratio 1:2) instead of spheres would result in an additional linewidth of 140 Hz [Kuchel & Bulliman 1989]. Therefore, the relative SNR would be below 0.2 % instead of 4 %. This in turn would require intracellular concentrations above 5 mM. In section 6.1.2, the effect of intracellular heterogeneities was estimated to give an additional line broadening in the order of 100 Hz. Therefore, a lower detection limit of 5 mM seems reasonable for heterogeneous subcellular compartments, even in the case of spheric cells.

Additionally, the quantification of metabolite resonances with linewidths above 50 Hz would be virtually impossible, since many metabolite signals are very close in chemical shift to each other. For instance, the relatively uncrowded NMR-spectral region between 0.7 ppm and 1.5 ppm, i.e. 640 Hz width at 800 MHz, contains 14 predominant signals in typical NMR spectra of cell suspensions (see Tab. 5.1 and Fig. 5.1).

In conclusion, the detection limit of intracellular small metabolites, like lactate, is estimated to be in the order of 1 mM. Additionally, even at this concentrations, the detection and discrimination of intracellular molecules require great effort, both regarding sophisticated acquisition and post-processing schemes as well as with respect to the optimum cell density and preparation method.

6.1.5. Approaches to Discriminate between Mobile Lipids and Mobile Proteins

Since NMR-visible macromolecules have never been found in supernatants, they were attributed to the intracellular compartment. Therefore, one focus of this dissertation was on these macromolecular signals. Unfortunately, the two subclasses of NMR-visible macromolecules, mobile lipids and mobile proteins, exhibited strong overlaps in chemical shifts of their most prominent resonances. Especially in cases of NMR spectra in which one macromolecular species dominated the other one, a robust discrimination between mobile lipids and mobile proteins including their quantification was not possible on the basis of post-processing deconvolution strategies. Hence, an acquisition method was sought for to differentiate between mobile lipids and mobile proteins.

Since mobile protein signals are essentially amino acid signals [Kauppinen et al. 1992; Behar & Ogino 1991] at chemical shifts of random coil peptides [Wishart et al. 1995], and mobile lipid signals are mainly fatty acid methyl, methylene, and methine signals [Hakumäki & Kauppinen 2000], a discrimination based on protein- and lipid-specific spectral regions in two-dimensional total correlation spectra (TOCSY) was possible. However, apart from very time-consuming two-dimensional acquisitions, the individual peaks were virtually not quantifyable, since their amplitude was heavily weighted by the efficacy of the magnetization transfer during the TOCSY mixing-time. Nevertheless, TOCSY spectra revealed mobile protein contributions even in extremely mobile lipid-dominated spectra.

Relaxation- and diffusion-weighted experiments revealed slight differences between mobile lipid and mobile protein signals. Mobile protein methyl resonances between 0.7 ppm and 1.5 ppm (i.e. M1 – M3) showed a very fast inversion-recovery, and thus a very short T_1-value of 0.54 s, whereas the T_1-values of mobile lipid resonances ML1 and ML2 were found to be 0.87

s and 0.70 s, respectively. In order to selectively suppress signals of molecules with a T_1-value between 0.7 s and 1.7 s (mobile lipids and lactate, respectively) and to retain mobile protein signals as much as possible, a multiple inversion-recovery scheme was tested. A triple inversion-recovery sequence with numerically optimized interpulse delays was shown to be supposed to attenuate mobile lipids and metabolites to an at least sevenfold extent with respect to mobile proteins. Applying this pulse sequence, a relative attenuation of ML2 to mobile proteins of 3:1 was achieved. The discrepancy between the simulated and the measured relative attenuation was most probably due to the sensitivity of this method to proper T_1-value determinations. For instance, a 5 % increase and decrease in T_1-value of mobile proteins and ML2, respectively, would yield a theoretical attenuation of 3:1, i.e. in accordance to the measured attenuation. In combination with the fact that protons in different chemical groups within the same molecule occasionally exhibited different T_1-values (e.g. T_1 of ML1 and ML2), a robust quantification based on multiple inversion-recovery is virtually impossible.

In contrast, a diffusion-based method to discriminate between mobile lipids and mobile proteins should enable more reliable quantifications, since normally, diffusion coefficients are characteristics of whole molecules. An even greater advantage of diffusion weighting over multiple inversion-recovery is the fact that the diffusion coefficient of mobile lipids appeared to be at least one order of magnitude lower than that of mobile proteins, since even at heaviest diffusion weightings the mobile lipid signals were virtually not attenuated. In contrast, the mobile protein peaks M1 – M3 (diffusion coefficient $(8 \pm 1) \cdot 10^{-6} m^2/s$) were attenuated below the noise level at maximum diffusion weighting. This difference in ability to diffuse enabled robust disentanglement of mobile lipid and mobile protein contributions. However, the subtraction of two differently diffusion-weighted spectra in order to obtain a pure mobile protein spectrum resulted in a 95 % loss of the signal-to-noise ratio compared to a non-weighted pulse-acquire spectrum. In addition, diffusion-weighted signals are also T_1- and T_2^J-weighted intrinsically, since within the diffusion weighting pulse sequence the magnetization is restored in z-direction during the diffusion delay (i.e. T_1-weighted), and even allowed to evolve under J-couplings during the gradient pulses (i.e. T_2^J-weighted). Nevertheless, measured relaxation parameters for each resonance could be used to calculate peak-specific correction factors in order to obtain purely diffusion-weighted quantities.

The nature of NMR-visible macromolecules, especially of mobile proteins, is not clarified yet. However, the percentage of cellular proteins that are NMR-visible may be estimated as follows: The intracellular concentration of proteins is approximately 250 mg/ml [Luby-Phelps 2000]. On the average, about 20 % of amino acids in proteins are either leucine, isoleucine or valine [Lehmann et al. 2000]. Assuming an average mass per amino acid of 120 Da, the concentration of branched-chain amino acids (leu, ile, val) is about 400 mmol/L (= 400 mM). The mobile protein peak M1 consists of resonances of leu, ile and val methyl protons. In case of a typical cell sample (5 mio cells, 20 µm cell diameter, 600 µl agarose), NMR-spectral integration of M1 gives a concentration of NMR-visible branched-chain amino acid (BCAA) residues of approximately 400 µM. Multiplication with the dilution factor (sample volume divided by intracellular volume, ca. 25) results in the intracellular concentration of NMR-visible BCAA residues: 10 mM. Therefore, solely 2.5 % of the intracellular proteins are NMR-visible.

Concluding the discussion on strategies to discriminate between the two subclasses of NMR-visible macromolecules, mobile lipids and mobile proteins could be identified according to their specific TOCSY signatures. In order to obtain disentangled NMR spectra of one macromolecular species, extensive diffusion weighting showed advantages (robustness, quantifyability) over multiple inversion-recovery. However, the percentage of intracellular macromolecules that are NMR-visible is rather low. About 2.5 % of cellular proteins are NMR-visible. Regarding cellular lipids, the NMR-visibility is addressed in section 6.3.

6.1.6. Dependence on Temperature

Without perfusion, NMR spectroscopy of cell suspensions is far away from physiological or cell culture conditions. In typical stem cell cultures [Wachs et al. 2003], cells are seeded at densities of 10'000 cells per ml, they are supplied with medium that contains e.g. glucose and amino acids and that is in equilibrium with a defined gas mixture of oxygen and carbon dioxide. In contrast, for NMR spectroscopy several million cells are resuspended in only 500 µl buffer, not medium, and in addition, they are deprived of oxygen and nutrition supply. Therefore, we decided to conduct all NMR spectroscopic measurements at low temperatures, i.e. 5° C, in order to slow down the metabolism rate of the cells during the experiment. Interestingly, and against intuition, another group showed that a series of cell types could be deprived of medium and oxygen for two hours and at 20° C [Duarte et al. 2009] resulting in only minor decreases in viability (0 % - 35 %).

We compared NMR spectra of identical cell samples at 5° C and at 37° C in time series of 15 hours. At 5° C the NMR spectra remained resonably constant with a remarkable exception of lactate, which showed a linear increase to five times its initial value after 15 h. In contrast, at 37° C the appearance of the NMR spectra changed considerably already within the first hour. Three aspects are worth noting: First, within the first hour at 37° C, mobile lipid signals appeared and increased. Upon switching the temperature to 5° C, the intensity of these lipid resonances decreased again but did not vanish completely. This finding indicates that a temperature-dependent phase transition occurred for at least one species of lipids that could give rise to NMR-visible mobile lipids, and that this phase transition was only partially reversible. Interestingly, the used cell line (GBM-TC HTZ-349) virtually never showed distinct mobile lipid resonances at 5° C. Second, the lactate intensity (together with the mobile lipid intensity) did not show any further significant changes after the rapid increase within the first hour, even in case of glucose addition. This suggests that after a short time the lactate-associated metabolism was slowed down dramatically or even came to a standstill. Third, signals of free amino acids appeared and increased profoundly during this time course. At the end of the experiment, after 16 hours of linear increase, the intensities were about ten times the start intensities. The last two aspects might be interpreted as signs for dying cells, i.e. a missing metabolism of glucose to lactate and an ongoing lysis of proteins to free amino acids, respectively.

Concluding the discussion on the temperature-dependent phenomena, at 5° C NMR spectra remained reasonably stable except for lactate. Therefore, measurements at 5° C are considered reliable despite the fact that unperfused cell suspensions are not physiological. In contrast, at 37° C, evidence of rapidly dying cells that would corrupt NMR-spectroscopic results was found in a hindered lactate metabolism and in progressive proteolysis.

Caution is recommended when comparing findings about mobile lipids that were gained at different temperatures, since indications exist that mobile lipid signals are temperature-dependent [Ferretti et al. 2003].

6.2. Mobile Lipids in Neural Progenitor Cells and Brain Tumor-Initiating Cells

Despite the fact that NMR-visible mobile lipids are a common phenomenon both *in vitro* and *in vivo*, the identity and the biological relevance of mobile lipids has not been clarified completely yet. Also summarized in chapter 3.1.4, most of the publications on mobile lipids link their appearance or increase in intensity to cellular stress, e.g. confluence, cell death, pH, chemotherapy etc.. Corresponding to these findings of other groups, the connection of mobile lipids to cellular stress found in neural progenitor cells (NPC) and brain tumor-initiating cells (BTIC) are discussed in the first part of this section. In the second part, the cell-specific influence of transforming growth factor β (TGF-β) on confluence-induced mobile lipid signals is focused on.

6.2.1. Dependence on Confluence, Cell Death and Induction of Apoptosis

As summarized in Tab. 5.2, NMR-visible lipid resonances could be found in NMR spectra of neural progenitor cells (NPC) and brain tumor-initiating cells (BTIC). Moreover, a general correlation of the mobile lipid intensity to cell death could be shown for these two subclasses of brain-derived stem cells. In case of NPC as well as for mesenchymal stem cells (MSC) and COS7 fibroblasts, an increase of mobile lipid signals upon both confluence and induction of apoptosis was evident. In contrast to published findings of another group [Manganas et al. 2007], a connection of mobile lipids to biological quantities of stemness, e.g. Nestin expression or clonogenicity, could not be confirmed, neither in NPC nor in BTIC [Ramm et al. 2009; Ramm et al. 2011].

However, as a general drawback of using mobile lipids as a readout for cellular stress, both the intensities of mobile lipids and their relative change in intensity upon cellular stress varied profoundly between the cell types. Moreover, mobile lipid contents and response characteristics were not even consistent between different cell lines of the same cell type. To illustrate this, the ratio of the intensity of mobile lipids to the percentage of dead cells was seven times higher in BTIC-line R53 than in line R18.

Nevertheless, using mobile lipid resonances as surrogate markers for cellular stress (see section 3.1.4), at least within a single cell line, seems promising, even though much effort still has to be invested to determine the nature of mobile lipids.

6.2.2. Cell-Specific Modulation by TGF-β

Treatment studies of neural progenitor cells (NPC), brain tumor-initiating cell line R49, and three different glioblastoma-derived tumor cell lines (GBM-TC HTZ-349, HTZ-417, U87) with tranforming growth factor β (TGF-β) revealed a cell line-specific response of confluence-induced mobile lipids. Due to the fact that confluence-induced mobile lipids exhibit great variances in intensity even between samples of the same cell line, many of these TGF-β-induced modulations were statistically not significant. Nevertheless, the mobile lipid response on TGF-β-treatment in GBM-TC HTZ-417 and in BTIC R49 was opposite. In case of HTZ-417, a "differentiated" tumor cell line, the mobile lipid intensity decreased upon TGF-β, whereas in R49, a putative "cancer stem cell" line, TGF-β caused an increase of mobile lipids. Notably, this different behavior of differentiated and tumor-initiating cell lines with respect to mobile lipids was reflected in different alterations of cell cycle distributions upon TGF-β. The percentage of cells in cell cyle S-phase was increased by TGF-β in the differentiated cell line but decreased in the tumor-initiating cell line. In addition, a negative correlation between mobile lipids and S-phase was found for both the differentiated and the tumor-initiating cell line, which was significant for the former. This finding agrees well with published data on growth arrest-induced mobile lipids in C6-glioma cells [Quintero et al. 2007; Barba et al. 1999].

The different mobile lipid response to TGF-β-treatment in the different cell types and cell lines could have at least two reasons: First, as mentioned in section 3.2.3, TGF-β has an opposite effect on normal neural (stem) cells and their pathologic counterparts, i.e. glioblastoma cells. In particular, TGF-β causes growth arrest in NPC, acts neuroprotective on the healthy brain, but promotes proliferation in glioblastomas. To date, a general statement on the TGF-β-effect on glioblastoma-derived cell cultures could not be provided, however, unpublished data suggest a rather inhomogeneous behavior with respect to TGF-β-treatment. Second, mobile lipids do not only occur upon growth arrest but also upon other types of cellular stress. For instance, the neuroprotective effect of TGF-β on NPC could be a reason for decreasing mobile lipids upon TGF-β-treatment, since confluence-induced stress might be reduced. If this effect dominates the growth arrest-induced mobile lipid increase, an overall decrease of mobile lipids upon TGF-β-treatment seems plausible even in NPC.

Therefore, in further studies on TGF-β-induced or –reduced mobile lipids, attention should be paid to comparable cell culture conditions in order not to intermix different NMR-visible effects of TGF-β.

6.3. Mobile Lipids in LDL-Loaded Macrophages

Low density lipoproteins (LDL) change their structure upon enzymatic degradation. In native LDL, there is a fluid, oil-like core of cholesteryl ester, whereas trypsinized and hydrolysed LDL (E-LDL) exhibit a multilamellar liposome-like interior [Chao et al. 1992; Hevonoja et al. 2000].

Therefore it was not surprising that NMR spectra of native LDL showed NMR-visible lipids, whereas E-LDL counterparts did not. Interestingly, when macrophages were loaded with different LDL-species, the opposite was found: There was almost no increase of mobile lipids in NMR spectra of suspensions of macrophages loaded with native LDL, but a several fold increase of mobile lipids in E-LDL-loaded macrophages. This finding is in agreement with the fact that E-LDL-loaded macrophages are filled with cytoplasmic lipid droplets to such a high extent that they are also known as “foam cells” [Grandl et al. 2006; G. Schmitz & Grandl 2009]. In addition, a rearrangement of the lipid structure during E-LDL uptake from a multilamellar design to a more mobile arrangement was also confirmed, since E-LDL loading-induced lipid storages were at least partially NMR-visible. Moreover, the relations among the different NMR-visible fatty-acid moieties changed upon E-LDL loading. Especially the mobile lipid peak M6, which originates from fatty-acid methylene that is surrounded by methine, and thus is specific for polyunsaturated lipids, exhibited a several fold increase upon E-LDL loading. According to this change in saturation degree of NMR-visible lipids, a fivefold relative increase in polyunsaturated cholesterol esters (pufa-CE, normalized to the total amount of CE) could be found by mass spectroscopy of E-LDL-loaded macrophages (unpublished data, personal communication with Dr. Margot Grandl, department of clinical chemistry, chair Prof. Schmitz, Regensburg). Most interestingly, the increase in polyunsaturation was not (!) found in pure E-LDL (also mass-spectroscopic data), which constitutes a further indication that lipids are resynthesized within macrophages, even with respect to their degree of saturation.

In conclusion, the structure-dependent NMR-visibility of lipids could be reproduced for lipoproteins. Moreover, a structural resynthesis of multilamellar lipoproteins to lipid droplets within macrophages could be varified by NMR spectroscopy. Notably, an additional modification of the saturation degree upon phagocytosis of enzymatically degraded lipoproteins could be detected.

6.4. Stem Cell-Specific NMR-Spectroscopic Signatures

A major goal of NMR spectroscopy of stem cells *in vitro* constitutes the identification of possible biomarkers for stem cells. Having identified a stem cell-specific marker, a translation “from bench to bedside” could be possible, which in turn would allow to monitor neurogenesis and tumorigenesis non-invasively. Especially in case of brain-derived stem cells, e.g. neural progenitor cells (NPC) and brain tumor-initiating cells (BTIC), non-invasive surrogate markers for changes in these stem cell pools, e.g. upon neurodegeneration or upon tumor antisense therapy, are strongly sought for – unfortunately without success so far.

Therefore, in a pilot study, ten different BTIC-lines were systematically screened for possible BTIC-specific NMR-spectroscopic features. As correlate for stemness, the clonogenicity and the expression of CD133 were evaluated in parallel. The application of statistical methods, i.e. principal component analysis and frequency-resolved correlation analysis, revealed at least one significant correlation between the hallmark of stemness, i.e. clonogenicity, and an NMR-spectral region, namely between 2.28 ppm and 2.38 ppm. Unfortunately, many NMR-visible molecules give rise to resonances within this spectral region, e.g. glutamate, mobile lipids (ML5) and mobile proteins (M5). Therefore, the determination of the molecules which were linked to clonogenicity was virtually impossible.

Furthermore, a moderate clustering of NMR spectra of tumor-initiating cells according to their clonogenicity was found in the scales plot of the first and the third principal component (PC). However, the clustering was not distinct enough to draw conclusions about molecular origins on the basis of the loadings of PC 1 and PC 3. More convincingly, in all scores plots of the first three PC, reasonably small distances between the sample pairs of each BTIC line could be observed, which suggests that relative metabolic similarities of samples from same cell lines could be detected with NMR spectroscopy and subsequent PCA.

However, caution has to be paid when dealing with such a small cohort study, since multivariate testings tend to yield false-positive results if they are not corrected for multiple testing. Nevertheless, the above mentioned correlation between clonogenicity and the spectral region of glutamate, ML5, and M5 remained significant after a Bonferroni correction.

Methodological problems, like the mentioned cohort size of this pilot study and like the corruption of correlation coefficients by sedimentation-induced frequency shifts, pointed out the limits of this approach. Therefore, conclusions drawn from these findings should be verified by further, more sophisticated investigations.

7. Bibliography

Aigner, L. & Bogdahn, U., 2008. TGF-beta in neural stem cells and in tumors of the central nervous system. *Cell and Tissue Research*, 331(1), 225-241.

Al-Saffar, N.M.S., Titley, J.C., Robertson, D., Clarke, P.A., Jackson, L.E., Leach, M.O. & Ronen, S.M., 2002. Apoptosis is associated with triacylglycerol accumulation in Jurkat T-cells. *British Journal of Cancer*, 86(6), 963-970.

Andrew, E.A., Bradbury, A. & Eades, R.G., 1958. Nuclear Magnetic Resonance Spectra from a Crystal rotated at High Speed. *Nature*, 182(4650), 1659.

Andrew, E.R., Bradbury, A. & Eades, R.G., 1959. Removal of Dipolar Broadening of Nuclear Magnetic Resonance Spectra of Solids by Specimen Rotation. *Nature*, 183(4678), 1802-1803.

Araníbar, N., Ott, K., Roongta, V. & Mueller, L., 2006. Metabolomic analysis using optimized NMR and statistical methods. *Analytical Biochemistry*, 355(1), 62-70.

Arslan, F., Bosserhoff, A., Nickl-Jockschat, T., Doerfelt, A., Bogdahn, U. & Hau, P., 2007. The role of versican isoforms V0/V1 in glioma migration mediated by transforming growth factor-β2. *British Journal of Cancer*, 96(10), 1560-1568.

Azanza, M.J., Blott, B.H., del Moral, A. & Peg, M.T., 1993. Measurement of the red blood cell membrane magnetic susceptibility. *Bioelectrochemistry and Bioenergetics*, 30, 43-53.

Barba, I., Cabañas, M.E. & Arús, C., 1999. The relationship between nuclear magnetic resonance-visible lipids, lipid droplets, and cell proliferation in cultured C6 cells. *Cancer Research*, 59(8), 1861-1868.

Barba, I., Mann, P., Cabañas, M.E., Arús, C. & Gasparovic, C., 2001. Mobile lipid production after confluence and pH stress in perfused C6 cells. *NMR in Biomedicine*, 14(1), 33-40.

Baumstark, M.W., Kreutz, W., Berg, A., Frey, I. & Keul, J., 1990. Structure of human low-density lipoprotein subfractions determined by X-ray small-angle scattering. *Biochimica et Biophysica Acta (BBA) - Protein Structure and Molecular Enzymology*, 1037(1), 48-57.

Beckonert, O., Keun, H.C., Ebbels, T.M.D., Bundy, J., Holmes, E., Lindon, J.C. & Nicholson, J.K., 2007. Metabolic profiling, metabolomic and metabonomic procedures for NMR spectroscopy of urine, plasma, serum and tissue extracts. *Nat. Protocols*, 2(11), 2692-2703.

Behar, K.L. & Ogino, T., 1991. Assignment of resonance in the 1H spectrum of rat brain by two-dimensional shift correlated and J-resolved NMR spectroscopy. *Magnetic Resonance in Medicine*, 17(2), 285-303.

Behar, K.L. & Ogino, T., 1993. Characterization of macromolecule resonances in the 1H NMR spectrum of rat brain. *Magnetic Resonance in Medicine*, 30(1), 38-44.

Behar, K.L., Rothman, D.L., Spencer, D.D. & Petroff, O.A., 1994. Analysis of macromolecule resonances in 1H NMR spectra of human brain. *Magnetic Resonance in Medicine*, 32(3), 294-302.

Beier, C.P. & Beier, D., 2011. CD133 negative cancer stem cells in glioblastoma. *Frontiers in Bioscience (Elite Edition)*, 3, 701-710.

Beier, D., Hau, P., Proescholdt, M., Lohmeier, A., Wischhusen, J., Oefner, P.J., Aigner, L., Brawanski, A., Bogdahn, U. & Beier, C.P., 2007. CD133+ and CD133− Glioblastoma-Derived Cancer Stem Cells Show Differential Growth Characteristics and Molecular Profiles. *Cancer Research*, 67(9), 4010 -4015.

Blankenberg, F.G., Katsikis, P.D., Storrs, R.W., Beaulieu, C., Spielman, D., Chen, J.Y., Naumovski, L. & Tait, J.F., 1997. Quantitative analysis of apoptotic cell death using proton nuclear magnetic resonance spectroscopy. *Blood*, 89(10), 3778-3786.

Blankenberg, F.G., Storrs, R.W., Naumovski, L., Goralski, T. & Spielman, D., 1996. Detection of apoptotic cell death by proton nuclear magnetic resonance spectroscopy. *Blood*, 87(5), 1951-1956.

Bloembergen, N., Purcell, E.M. & Pound, R.V., 1948. Relaxation Effects in Nuclear Magnetic Resonance Absorption. *Physical Review*, 73(7), 679.

Bogdahn, U., Apfel, R., Hahn, M., Gerlach, M., Behl, C., Hoppe, J. & Martin, R., 1989. Autocrine tumor cell growth-inhibiting activities from human malignant melanoma. *Cancer Research*, 49(19), 5358-5363.

Brand, A., Richter-Landsberg, C., Flögel, U., Willker, W. & Leibfritz, D., 1998. Rat brain primary neurons immobilized in basement membrane gel threads: an improved method for on-line 13C NMR spectroscopy of live cells. *Brain Research. Brain Research Protocols*, 3(2), 183-191.

Brisdelli, F., Iorio, E., Knijn, A., Ferretti, A., Marcheggiani, D., Lenti, L., Strom, R., Podo, F. & Bozzi, A., 2003. Two-step formation of 1H NMR visible mobile lipids during apoptosis of paclitaxel-treated K562 cells. *Biochemical Pharmacology*, 65(8), 1271-1280.

Callies, R., Sri-Pathmanathan, R.M., Ferguson, D.Y. & Brindle, K.M., 1993. The appearance of neutral lipid signals in the 1H NMR spectra of a myeloma cell line correlates with the induced formation of cytoplasmic lipid droplets. *Magnetic Resonance in Medicine*, 29(4), 546-550.

Cerdonio, M., Morante, S., Torresani, D., Vitale, S., DeYoung, A. & Noble, R.W., 1985. Reexamination of the evidence for paramagnetism in oxy- and carbonmonoxyhemoglobins. *Proceedings of the National Academy of Sciences of the United States of America*, 82(1), 102-103.

Chao, F.F., Blanchette-Mackie, E.J., Tertov, V.V., Skarlatos, S.I., Chen, Y.J. & Kruth, H.S., 1992. Hydrolysis of cholesteryl ester in low density lipoprotein converts this lipoprotein to a liposome. *The Journal of Biological Chemistry*, 267(7), 4992-4998.

Cooper, W.A., Bartier, W.A., Rideout, D.C. & Delikatny, E.J., 2001. 1H NMR visible lipids are induced by phosphonium salts and 5-fluorouracil in human breast cancer cells. *Magnetic Resonance in Medicine*, 45(6), 1001-1010.

Couillard-Despres, S., Uyanik, G., Ploetz, S., Karl, C., Koch, H., Winkler, J. & Aigner, L., 2004. Mitotic impairment by doublecortin is diminished by doublecortin mutations found in patients. *Neurogenetics*, 5(2), 83-93.

Delikatny, E.J., Cooper, W.A., Brammah, S., Sathasivam, N. & Rideout, D.C., 2002. Nuclear magnetic resonance-visible lipids induced by cationic lipophilic chemotherapeutic agents are accompanied by increased lipid droplet formation and damaged mitochondria. *Cancer Research*, 62(5), 1394-1400.

Delikatny, E.J., Lander, C.M., Jeitner, T.M., Hancock, R. & Mountford, C.E., 1996. Modulation of MR-visible mobile lipid levels by cell culture conditions and correlations with chemotactic response. *International Journal of Cancer. Journal International Du Cancer*, 65(2), 238-245.

Delikatny, E.J., Roman, S.K., Hancock, R., Jeitner, T.M., Lander, C.M., Rideout, D.C. & Mountford, C.E., 1996. Tetraphenylphosphonium chloride induced MR-visible lipid accumulation in a malignant human breast cell line. *International Journal of Cancer. Journal International Du Cancer*, 67(1), 72-79.

Di Vito, M., Lenti, L., Knijn, A., Iorio, E., D'Agostino, F., Molinari, A., Calcabrini, A., Stringaro, A., Meschini, S., Arancia, G., Bozzi, A., Strom, R. & Podo, F., 2001. 1H NMR-visible mobile lipid domains correlate with cytoplasmic lipid bodies in apoptotic T-lymphoblastoid cells. *Biochimica Et Biophysica Acta*, 1530(1), 47-66.

Dickinson, W.C., 1951. The Time Average Magnetic Field at the Nucleus in Nuclear Magnetic Resonance Experiments. *Physical Review*, 81(5), 717.

Dong, Z., Dreher, W., Leibfritz, D. & Peterson, B.S., 2009. Challenges of using MR spectroscopy to detect neural progenitor cells in vivo. *AJNR. American Journal of Neuroradiology*, 30(6), 1096-1101.

Duarte, I.F., Marques, J., Ladeirinha, A.F., Rocha, C., Lamego, I., Calheiros, R., Silva, T.M., Marques, M.P.M., Melo, J.B., Carreira, I.M. & Gil, A.M., 2009. Analytical approaches toward successful human cell metabolome studies by NMR spectroscopy. *Analytical Chemistry*, 81(12), 5023-5032.

Duer, M., 2002. *solid-state NMR spectroscopy*, Wiley-Blackwell.

Durrant, C.J., Hertzberg, M.P. & Kuchel, P.W., 2003. Magnetic susceptibility: Further insights into macroscopic and microscopic fields and the sphere of Lorentz. *Concepts in Magnetic Resonance*, 18A(1), 72-95.

Erdelyi, A., 1954. *Tables of integral transforms. Based, in part, on notes left by Harry Bateman,*, New York: McGraw-Hill.

Ferretti, A., Knijn, A., Iorio, E., Pulciani, S., Giambenedetti, M., Molinari, A., Meschini, S., Stringaro, A., Calcabrini, A., Freitas, I., Strom, R., Arancia, G. & Podo, F., 1999. Biophysical and structural characterization of 1H-NMR-detectable mobile lipid domains in NIH-3T3 fibroblasts. *Biochimica Et Biophysica Acta*, 1438(3), 329-348.

Ferretti, A., Knijn, A., Raggi, C. & Sargiacomo, M., 2003. High-resolution proton NMR measures mobile lipids associated with Triton-resistant membrane domains in haematopoietic K562 cells lacking or expressing caveolin-1. *European Biophysics Journal: EBJ*, 32(2), 83-95.

Fischer, H., Polikarpov, I. & Craievich, A.F., 2004. Average protein density is a molecular-weight-dependent function. *Protein Science : A Publication of the Protein Society*, 13(10), 2825-2828.

Folch, J., LEES, M. & SLOANE STANLEY, G.H., 1957. A simple method for the isolation and purification of total lipides from animal tissues. *The Journal of Biological Chemistry*, 226(1), 497-509.

Friedman, S.D., 2008. Comment on "Magnetic resonance spectroscopy identifies neural progenitor cells in the live human brain". *Science (New York, N.Y.)*, 321(5889), 640; author reply 640.

Goodsell, D.S., 2009. *The machinery of life*, Springer.

de Graaf, R.A., 2007. *in vivo NMR Spectroscopy, Principles and Techniques*, John Wiley & Sons.

de Graaf, R.A., Brown, P.B., McIntyre, S., Nixon, T.W., Behar, K.L. & Rothman, D.L., 2006. High magnetic field water and metabolite proton T1 and T2 relaxation in rat brain in vivo. *Magnetic Resonance in Medicine*, 56(2), 386-394.

Grande, S., Giovannini, C., Luciani, A.M., Palma, A., Rosi, A., Sapora, O., Viti, V. & Guidoni, L., 2006. Radiation effects in cultured tumour cells examined by 1H MRS: mobile lipids modulation and proliferative arrest. *Radiation Protection Dosimetry*, 122(1-4), 202-204.

Grande, S., Luciani, A.M., Rosi, A., Cherubini, R., Conzato, M., Guidoni, L. & Viti, V., 2001. Radiation effects on soluble metabolites in cultured HeLa cells examined by 1H MRS: changes in concentration of glutathione and of lipid catabolites induced by gamma rays and proton beams. *International Journal of Cancer. Journal International Du Cancer*, 96 Suppl, 27-42.

Grandl, M., Bared, S.M., Liebisch, G., Werner, T., Barlage, S. & Schmitz, G., 2006. E-LDL and Ox-LDL differentially regulate ceramide and cholesterol raft microdomains in human Macrophages. *Cytometry Part A*, 69A(3), 189-191.

Griffin, J.L., Bollard, M., Nicholson, J.K. & Bhakoo, K., 2002. Spectral profiles of cultured neuronal and glial cells derived from HRMAS 1H NMR spectroscopy. *NMR in Biomedicine*, 15(6), 375-384.

Guidoni, L., Mariutti, G., Rampelli, G.M., Rosi, A. & Viti, V., 1987. Mobile phospholipid signals in NMR spectra of cultured human adenocarcinoma cells. *Magnetic Resonance in Medicine*, 5(6), 578-585.

Hakumäki, J.M. & Kauppinen, R.A., 2000. 1H NMR visible lipids in the life and death of cells. *Trends in Biochemical Sciences*, 25(8), 357-362.

Hevonoja, T., Pentikäinen, M.C., Hyvönen, M.T., Kovanen, P.T. & Ala-Korpela, M., 2000. Structure of low density lipoprotein (LDL) particles: Basis for understanding molecular changes in modified LDL. *Biochimica et Biophysica Acta (BBA) - Molecular and Cell Biology of Lipids*, 1488(3), 189-210.

Hoch, J.C., Maciejewski, M.W. & Gryk, M.R., 2008. Comment on "magnetic resonance spectroscopy identifies neural progenitor cells in the live human brain". *Science (New York, N.Y.)*, 321(5889), 640; author reply 640.

Hwang, T.L. & Shaka, A.J., 1995. Water Suppression That Works. Excitation Sculpting Using Arbitrary Wave-Forms and Pulsed-Field Gradients. *Journal of Magnetic Resonance, Series A*, 112(2), 275-279.

Iorio, E., Di Vito, M., Spadaro, F., Ramoni, C., Lococo, E., Carnevale, R., Lenti, L., Strom, R. & Podo, F., 2003. Triacsin C inhibits the formation of 1H NMR-visible mobile lipids and lipid bodies in HuT 78 apoptotic cells. *Biochimica Et Biophysica Acta*, 1634(1-2), 1-14.

Jackson, J.D., 1962. *Classical electrodynamics*, Wiley.

Jansen, J.F.A., Gearhart, J.D. & Bulte, J.W.M., 2008. Comment on "Magnetic resonance spectroscopy identifies neural progenitor cells in the live human brain". *Science (New York, N.Y.)*, 321(5889), 640;author reply 640.

Jansen, J.F.A., Shamblott, M.J., van Zijl, P.C.M., Lehtimäki, K.K., Bulte, J.W.M., Gearhart, J.D. & Hakumäki, J.M., 2006. Stem cell profiling by nuclear magnetic resonance spectroscopy. *Magnetic Resonance in Medicine*, 56(3), 666-670.

Jin, X., 2010. *Investigation of Intrinsic Cell Magnetophoresis for Label-Less Cell Separation and Analysis and the Optimization of the CTV Instrumentation for Such Studies*. thesis. Available at: http://etd.ohiolink.edu/view.cgi/Jin%20Xiaoxia.pdf?osu1268002273 [Accessed February 18, 2011].

Kapinsky, M., Torzewski, M., Buchler, C., Duong, C.Q., Rothe, G. & Schmitz, G., 2001. Enzymatically Degraded LDL Preferentially Binds to CD14high CD16+ Monocytes and Induces Foam Cell Formation Mediated Only in Part by the Class B Scavenger-Receptor CD36. *Arterioscler Thromb Vasc Biol*, 21(6), 1004-1010.

Karl, C., Couillard-Despres, S., Prang, P., Munding, M., Kilb, W., Brigadski, T., Plötz, S., Mages, W., Luhmann, H., Winkler, J., Bogdahn, U. & Aigner, L., 2005. Neuronal precursor-specific activity of a human doublecortin regulatory sequence. *Journal of Neurochemistry*, 92(2), 264-282.

Kashevskii, B.E., Kashevskii, S.B., Prokhorov, I.V., Aleksandrova, E.N. & Istomin, Y.P., 2006. Magnetophoresis and the magnetic susceptibility of HeLa tumor cells. *Biophysics*, 51(6), 902-907.

Kauppinen, R.A., Kokko, H. & Williams, S.R., 1992. Detection of mobile proteins by proton nuclear magnetic resonance spectroscopy in the guinea pig brain ex vivo and their partial purification. *Journal of Neurochemistry*, 58(3), 967-974.

Kauppinen, R.A., Niskanen, T., Hakumäki, J.M. & Williams, S.R., 1993. Quantitative analysis of 1H NMR detected proteins in the rat cerebral cortex in vivo and in vitro. *NMR in Biomedicine*, 6(4), 242-247.

Kauppinen, R.A., Nissinen, T., Kärkkäinen, A.M., Pirttilä, T.R., Palvimo, J., Kokko, H. & Williams, S.R., 1992. Detection of thymosin beta 4 in situ in a guinea pig cerebral cortex preparation using 1H NMR spectroscopy. *The Journal of Biological Chemistry*, 267(14), 9905-9910.

Kauppinen, R.A. & Palvimo, J., 1992. Contribution of cytoplasmic polypeptides to the 1H NMR spectrum of developing rat cerebral cortex. *Magnetic Resonance in Medicine*, 25(2), 398-407.

Keeler, J., 2005. *Understanding NMR Spectroscopy*, John Wiley & Sons.

King, N.J., Delikatny, E.J. & Holmes, K.T., 1994. 1H magnetic resonance spectroscopy of primary human and murine cells of the myeloid lineage. *ImmunoMethods*, 4(2), 188-198.

Knijn, A., Ferretti, A., Zhang, P.J., Giambenedetti, M., Molinari, A., Meschini, S., Pulciani, S. & Podo, F., 1997. Lower levels of 1H MRS-visible mobile lipids in H-ras transformed tumorigenic fibroblasts with respect to their untransformed parental cells. *Cellular and Molecular Biology (Noisy-Le-Grand, France)*, 43(5), 691-701.

Koch, K.M., Papademetris, X., Rothman, D.L. & de Graaf, R.A., 2006. Rapid calculations of susceptibility-induced magnetostatic field perturbations for in vivo magnetic resonance. *Physics in Medicine and Biology*, 51(24), 6381-6402.

Kuchel, P.W. & Bulliman, B.T., 1989. Perturbation of homogeneous magnetic fields by isolated single and confocal spheroids. Implications for NMR spectroscopy of cells. *NMR in Biomedicine*, 2(4), 151-160.

Kuchel, P.W., Chapman, B.E., Bubb, W.A., Hansen, P.E., Durrant, C.J. & Hertzberg, M.P., 2003. Magnetic susceptibility: Solutions, emulsions, and cells. *Concepts in Magnetic Resonance*, 18A(1), 56-71.

Le Belle, J.E., Harris, N.G., Williams, S.R. & Bhakoo, K.K., 2002. A comparison of cell and tissue extraction techniques using high-resolution 1H-NMR spectroscopy. *NMR in Biomedicine*, 15(1), 37-44.

Le Moyec, L., Kawakami, M., Leray, G., Larue, V., Briane, D., Hantz, E. & De Certaines, J., 2000. Magnetic resonance spectroscopy and fluorescence microscopy to investigate mobile lipids in sensitive, resistant and reverting K562 cells and their membranes. *Anticancer Research*, 20(6B), 4513-4518.

Le Moyec, L., Tatoud, R., Eugène, M., Gauvillé, C., Primot, I., Charlemagne, D. & Calvo, F., 1992. Cell and membrane lipid analysis by proton magnetic resonance spectroscopy in five breast cancer cell lines. *British Journal of Cancer*, 66(4), 623-628.

Lehmann, W.D., Bohne, A. & von Der Lieth, C.W., 2000. The information encrypted in accurate peptide masses-improved protein identification and assistance in glycopeptide identification and characterization. *Journal of Mass Spectrometry: JMS*, 35(11), 1335-1341.

Lehtimäki, K.K., Valonen, P.K., Griffin, J.L., Väisänen, T.H., Gröhn, O.H.J., Kettunen, M.I., Vepsäläinen, J., Ylä-Herttuala, S., Nicholson, J.K. & Kauppinen, R.A., 2003. Metabolite changes in BT4C rat gliomas undergoing ganciclovir-thymidine kinase gene therapy-induced programmed cell death as studied by 1H NMR spectroscopy in vivo, ex vivo, and in vitro. *The Journal of Biological Chemistry*, 278(46), 45915-45923.

Levitt, M.H., 2008. *Spin Dynamics, Basics of Nuclear Magnetic Resonance* 2. ed., John Wiley & Sons.

Lie, D.C., Song, H., Colamarino, S.A., Ming, G. & Gage, F.H., 2004. Neurogenesis in the adult brain: new strategies for central nervous system diseases. *Annual Review of Pharmacology and Toxicology*, 44, 399-421.

Live, D.H. & Chan, S.I., 1970. Bulk susceptibility corrections in nuclear magnetic resonance experiments using superconducting solenoids. *Analytical Chemistry*, 42(7), 791-792.

Lorentz, H.A., 1916. *The theory of electrons and its applications to the phenomena of light and radiant heat.*, Leibzig: Teubner.

Luby-Phelps, K., 2000. Cytoarchitecture and physical properties of cytoplasm: volume, viscosity, diffusion, intracellular surface area. *International Review of Cytology*, 192, 189-221.

Luciani, A.M., Grande, S., Palma, A., Rosi, A., Giovannini, C., Sapora, O., Viti, V. & Guidoni, L., 2009. Characterization of 1H NMR detectable mobile lipids in cells from human adenocarcinomas. *The FEBS Journal*, 276(5), 1333-1346.

Luciani, A.M., Rosi, A., Grande, S., Guidoni, L., Viti, V., Cherubini, R. & Conzato, M., 2002. Changes in soluble metabolites induced in tumour cells by gamma rays and proton beams: a 1H magnetic resonance spectroscopy study. *Radiation Protection Dosimetry*, 99(1-4), 307-310.

Ma, L.H., Li, Y., Djurić, P.M. & Maletić-Savatić, M., 2011. Systems biology approach to imaging of neural stem cells. *Methods in Molecular Biology (Clifton, N.J.)*, 711, 421-434.

Manganas, L.N., Zhang, X., Li, Y., Hazel, R.D., Smith, S.D., Wagshul, M.E., Henn, F., Benveniste, H., Djuric, P.M., Enikolopov, G. & Maletic-Savatic, M., 2007. Magnetic Resonance Spectroscopy Identifies Neural Progenitor Cells in the Live Human Brain. *Science*, 318(5852), 980-985.

Marques, J.P. & Bowtell, R., 2005. Application of a Fourier-based method for rapid calculation of field inhomogeneity due to spatial variation of magnetic susceptibility. *Concepts in Magnetic Resonance Part B: Magnetic Resonance Engineering*, 25B(1), 65-78.

May, G.L., Sztelma, K. & Sorrell, T.C., 1994. The presence of cytoplasmic lipid droplets is not sufficient to account for neutral lipid signals in the 1H MR spectra of neutrophils. *Magnetic Resonance in Medicine*, 31(2), 212-217.

McLean, M.A., Woermann, F.G., Barker, G.J. & Duncan, J.S., 2000. Quantitative analysis of short echo time (1)H-MRSI of cerebral gray and white matter. *Magnetic Resonance in Medicine: Official Journal of the Society of Magnetic Resonance in Medicine / Society of Magnetic Resonance in Medicine*, 44(3), 401-411.

Mikhailenko, V.M., Philchenkov, A.A. & Zavelevich, M.P., 2005. Analysis of 1H NMR-detectable mobile lipid domains for assessment of apoptosis induced by inhibitors of DNA synthesis and replication. *Cell Biology International*, 29(1), 33-39.

Milkevitch, M., Shim, H., Pilatus, U., Pickup, S., Wehrle, J.P., Samid, D., Poptani, H., Glickson, J.D. & Delikatny, E.J., 2005. Increases in NMR-visible lipid and glycerophosphocholine during phenylbutyrate-induced apoptosis in human prostate cancer cells. *Biochimica Et Biophysica Acta*, 1734(1), 1-12.

Mirbahai, L., Wilson, M., Shaw, C.S., McConville, C., Malcomson, R.D.C., Griffin, J.L., Kauppinen, R.A. & Peet, A.C., 2010. (1)H magnetic resonance spectroscopy metabolites as biomarkers for cell cycle arrest and cell death in rat glioma cells. *The International Journal of Biochemistry & Cell Biology*. Available at: http://www.ncbi.nlm.nih.gov/pubmed/20633697 [Accessed February 7, 2011].

Mountford, C.E. & Tattersall, M.H., 1987. Proton magnetic resonance spectroscopy and tumour detection. *Cancer Surveys*, 6(2), 285-314.

Nicholson, C. & Phillips, J.M., 1981. Ion diffusion modified by tortuosity and volume fraction in the extracellular microenvironment of the rat cerebellum. *The Journal of Physiology*, 321(1), 225 -257.

Nicolay, K., Braun, K.P.J., de Graaf, R.A., Dijkhuizen, R.M. & Kruiskamp, M.J., 2001. Diffusion NMR spectroscopy. *NMR in Biomedicine*, 14(2), 94-111.

Opstad, K.S., Bell, B.A., Griffiths, J.R. & Howe, F.A., 2008a. An assessment of the effects of sample ischaemia and spinning time on the metabolic profile of brain tumour biopsy specimens as determined by high-resolution magic angle spinning (1)H NMR. *NMR in Biomedicine*, 21(10), 1138-1147.

Opstad, K.S., Bell, B.A., Griffiths, J.R. & Howe, F.A., 2008b. Toward accurate quantification of metabolites, lipids, and macromolecules in HRMAS spectra of human brain tumor biopsies using LCModel. *Magnetic Resonance in Medicine*, 60(5), 1237-1242.

Pfeuffer, J., Flögel, U., Dreher, W. & Leibfritz, D., 1998. Restricted diffusion and exchange of intracellular water: theoretical modelling and diffusion time dependence of1H NMR measurements on perfused glial cells. *NMR in Biomedicine*, 11(1), 19-31.

Philp, D.J., Bubb, W.A. & Kuchel, P.W., 2004. Chemical shift and magnetic susceptibility contributions to the separation of intracellular and supernatant resonances in variable angle spinning NMR spectra of erythrocyte suspensions. *Magnetic Resonance in Medicine*, 51(3), 441-444.

Prassl, R. & Laggner, P., 2008. Molecular structure of low density lipoprotein: current status and future challenges. *European Biophysics Journal*, 38(2), 145-158.

Quintero, M.R., Cabañas, M.E. & Arús, C., 2010. 13C-labelling studies indicate compartmentalized synthesis of triacylglycerols in C6 rat glioma cells. *Biochimica Et Biophysica Acta*, 1801(7), 693-701.

Quintero, M.R., Cabañas, M.E. & Arús, C., 2007. A possible cellular explanation for the NMR-visible mobile lipid (ML) changes in cultured C6 glioma cells with growth. *Biochimica et Biophysica Acta (BBA) - Molecular and Cell Biology of Lipids*, 1771(1), 31-44.

Ramm, P., Bettscheider, M., Beier, D., Kalbitzer, H.R., Bogdahn, U., Hau, P., Aigner, L. & Beier, C.P., 2011. 1H-NMR Spectroscopy of Glioblastoma Cancer Stem Cells. *Stem Cells and Development*.

Ramm, P., Couillard-Despres, S., Plötz, S., Rivera, F.J., Krampert, M., Lehner, B., Kremer, W., Bogdahn, U., Kalbitzer, H.R. & Aigner, L., 2009. A Nuclear Magnetic Resonance Biomarker for Neural Progenitor Cells: Is It All Neurogenesis? *Stem Cells*, 27(2), 420-423.

Rémy, C., Fouilhé, N., Barba, I., Sam-Laï, E., Lahrech, H., Cucurella, M.G., Izquierdo, M., Moreno, A., Ziegler, A., Massarelli, R., Décorps, M. & Arús, C., 1997. Evidence that mobile lipids detected in rat brain glioma by 1H nuclear magnetic resonance correspond to lipid droplets. *Cancer Research*, 57(3), 407-414.

Reuben, J., 1971. Gadolinium(III) as a paramagnetic probe for proton relaxation studies of biological macromolecules. Binding to bovine serum albumin. *Biochemistry*, 10(15), 2834-2838.

Reya, T., Morrison, S.J., Clarke, M.F. & Weissman, I.L., 2001. Stem cells, cancer, and cancer stem cells. *Nature*, 414(6859), 105-111.

Rivera, F.J., Couillard-Despres, S., Pedre, X., Ploetz, S., Caioni, M., Lois, C., Bogdahn, U. & Aigner, L., 2006. Mesenchymal stem cells instruct oligodendrogenic fate decision on adult neural stem cells. *Stem Cells (Dayton, Ohio)*, 24(10), 2209-2219.

Roman, S.K., Jeitner, T.M., Hancock, R., Cooper, W.A., Rideout, D.C. & Delikatny, E.J., 1997. Induction of magnetic resonance-visible lipid in a transformed human breast cell line by tetraphenylphosphonium chloride. *International Journal of Cancer. Journal International Du Cancer*, 73(4), 570-579.

Rosi, A., Grande, S., Luciani, A.M., Barone, P., Mlynarik, V., Viti, V. & Guidoni, L., 2004. (1H) MRS studies of signals from mobile lipids and from lipid metabolites: comparison of the behavior in cultured tumor cells and in spheroids. *NMR in Biomedicine*, 17(2), 76-91.

Rosi, A., Luciani, A.M., Matarrese, P., Arancia, G., Viti, V. & Guidoni, L., 1999. 1H-MRS lipid signal modulation and morphological and ultrastructural changes related to tumor cell proliferation. *Magnetic Resonance in Medicine: Official Journal of the Society of Magnetic Resonance in Medicine / Society of Magnetic Resonance in Medicine*, 42(2), 248-257.

Salomir, R., de Senneville, B. & Moonen, C.T.W., 2003. A fast calculation method for magnetic field inhomogeneity due to an arbitrary distribution of bulk susceptibility. *Concepts in Magnetic Resonance*, 19B(1), 26-34.

Santini, M.T., Romano, R., Rainaldi, G., Ferrante, A., Motta, A. & Indovina, P.L., 2006. Increases in 1H-NMR mobile lipids are not always associated with overt apoptosis: evidence from MG-63 human osteosarcoma three-dimensional spheroids exposed to a low dose (2 Gy) of ionizing radiation. *Radiation Research*, 165(2), 131-141.

Schmitz, G. & Grandl, M., 2009. Endolysosomal phospholipidosis and cytosolic lipid droplet storage and release in macrophages. *Biochimica et Biophysica Acta (BBA) - Molecular and Cell Biology of Lipids*, 1791(6), 524-539.

Schmitz, J.E., Kettunen, M.I., Hu, D.E. & Brindle, K.M., 2005. 1H MRS-visible lipids accumulate during apoptosis of lymphoma cells in vitro and in vivo. *Magnetic Resonance in Medicine*, 54(1), 43-50.

Stejskal, E.O. & Tanner, J.E., 1965. Spin Diffusion Measurements: Spin Echoes in the Presence of a Time-Dependent Field Gradient. *The Journal of Chemical Physics*, 42(1), 288.

Tanner, J.E. & Stejskal, E.O., 1968. Restricted Self-Diffusion of Protons in Colloidal Systems by the Pulsed-Gradient, Spin-Echo Method. *The Journal of Chemical Physics*, 49(4), 1768.

Ulrich, E.L., Akutsu, H., Doreleijers, J.F., Harano, Y., Ioannidis, Y.E., Lin, J., Livny, M., Mading, S., Maziuk, D., Miller, Z., Nakatani, E., Schulte, C.F., Tolmie, D.E., Kent Wenger, R., Yao, H. & Markley, J.L., 2008. BioMagResBank. *Nucl. Acids Res.*, 36(suppl_1), D402-408.

Urenjak, J., Williams, S.R., Gadian, D.G. & Noble, M., 1993. Proton nuclear magnetic resonance spectroscopy unambiguously identifies different neural cell types. *The Journal of Neuroscience: The Official Journal of the Society for Neuroscience*, 13(3), 981-989.

Van Zijl, P.C., Moonen, C.T., Faustino, P., Pekar, J., Kaplan, O. & Cohen, J.S., 1991. Complete separation of intracellular and extracellular information in NMR spectra of perfused cells by diffusion-weighted spectroscopy. *Proceedings of the National Academy of Sciences of the United States of America*, 88(8), 3228-3232.

Veale, M.F., Roberts, N.J., King, G.F. & King, N.J., 1997. The generation of 1H-NMR-detectable mobile lipid in stimulated lymphocytes: relationship to cellular activation, the cell cycle, and phosphatidylcholine-specific phospholipase C. *Biochemical and Biophysical Research Communications*, 239(3), 868-874.

Vescovi, A.L., Galli, R. & Reynolds, B.A., 2006. Brain tumour stem cells. *Nature Reviews. Cancer*, 6(6), 425-436.

Vollmann-Zwerenz, A., Diermeier-Daucher, S., Wege, A.K., Sassen, A., Schmidt-Brücken, E., Hofstaedter, F., Ortmann, O., Nauwelaers, F. & Brockhoff, G., 2010. Multichromatic phenotyping of HER receptor coexpression in breast tumor tissue samples using flow cytometry-Possibilities and limitations. *Cytometry Part A*, 77A(4), 387-398.

Wachs, F.P., Couillard-Despres, S., Engelhardt, M., Wilhelm, D., Ploetz, S., Vroemen, M., Kaesbauer, J., Uyanik, G., Klucken, J., Karl, C., Tebbing, J., Svendsen, C., Weidner, N., Kuhn, H.G., Winkler, J. & Aigner, L., 2003. High efficacy of clonal growth and expansion of adult neural stem cells. *Laboratory Investigation; a Journal of Technical Methods and Pathology*, 83(7), 949-962.

Weinmann, H.J., Brasch, R.C., Press, W.R. & Wesbey, G.E., 1984. Characteristics of gadolinium-DTPA complex: a potential NMR contrast agent. *AJR. American Journal of Roentgenology*, 142(3), 619-624.

Wishart, D., Bigam, C., Holm, A., Hodges, R. & Sykes, B., 1995. 1H, 13C and 15N random coil NMR chemical shifts of the common amino acids. I. Investigations of nearest-neighbor effects. *Journal of Biomolecular NMR*, 5(1), 67-81.

Wishart, D.S., Knox, C., Guo, A.C., Eisner, R., Young, N., Gautam, B., Hau, D.D., Psychogios, N., Dong, E., Bouatra, S., Mandal, R., Sinelnikov, I., Xia, J., Jia, L., Cruz, J.A., Lim, E., Sobsey, C.A., Shrivastava, S., Huang, P., Liu, P., Fang, L., Peng, J., Fradette, R., Cheng, D., Tzur, D., Clements, M., Lewis, A., De Souza, A., Zuniga, A., Dawe, M., Xiong, Y., Clive, D., Greiner, R., Nazyrova, A., Shaykhutdinov, R., Li, L., Vogel, H.J. & Forsythe, I., 2009. HMDB: a knowledgebase for the human metabolome. *Nucl. Acids Res.*, 37(suppl_1), D603-610.

Wu, D.H., Chen, A.D. & Johnson, C.S., 1995. An Improved Diffusion-Ordered Spectroscopy Experiment Incorporating Bipolar-Gradient Pulses. *Journal of Magnetic Resonance, Series A*, 115(2), 260-264.

Zwingmann, C. & Leibfritz, D., 2003. Regulation of glial metabolism studied by 13C-NMR. *NMR in Biomedicine*, 16(6-7), 370-399.

8. Appendix

8.1. Matlab Code for Simulation of Susceptibility-Induced Magnetic B-Field Distortions

The following Matlab code enables simulations of B-field distributions according to the method described in sections 3.1.2 and 4.3. In the first 14 lines, the user is able to configure the simulation by adjusting the spectrometer frequency, the two different susceptibilities, the pixel size and the relative diameter of the sphere/cube. Alternatively to spheres and cubes, hand-drawn black-and-white png-images can be imported, which are projected along the desired dimension with respect to the magnetic B-field axis. Additionally, the user may choose spectra simulations of either the interior space, the exterior space, both or none. For further illustration of the three-dimensional field distribution, the user can swith on a “movie” in which all slices perpendicular to the y-axis are plotted serially.

This Matlab code works on Matlab version 7.0 (R14, The Mathworks, Germany).

```
clear;

% configurations
scale=800;                      % spectrometer frequency in MHz
chiblack=-8.3*10^-6;            % susceptibility of BLACK (=0) in png image
chiwhite=-9.0*10^-6;            % susceptibility of WHITE (=1) in png image
spflag=1;                       % 1 for spectrum of BLACK, -1 for WHITE, 0 for all, 2 for nothing
pic=2;                          % 1 if picture is a file, 2=Sphere, 3=Cube
pixel=100;                      % size of Sphere/Cube, BLACK = interior
reldiag=0.3;                    % rel. diam. for SphereCube
path='d:\matlab\bottom.png';    % image path
proj=-1;                        % expansion projection direction of image to 3D; 1=z, 2=x, 3=y
                                % -1=rotation about z-axis
splotflag=0;                    % 1 for "movie" figure

'import image'
pause(0.001);
if pic==1
    A=imread(path);
    C = .2989*A(:,:,1)+.5870*A(:,:,2)+.1140*A(:,:,3); % uint8 RGB to gray scale
    C=single(C)./256;
    if proj==1 D(1,:,:)=C; E = repmat(D,[size(C,1) 1 1]);
    elseif proj==2 D(:,1,:)=C; E = repmat(D,[1 size(C,1) 1]);
```

```
    elseif proj==3 E = repmat(C,[1 1 size(C,1)]);
    elseif proj==-1
        'rotate image'
        centr=floor(size(C,1)/2);
        for i=1:size(C,1)
            for j=1:size(C,1)
                radi=floor( ((i-centr)^2+(j-centr)^2)^0.5);
                if centr+radi<=size(C,2)
                    E(:,i,j)=C(:,centr+radi);
                else
                    E(:,i,j)=C(:,size(C,2));
                end
            end
        end
    end
elseif pic==2 %Sphere
    x=[-0.5:1/(pixel-1):0.5];
    z(1,1,:)=x;
    R=(repmat(x.^2,[pixel 1 pixel])+repmat(x.^2',[1 pixel pixel])+...
        repmat(z.^2,[pixel pixel 1])).^0.5;
    S=R;
    S(find(R>reldiag/2))=1;
    S(find(R<=reldiag/2))=0;
    E=uint8(S);
    E=single(E);
    clear x z R S;
else %Cube
    S=ones(pixel,pixel,pixel);
    S(  round((1-reldiag)/2*pixel):round((1+reldiag)/2*pixel)-1,...
        round((1-reldiag)/2*pixel):round((1+reldiag)/2*pixel)-1,...
        round((1-reldiag)/2*pixel):round((1+reldiag)/2*pixel)-1 ) =...
        zeros(round((1+reldiag)/2*pixel)-round((1-reldiag)/2*pixel),...
            round((1+reldiag)/2*pixel)-round((1-reldiag)/2*pixel),...
            round((1+reldiag)/2*pixel)-round((1-reldiag)/2*pixel));
    E=uint8(S);
    E=single(E);
end

% ensure square matrix
if size(E,1)~=size(E,2) | size(E,1)~=size(E,3) | size(E,3)~=size(E,2)
    E=E(1:min([size(E,1) size(E,2) size(E,3)]),1:min([size(E,1) size(E,2) size(E,3)]),...
        1:min([size(E,1) size(E,2) size(E,3)]));
end

% ensure odd matrix size
if mod(size(E,1),2)~=1 E=E(2:size(E,1),2:size(E,1),2:size(E,1)); end
Chi(:,:,:,4)=(-E+max(max(max(E)))) .*(chiblack-chiwhite)+chiwhite;

'create x,y,z-scale and kx,ky,kz-scale'
pause(0.001);
x=size(Chi,2);
Chit=zeros(x,x,x,4);
for i=1:size(Chi,1)
    Chi(i,:,:,1)=(-1+((i-1)*2*1/(x-1))).*ones(1,x,x); % z
```

```
    Chi(:,i,:,2)=(-1+((i-1)*2*1/(x-1))).*ones(x,1,x); % x
    Chi(:,:,i,3)=(-1+((i-1)*2*1/(x-1))).*ones(x,x,1); % y
    Chit(i,:,:,1)=(-(x-1)/1/2+(i-1)*(x-1)/(1)/(x-1)).*ones(1,x,x); % kz
    Chit(:,i,:,2)=(-(x-1)/1/2+(i-1)*(x-1)/(1)/(x-1)).*ones(x,1,x); % kx
    Chit(:,:,i,3)=(-(x-1)/1/2+(i-1)*(x-1)/(1)/(x-1)).*ones(x,x,1); % ky
end
Chit=single(Chit); Chi=single(Chi);

'calculate Bt-field'
pause(0.001);
Chit(:,:,:,4)=fftshift(fftn(Chi(:,:,:,4)));
B(:,:,:,1:3)=Chi(:,:,:,1:3);
clear Chi;
Bt(:,:,:,1:3)=Chit(:,:,:,1:3); % now physics!
Bt(:,:,:,4)=Chit(:,:,:,4).*(1/3-Chit(:,:,:,1).^2./(Chit(:,:,:,1).^2+Chit(:,:,:,2).^2+Chit(:,:,:,3).^2));
clear Chit;
'calculate B-field'
pause(0.001);
% singularity --> substitude with dc-offset
Bt(size(Bt,1)/2+0.5,size(Bt,2)/2+0.5,size(Bt,3)/2+0.5,4)=0;
B(:,:,:,4)=(ifftn(ifftshift(Bt(:,:,:,4))));
Deltaf(:,:,:)=scale*10^6*real(B(:,:,:,4)); % frequency shift distribution in Hz

'plot'
pause(0.001);

h=figure('Position',[5 700 830 760]);
% movie
if splotflag==1
    for i=1:size(Deltaf,3)
        Df(:,:)=Deltaf(:,:,i);
        imagesc(B(1,:,1,2),B(:,1,1,1),Df,[min(min(min(Deltaf))) max(max(max(Deltaf)))]);
        colorbar; colormap(jet(128)); title(sprintf('%d of %d',i,size(Deltaf,3)));
        pause(0.01);
        M(i)=getframe;
    end
end

Df(:,:)=Deltaf(:,:,size(B,1)/2+0.5);
jetfac=round((max(max(Df))-min(min(Df)))/5);
imagesc(B(1,:,1,2),B(:,1,1,1),Df);colormap(jet(jetfac)); colorbar;
title('\Delta f in Hz, Stepsize 5 Hz','FontSize',16);
set(gca,'TickDir','out');

if spflag~=2
    'create spectrum'
    pause(0.001);
    amp=1;
    fwhm=3; % control FWHM in Hz
    a=amp.*0.25.*fwhm^2; b=0.25.*fwhm.^2;
    if spflag==1 I=-round(E)+1; elseif spflag==-1 I=round(E); else I=ones(size(E)); end
    Df1=Deltaf(find(I==1));
    if min(min(Df1))*max(max(Df1))<0
        hz=[min((min(Df1)))-0.3*abs(max((max(Df1)))-min((min(Df1)))):...
```

```
            abs((max(max(Df1)))-min((min(Df1))))/100:...
            max((max(Df1)))+0.3*abs((max(max(Df1)))-min((min(Df1))))];
    elseif min(min(Df1))*max(max(Df1))>0 & min(min(Df1))>0
        hz=[-fwhm*2:...
            abs((max(max(Df1)))+fwhm*2)/100:...
            2*max((max(Df1)))];
    else
        hz=[2*min(min(Df1)):...
            abs((min(min(Df1)))-fwhm*2)/100:...
            +fwhm];
    end
    spect=zeros(size(hz)); spectzero=zeros(size(hz));
    t=cputime;
    for i=1:numel(Df1)
        spect=spect+ a.*(1./((hz-Df1(i)).^2+b));
           if cputime-t>1
            sprintf('%u of %u',i,numel(Df1))
            t=cputime;
           end
    end
    % sum of pixels
    spectzero=numel(Df1).*a.*(1./((hz).^2+b));
    maxsp=max(spect); maxspz=max(spectzero);
    p=figure('Position',[840 500 430 760]);
    plot(hz,spectzero./maxspz,hz,spect./maxspz,hz,spect./maxsp);
    legend(sprintf('In pure solution, FWHM = %d Hz', fwhm),'Susceptibility affected',...
        sprintf('Susceptibility affected (x %3.1f)',maxspz/maxsp));
    grid on;
    axis([min(hz) max(hz) 0 1.2]);
    xlabel('Frequency in Hz');
end
```

8.2. Pulse Program Codes

Modified pulse programs are presented in Bruker's pulse program language.

8.2.1. Pulse-Acquire with Excitation Sculpting and Pulse-Train Presaturation

The standard "double watergate" excitation sculpting pulse sequence [Hwang & Shaka 1995] (Bruker nomenclature "zgesgp") was upgraded with a presaturation, which consisted of 200 sinc-shaped pulses of length 10 ms [Araníbar et al. 2006].

```
prosol relations=<triple>
#include <Avance.incl>
#include <Grad.incl>
"p2=p1*2"
"d12=20u"

1 ze
2 30m
        d1
  d12 pl0:f1 BLKGRAD
3 (p18:sp6 ph10):f1              ;wiggling presat
        40u
        lo to 3 times l5
  d12 pl1:f1
  p1 ph1         ;excitation

  50u UNBLKGRAD
  p16:gp1                ;excitation sculpting
  d16 pl0:f1
  (p12:sp1 ph2:r):f1
  4u
  d12 pl1:f1

  p2 ph3

  4u
  p16:gp1
  d16
  50u
  p16:gp2
  d16 pl0:f1
  (p12:sp1 ph4:r):f1
  4u
  d12 pl1:f1

  p2 ph5
```

```
  4u
  p16:gp2
  d16

  go=2 ph31
  30m mc #0 to 2 F0(zd)
  4u BLKGRAD
exit


ph1=0
ph2=0 1
ph3=2 3
ph4=0 0 1 1
ph5=2 2 3 3
ph10=0
ph31=0 2 2 0


;pl0 : 120dB
;pl1 : f1 channel - power level for pulse (default)
;sp1 : f1 channel - shaped pulse 180 degree
;sp6 : f1 channel - shaped wiggle pulse
;p1 : f1 channel -  90 degree high power pulse
;p2 : f1 channel - 180 degree high power pulse
;p12 : f1 channel - 180 degree shaped pulse (Squa100.1000)   [2 msec]
;p16 : homospoil/gradient pulse
                                                    [1 msec]
;p18 : wiggling presat pulse
                                                            [10 msec]
;d1 : additional relaxation delay
;d12: delay for power switching                               [20 usec]
;d16: delay for homospoil/gradient recovery

;l5 : wiggling presat loop
                                                                    [200]
;NS: 8 * n, total number of scans: NS * TD0
;DS: 4

;use shaped pulses:
;spnam1: Squa100.1000
;spnam6: Sinc1.1000

;for z-only gradients:
;gpz1: 31%
;gpz2: 11%

;use gradient files:
;gpnam1: SINE.100
;gpnam2: SINE.100
```

8.2.2. Diffusion Weighting with Excitation Sculpting and Pulse-Train Presaturation

The standard pulse sequence for bipolar pulsed field gradient-based stimulated echo with longitudinal eddy-current delay (Bruker nomenclature “ledbpgp2s1d”) was upgraded with a “double watergate” excitation sculpting watersuppression (copied from “zgesgp”) and a presaturation, which consisted of 200 sinc-shaped pulses of length 10 ms [Araníbar et al. 2006].

```
prosol relations=<triple>

#include <Avance.incl>
#include <Grad.incl>
#include <Delay.incl>


"p2=p1*2"
"d12=20u"


"DELTA1=d20-p1*2-p2-p30*2-d16*2-p19-d16-d12-4u"
"DELTA2=d21-p19-d16-d12-8u"


1 ze
2 30m
  d12 pl0:f1 BLKGRAD
3 (p18:sp6 ph10):f1               ;wiggling presat
        1m
        lo to 3 times l5
  d12 pl1:f1

  p1 ph1         ;excitation
  p30:gp6
  d16
  p2 ph1
  p30:gp6*-1
  d16
  p1 ph2
  p19:gp7
  d16 pl9:f1
  DELTA1 cw:f1 ph29
  4u do:f1
  d12 pl1:f1
  p1 ph3
  p30:gp6
  d16
  p2 ph1
  p30:gp6*-1
  d16
  p1 ph4
```

```
  p19:gp8
  d16 pl9:f1
  DELTA2 cw:f1 ph29
  4u do:f1
  d12 pl1:f1
  4u BLKGRAD
  p1 ph5

        50u UNBLKGRAD             ;excitation sculpting
  p16:gp1
  d16 pl0:f1
  (p12:sp1 ph22:r):f1
  4u
  d12 pl1:f1

  p2 ph23

  4u
  p16:gp1
  d16
  50u
  p16:gp2
  d16 pl0:f1
  (p12:sp1 ph24:r):f1
  4u
  d12 pl1:f1

  p2 ph25

  4u
  p16:gp2
  d16

  go=2 ph31
  30m mc #0 to 2 F0(zd)
exit


ph1= 0
ph2= 0 0 2 2
ph3= 0 0 0 0 2 2 2 2  1 1 1 1 3 3 3 3
ph4= 0 2 0 2 2 0 2 0  1 3 1 3 3 1 3 1
ph5= 0 0 0 0 2 2 2 2  1 1 1 1 3 3 3 3
ph10= 0
ph22=0 1 0 1 2 3 2 3  1 2 1 2 3 0 3 0
ph23=2 3 2 3 0 1 0 1  3 0 3 0 1 2 1 2
ph24=0 0 1 1 2 2 3 3  1 1 2 2 3 3 4 4
ph25=2 2 3 3 0 0 1 1  3 3 0 0 1 1 2 2
ph29=0
ph31=0 0 0 0 2 2 2 2  3 3 3 3 1 1 1 1


;pl1 : f1 channel - power level for pulse (default)
;sp1 : f1 channel - shaped pulse 180 degree
```

```
;sp6 : f1 channel - shaped wiggle pulse
;p1  : f1 channel -  90 degree high power pulse
;p2  : f1 channel - 180 degree high power pulse
;p12 : f1 channel - 180 degree shaped pulse (Squa100.1000)   [2 msec]
;p16 : homospoil/gradient pulse                                [1 msec]
;p18 : wiggling presat pulse                                          [10 msec]
;p19: gradient pulse 2 (spoil gradient)
;p30: gradient pulse (little DELTA * 0.5)
;d1  : relaxation delay; 1-5 * T1
;d12: delay for power switching                     [20 usec]
;d16: delay for gradient recovery
;d20: diffusion time (big DELTA)
;d21: eddy current delay (Te)                        [5 ms]
;l5 : wiggling presat loop                                                  [200]
;NS: 8 * n
;DS: 4 * m

;use shaped pulses:
;spnam1: Squa100.1000
;spnam6: Sinc1.1000

;use gradient ratio:    gp 6 : gp 7   : gp 8
;                       var  : -17.13 : -13.17

;for z-only gradients:
;gpz1: 31%
;gpz2: 11%
;gpz6: 1-100%
;gpz7: -17.13% (spoil)
;gpz8: -13.17% (spoil)

;use gradient files:
;gpnam1: SINE.100
;gpnam2: SINE.100
;gpnam6: SINE.100
;gpnam7: SINE.100
;gpnam8: SINE.100
```

8.2.3. CPMG T_2-Weighting with Excitation Sculpting and Pulse-Train Presaturation

The standard pulse sequence for T_2-weighting according to the Carr-Purrcel-Meiboom-Gill scheme (Bruker nomenklature “cpmg1d”) was upgraded with a “double watergate” excitation sculpting watersuppression (copied from “zgesgp”) and a presaturation, which consisted of 200 sinc-shaped pulses of length 10 ms [Araníbar et al. 2006].

```
prosol relations=<triple>
```

```
#include <Avance.incl>
#include <Grad.incl>
"p2=p1*2"
"d12=20u"

1 ze
2 30m
        d1
  d12 pl0:f1 BLKGRAD
3 (p18:sp6 ph10):f1              ;wiggling presat
        4u
        lo to 3 times l5
  d12 pl1:f1
  p1 ph1                 ;excitation
4       d20
        p2 ph20                  ;cpmg
        d20
        lo to 4 times l20

  50u UNBLKGRAD
  p16:gp1
  d16 pl0:f1
  (p12:sp1 ph2:r):f1
  4u
  d12 pl1:f1

  p2 ph3

  4u
  p16:gp1
  d16
  50u
  p16:gp2
  d16 pl0:f1
  (p12:sp1 ph4:r):f1
  4u
  d12 pl1:f1

  p2 ph5

  4u
  p16:gp2
  d16

  go=2 ph31
  30m mc #0 to 2 F0(zd)
  4u BLKGRAD
exit


ph1=0
ph2=0 1
ph3=2 3
ph4=0 0 1 1
```

```
ph5=2 2 3 3
ph10=0
ph31=0 2 2 0
ph20=1 3


;pl0 : 120dB
;pl1 : f1 channel - power level for pulse (default)
;sp1 : f1 channel - shaped pulse 180 degree
;sp6 : f1 channel - shaped wiggle pulse
;p1 : f1 channel -  90 degree high power pulse
;p2 : f1 channel - 180 degree high power pulse
;p12 : f1 channel - 180 degree shaped pulse (Squa100.1000)   [2 msec]
;p16 : homospoil/gradient pulse
                                                [1 msec]
;p18 : wiggling presat pulse
                                                        [10 msec]
;d1 : relaxation delay; 1-5 * T1
;d12: delay for power switching                          [20 usec]
;d16: delay for homospoil/gradient recovery
;d20 : delay for cpmg spin echo
                                                [0.5 msec]

;l5 : wiggling presat loop
                                                                [200]
;l20 : cpmg loop
                                                                [300]
;NS: 8 * n, total number of scans: NS * TD0
;DS: 4

;use shaped pulses:
;spnam1: Squa100.1000
;spnam6: Sinc1.1000

;for z-only gradients:
;gpz1: 31%
;gpz2: 11%

;use gradient files:
;gpnam1: SINE.100
;gpnam2: SINE.100
```

8.2.4. Triple Inversion Recovery with Excitation Sculpting and Pulse-Train Presaturation

The standard “double watergate” excitation sculpting pulse sequence [Hwang & Shaka 1995] (Bruker nomenclature “zgesgp”) was modified by inserting three 180° pulses and delays in front of the excitation 90° pulse. Water-suppression was upgraded with a presaturation, which consisted of 200 sinc-shaped pulses of length 10 ms [Araníbar et al. 2006]. This water saturation was also inserted during the inversion-recovery delays between the 180° pulses.

```
prosol relations=<triple>
```

```
#include <Avance.incl>
#include <Grad.incl>

define loopcounter myl11
"myl11 = d11/ ( p18 + d18 )"
"d21 = d11 - myl11 * (p18 + d18) + 4u"

define loopcounter myl12
"myl12 = d12/ ( p18 + d18 )"
"d22 = d12 - myl12 * (p18 + d18) + 4u"

define loopcounter myl13
"myl13 = d13/ ( p18 + d18 )"
"d23 = d13 - myl13 * (p18 + d18) + 4u"

"p2=p1*2"

1 ze
2 30m
        d1
  20u pl0:f1 BLKGRAD
3 d18           ;wiggling presat
        (p18:sp6 ph10):f1
        lo to 3 times l5
  20u
        20u pl1:f1



        p2 ph1          ;first IR-pulse
        20u pl0:f1
4 d18           ;wiggling water saturation
        (p18:sp6 ph10):f1
        lo to 4 times myl11
        d21

        20u pl1:f1

        p2 ph1          ;second IR-pulse
        20u pl0:f1

5 d18           ;wiggling water saturation
        (p18:sp6 ph10):f1
        lo to 5 times myl12
        d22
        20u pl1:f1

        p2 ph1          ;third IR-pulse
        20u pl0:f1

6 d18           ;wiggling water saturation
        (p18:sp6 ph10):f1
        lo to 6 times myl13
        d23
```

```
        20u pl1:f1

  p1 ph1         ;excitation pulse

  50u UNBLKGRAD
  p16:gp1                ;excitation sculpting
  d16 pl0:f1
  (p12:sp1 ph2:r):f1
  4u
  20u pl1:f1

  p2 ph3

  4u
  p16:gp1
  d16
  50u
  p16:gp2
  d16 pl0:f1
  (p12:sp1 ph4:r):f1
  4u
  20u pl1:f1

  p2 ph5

  4u
  p16:gp2
  d16

  go=2 ph31
  30m mc #0 to 2 F0(zd)
  4u BLKGRAD
exit


ph1=0
ph2=0 1
ph3=2 3
ph4=0 0 1 1
ph5=2 2 3 3
ph10=0
ph31=0 2 2 0


;pl0 : 120dB
;pl1 : f1 channel - power level for pulse (default)
;sp1 : f1 channel - shaped pulse 180 degree
;sp6 : f1 channel - shaped wiggle pulse
;p1 : f1 channel -  90 degree high power pulse
;p2 : f1 channel - 180 degree high power pulse
;p12 : f1 channel - 180 degree shaped pulse (Squa100.1000)   [2 msec]
;p16 : homospoil/gradient pulse
                                                    [1 msec]
;p18 : wiggling presat pulse
                                                              [10 msec]
```

```
;d1 : additional relaxation delay
;d11 : 1st IR-delay [1.5 sec]
;d12 : 2nd IR-delay [0.7 sec]
;d13 : 3rd IR-delay [0.215 sec]
;d16: delay for homospoil1/gradient recovery
;d18 : delay between wiggling pulses [20u]
;l5 : wiggling presat loop                                    [200]
;NS: 8 * n, total number of scans: NS * TD0
;DS: 4

;use shaped pulses:
;spnam1: Squa100.1000
;spnam6: Sinc1.1000

;for z-only gradients:
;gpz1: 31%
;gpz2: 11%

;use gradient files:
;gpnam1: SINE.100
;gpnam2: SINE.100
```

8.3. Deconvolution Routine for Quantification of NMR Spectra

The following Matlab code enables deconvolution of NMR spectra assuming Gaussian-Lorentzian lineshapes, whose start values, fitting boundaries and inter-peak relationships of chemical shifts, amplitudes, linewidths, multiplett structures, J-coupling constants and Gaussian-Lorentzian ratios must be supplied in an Excel-sheet. The syntax of this Excel-sheet is also given.

8.3.1. Matlab Code of Spectral Deconvolution Routine

All user interactions are within the first 30 lines, namely the spectral range for fitting, file-pathes to the ASCII-format spectra (exported with Bruker command “convbin2asc”) and to the Excel-sheet, the numbers of the NMR spectra (note: They must be saved as e.g. “2.txt”.), a keyword for saving, and the fit parameters for the additional linear baseline fit.

This Matlab code works on Matlab version 7.0 (R14, The Mathworks, Germany).

```
clear;
```

```
%fit boundaries
f1p=1.5; f1pp=f1p;           % left boundary in ppm
f2p=0.8; f2pp=f2p;

%import export parameters
path='d:\files\';           % spectra files in ASCII-format
xls='d:\Compounds.xls';     % Excel file for predefined peaks
p=[1:20];
key='test'; %keyword for saving

for j=1:size(p,2)

    clear number amp hz ppm;
    [number amp hz ppm]=textread([path sprintf('%d',p(j)) '.txt'],...
           '%f, %f, %f, %f','headerlines',1);
       amp=amp./1000000;

hzfac=ppm(1)/hz(1); % converting hz to ppm

% fit parameter for linear baseline y=ax+b
bla         =0; % slope start value
blalower    =-max([abs(max(amp)/max(ppm)) abs(min(amp)/max(ppm))]); % slope lower boundary
blaupper    =-blalower;
blb         =mean(amp(find(ppm<f1p,1):find(ppm<f2p,1))); % offset start value
blblower    =-0.1*max(amp); % offset lower boundary
blbupper    =0.1*max(amp);

%%%%%%%%%%%%%%%%%%%%%%%%%%%%%%%%%%%%%%%%%%%%%%%%%%%%%%%%%%%%%%%%%%%%%%%%%%%%

%xls import
[P1,T1]=xlsread(xls);
T2=T1(3:size(T1,1),:);
P3=P1(find(P1(:,1)==0),:);
T3=T2(find(P1(:,1)==0),:);
P=P3(find(P3(:,5)<f1p & P3(:,5)>f2p),:);
T=T3(find(P3(:,5)<f1p & P3(:,5)>f2p),:);
% parameters
num=P(:,2)';
name=T(:,3)';
fitpos=P(:,4)';
position=P(:,5)';
for i=1:size(num,2)
    ppos(i)=find(ppm<position(i),1);
end
poslower=P(:,6)';
posupper=P(:,7)';
fitamp=P(:,8)';
fitampfac=P(:,9)';
amplitude=P(:,10)';
for i=1:size(num,2)
    if isnan(amplitude(i))==1
        if abs(amp(ppos(i)))<0.3*std(amp(find(ppm<f1pp,1):find(ppm<f2pp,1))) %if amp is too close to zero!
            amplitude(i)=std(amp(find(ppm<f1pp,1):find(ppm<f2pp,1)));
        else
```

```
            amplitude(i)=amp(ppos(i));
        end
    end
end
amplower=P(:,11)'.*abs(amplitude);
ampupper=P(:,12)'.*abs(amplitude);
fitwidth=P(:,13)';
width=P(:,14)';
widlower=P(:,15)';
widupper=P(:,16)';
multiplet=P(:,17)';
jfit=P(:,18)';
jcoup=P(:,19)';
jlower=P(:,20)';
jupper=P(:,21)';
fitglr=P(:,22)';
glr=P(:,23)';
glrlower=P(:,24)';
glrupper=P(:,25)';

%%%%%%%%%%%%%%%

      positionv=position;
      position=position(find(fitpos==0));
      poslower=poslower(find(fitpos==0));
      posupper=posupper(find(fitpos==0));

      amplitudev=amplitude;
      amplitude=amplitude(find(fitamp==0));
      amplower=amplower(find(fitamp==0));
      ampupper=ampupper(find(fitamp==0));

      widthv=width;
      width=width(find(fitwidth==0));
      widlower=widlower(find(fitwidth==0));
      widupper=widupper(find(fitwidth==0));

      jcoupv=jcoup;
      jcoup=jcoup(find(multiplet~=1 & jfit==0));
      jlower=jlower(find(multiplet~=1 & jfit==0));
      jupper=jupper(find(multiplet~=1 & jfit==0));

      glrv=glr;
      glr=glr(find(fitglr==0));
      glrlower=glrlower(find(fitglr==0));
      glrupper=glrupper(find(fitglr==0));

      % find metabolite linewidth (fitwidth=-1) via DSS-fitting
      if isempty(find(fitglr==-1))~=1 | isempty(find(fitwidth==-1))~=1
          gtype=fittype('a*((1-g)*0.25*f^2*(1/((x-b)^2+0.25*f^2)) + g*exp(-8*log(2)*(x-b)^2/2/f^2))',...
              'ind','x','coeff',{'a','b','f','g'});
           gopts=fitoptions('method', 'NonlinearLeastSquares', ...% 'Robust', 'On', ...
               'Lower', [-5*abs(amp(find(ppm<0,1))) -0.001 1*hzfac 0], 'Upper', ...
               [5*abs(amp(find(ppm<0,1))) 0.001 30*hzfac 1], 'Startpoint', ...
```

```
        [amp(find(ppm<0,1)) 0 5*hzfac 0.5], 'MaxIter',1000,...
        'MaxFunEvals', 10000,'Display','iter');
    g1p=find(ppm<0.02,1); g2p=find(ppm<-0.02,1);
    gresult=fit(ppm(g1p:g2p), amp(g1p:g2p),gtype,gopts);
    fdss=gresult.f;
    fdssh=fdss/hzfac;
    gdss=gresult.g;
else
   fdss=NaN; fdssh=NaN; gdss=NaN;
end


% fit boundaries; coefficients
start=[jcoup.*hzfac amplitude position width.*hzfac glr];
%start=abs(start);
start=[start bla blb];
lower=[jlower.*hzfac amplower poslower widlower.*hzfac glrlower];
%lower=abs(lower);
lower=[lower blalower blblower];
upper=[jupper.*hzfac ampupper posupper widupper.*hzfac glrupper];
%upper=abs(upper);
upper=[upper blaupper blbupper];

c=clock;
['DSS linewidth = ' sprintf('%2.2f Hz', fdssh) '; DSS glr= ' sprintf('%2.2f',gdss) ...
    ' --> Expno ' sprintf('%d',p(j)) ': Start FIT at '...
    sprintf('%02.0f',c(4)) ':' sprintf('%02.0f',c(5)) ':' sprintf('%02.0f',c(6))]

%fit type and options
fitstring='0';
for m=1:size(num,2)
    ms=sprintf('%02d',num(m));
    if fitwidth(m)==0    % check if width is fit
        fms=['f' ms];
    elseif fitwidth(m)==-1
        fms=sprintf('%f',fdss);
    elseif fitwidth(m)==-2
        fms=sprintf('%f',widthv(m)*hzfac);
    else
        fms=sprintf('f%02d',fitwidth(m));
    end

    if fitglr(m)==0    % check if glr is fit
        gms=['g' ms];
    elseif fitglr(m)==-1
        gms=sprintf('%f',gdss);
    elseif fitglr(m)==-2
        gms=sprintf('%f',glrv(m));
    else
        gms=sprintf('g%02d',fitglr(m));
    end

    if fitamp(m)==0      % check if amplitude is fit
        ams=['a' ms];
```

```
            elseif fitamp(m)==-2
                ams=sprintf('%f',amplitudev(m));
            else
                ams=sprintf('%f * a%02d',fitampfac(m),fitamp(m));
            end

            if fitpos(m)==0      % check if position is fit
                bms=['b' ms];
            else
                bms=sprintf('%f',positionv(m));
            end

            if jfit(m)==0      % check if jcoup is fit
                jms=['j' ms];
            else
                jms=sprintf('%f',jcoupv(m)*hzfac);
            end

            if multiplet(m)==1
                fitstring = [fitstring ' + ' ams '*((1-' gms ')*0.25*' fms '^2*(1/((x-' bms ')^2+0.25*'
fms...
                    '^2)) + ' gms '*exp(-8*log(2)*(x-' bms ')^2/2/' fms '^2))'];
            elseif multiplet(m)==2
                fitstring = [fitstring ' + ' ams '*((1-' gms ')*0.25*' fms '^2*(1/((x-' bms '-' jms ...
                     '/2)^2+0.25*' fms '^2)+1/((x-' bms '+' jms '/2)^2+0.25*' fms '^2)) + '...
                     gms '*(exp(-8*log(2)*(x-' bms '-' jms '/2)^2/2/' fms '^2) + ' ...
                     'exp(-8*log(2)*(x-' bms '+' jms '/2)^2/2/' fms '^2)))'];
            elseif multiplet(m)==3
                fitstring = [fitstring ' + ' ams '*((1-' gms ')*0.25*' fms '^2*(0.5/((x-' bms '-' jms ...
                    ')^2+0.25*' fms '^2)+1/((x-' bms ')^2+0.25*' fms '^2)+0.5/((x-' bms '+' jms ...
                    ')^2+0.25*' fms '^2)) + ' ...
                    gms '*(0.5*exp(-8*log(2)*(x-' bms '-' jms ')^2/2/' fms '^2) + ' ...
                    'exp(-8*log(2)*(x-' bms ')^2/2/' fms '^2) + ' ...
                     '0.5*exp(-8*log(2)*(x-' bms '+' jms ')^2/2/' fms '^2)))'];
            end
        end
        fitstring=[fitstring '+a*x+ b'];

        % create cell for ftype-coeff
        for m=1:(size(num,2))

        coeffstringj(m)={['j' sprintf('%02d',num(m))]};
        coeffstringa(m)={['a' sprintf('%02d',num(m))]};
        coeffstringb(m)={['b' sprintf('%02d',num(m))]};
        coeffstringf(m)={['f' sprintf('%02d',num(m))]};
        coeffstringg(m)={['g' sprintf('%02d',num(m))]};
        end
        coeffcell=[coeffstringj(find(multiplet~=1 & jfit==0))...
            coeffstringa(find(fitamp==0)) coeffstringb(find(fitpos==0)) ...
            coeffstringf(find(fitwidth==0)) coeffstringg(find(fitglr==0)) ...
            {'a'} {'b'}];

        clear f;
        %fitting
```

```
ftype=fittype(fitstring, 'ind','x','coeff',coeffcell);
opts=fitoptions('method', 'NonlinearLeastSquares', ...%'Robust', 'On', ...
    'Lower', lower, 'Upper', upper, 'Startpoint', start, 'MaxIter',1000,...
    'MaxFunEvals', 10000,'Display','iter');
f1p=find(ppm<f1p,1); f2p=find(ppm<f2p,1);
fresult=fit(ppm(f1p:f2p), amp(f1p:f2p),ftype,opts);
f=feval(fresult,ppm);

%%%%%%%%%%%%%%%%%%%%%%%%%%%%%%%%%%%%%%%%%%%%%%%%%%%%
% single components of fit for plotting

%extracting and sorting fresults
fitresults=coeffvalues(fresult);
fitresultsj=fitresults(1:size(jcoup,2));
fitresultsjj=fitresultsj;
fitresultsa=fitresults(size(jcoup,2)+1:size(jcoup,2)+size(amplitude,2));
fitresultsaa=fitresultsa;
fitresultsb=fitresults(size(jcoup,2)+size(amplitude,2)+1:...
    size(jcoup,2)+size(amplitude,2)+size(position,2));
fitresultsbb=fitresultsb;
fitresultsff=fitresults(size(jcoup,2)+size(amplitude,2)+size(position,2)+1:...
    size(jcoup,2)+size(amplitude,2)+size(position,2)+size(width,2));
fitresultsf=fitresultsff;
fitresultsgg=fitresults(size(jcoup,2)+size(amplitude,2)+size(position,2)+size(width,2)+1:...
    size(jcoup,2)+size(amplitude,2)+size(position,2)+size(width,2)+size(glr,2));
fitresultsg=fitresultsgg;
fitresultsbl=fitresults(size(fitresults,2)-1:size(fitresults,2));

    m=0;
for i=1:size(num,2) %position is filled with zeros
    m=m+1;
    if fitpos(i)~=0
        fitresultsb(i)=0;
        m=m-1;
    else
        fitresultsb(i)=fitresultsbb(m);
    end
end

for i=1:size(num,2) % zero-filled position get their real values
    if fitresultsb(i)==0
        if fitpos(i)==0
            fitresultsb(i)=fitresultsb(i);
        else
            fitresultsb(i)=positionv(i);
        end
    end
end

    m=0;
for i=1:size(num,2) %amplitude is filled with zeros
    m=m+1;
    if fitamp(i)~=0
        fitresultsa(i)=0;
```

```
        m=m-1;
    else
        fitresultsa(i)=fitresultsaa(m);
    end
end

for i=1:size(num,2) % zero-filled amplitudes get their real values
    if fitresultsa(i)==0
        if fitamp(i)==0
            fitresultsa(i)=fitresultsa(i);
        elseif fitamp(i)==-2
            fitresultsa(i)=amplitudev(i);
        else
            fitresultsa(i)=fitampfac(i).*fitresultsa(find(num==fitamp(i)));
        end
    end
end

    m=0;
for i=1:size(num,2) %width is filled with zeros
    m=m+1;
    if fitwidth(i)~=0
        fitresultsf(i)=0;
        m=m-1;
    else
        fitresultsf(i)=fitresultsff(m);
    end
end
for i=1:size(num,2) % zero-filled widths get their real values
    if fitresultsf(i)==0
        if fitwidth(i)==0
            fitresultsf(i)=fitresultsf(i);
        elseif fitwidth(i)==-1
            fitresultsf(i)=fdss;
        elseif fitwidth(i)==-2
            fitresultsf(i)=widthv(i)*hzfac;
        else
            fitresultsf(i)=fitresultsf(find(num==fitwidth(i)));
        end
    end
end

    m=0;
for i=1:size(num,2) %glr is filled with zeros
    m=m+1;
    if fitglr(i)~=0
        fitresultsg(i)=0;
        m=m-1;
    else
        fitresultsg(i)=fitresultsgg(m);
    end
end
for i=1:size(num,2) % zero-filled glrs get their real values
    if fitresultsg(i)==0
```

```
            if fitglr(i)==0
                fitresultsg(i)=fitresultsg(i);
            elseif fitglr(i)==-1
                fitresultsg(i)=gdss;
            elseif fitglr(i)==-2
                fitresultsg(i)=glrv(i);
            else
                fitresultsg(i)=fitresultsg(find(num==fitglr(i)));
            end
        end
    end

        m=0;
    for i=1:size(num,2) %jcoup is filled with zeros
        m=m+1;
        if multiplet(i)==1 | jfit(i)~=0
            fitresultsj(i)=0;
            m=m-1;
        else
            fitresultsj(i)=fitresultsjj(m);
        end
    end
    for i=1:size(num,2) % zero-filled jcoups get their real values
        if fitresultsj(i)==0
            if jfit(i)==0
                fitresultsj(i)=fitresultsj(i);
            else
                fitresultsj(i)=jcoupv(i)*hzfac;
            end
        end
    end

    clear SINGLE;
    for i=1:size(num,2)
        if multiplet(i)==1
            SINGLE(i,:)=fitresultsa(i).*((1-fitresultsg(i)).*0.25.*fitresultsf(i).^2./...
                 ((ppm-fitresultsb(i)).^2+0.25.*fitresultsf(i).^2) + ...
                 fitresultsg(i).*exp(-8*log(2)*(ppm-fitresultsb(i)).^2/2/fitresultsf(i).^2));
        elseif multiplet(i)==2
            SINGLE(i,:)=fitresultsa(i)*((1-fitresultsg(i)).*0.25*fitresultsf(i).^2.*...
        (1./((ppm-fitresultsb(i)-fitresultsj(i)./2).^2+0.25.*fitresultsf(i).^2)...
        +1./((ppm-fitresultsb(i)+fitresultsj(i)./2).^2+0.25.*fitresultsf(i).^2)) + ...
        fitresultsg(i).*(exp(-8*log(2)*(ppm-fitresultsb(i)-fitresultsj(i)./2).^2/2/fitresultsf(i).^2)   +
...
        exp(-8*log(2)*(ppm-fitresultsb(i)+fitresultsj(i)./2).^2/2/fitresultsf(i).^2)));
        elseif multiplet(i)==3
            SINGLE(i,:)=fitresultsa(i)*((1-fitresultsg(i))*0.25*fitresultsf(i).^2.*...
        (0.5./((ppm-fitresultsb(i)-fitresultsj(i)).^2+0.25.*fitresultsf(i).^2)+...
         1./((ppm-fitresultsb(i)).^2+0.25.*fitresultsf(i).^2)...
        +0.5./((ppm-fitresultsb(i)+fitresultsj(i)).^2+0.25.*fitresultsf(i).^2)) + ...
        fitresultsg(i).*(0.5.*exp(-8*log(2)*(ppm-fitresultsb(i)-fitresultsj(i)).^2/2/fitresultsf(i).^2) +
...
        1.*exp(-8*log(2)*(ppm-fitresultsb(i)).^2/2/fitresultsf(i).^2) + ...
        0.5.*exp(-8*log(2)*(ppm-fitresultsb(i)+fitresultsj(i)).^2/2/fitresultsf(i).^2)));
        end
```

```
        end

        baseline=fitresultsbl(1)*ppm+fitresultsbl(2);%.*ones(size(ppm));

        % result matrix
        SUMSINGLE=sum(SINGLE,2).*(ppm(1)-ppm(size(ppm,1)))./size(ppm,1);
        SUMSINGLE=SUMSINGLE';
        RESULT(j,:)=[p(j) SUMSINGLE];      % look to {names} for component names
        FITRESULTS(j,:)=[p(j) fitresults];


        % plotting
        if j==1 h=figure('Position',[20 300 1200 600],'Color','w'); end
        for i=1:size(num,2)
            plot(ppm,SINGLE(i,:),'Color','b');
            hold all;
        end
        plot(ppm,amp, 'LineWidth',1.4, 'Color','k');
        plot(ppm,f, 'LineWidth',1.2,'Color','r');
        plot(ppm,baseline, 'LineWidth',1.2,'Color','g');
        line([ppm(f1p) ppm(f1p)],[-max(abs(f))/2 max(abs(f))/2],'Color','r','LineWidth',2);
        line([ppm(f2p) ppm(f2p)],[-max(abs(f))/2 max(abs(f))/2],'Color','r','LineWidth',2);
        if isempty(find(fitglr==-1))~=1 & isempty(find(fitwidth==-1))~=1
            title(['Expno ' sprintf('%d',p(j)) '    DSS-linewidth = ' sprintf('%2.2f Hz',fdssh) ...
                    '      DSS-Gaussian-Lorentzian-ratio = ' sprintf('%2.2f',gdss)]);
        else
            title(['Expno ' sprintf('%d',p(j))]);
        end
        set(gca,'XDir','reverse');
        axis([f2pp-(0.5*(f1pp-f2pp)) f1pp+(0.1*(f1pp-f2pp)) 0 max(amp(f1p:f2p))]);
        xlabel('Chemical shift in ppm');
        set(findall(gcf,'-property','FontSize'),'FontSize',14);
        set(findall(gcf,'-property','LineWidth'),'LineWidth',1.5);
        hold off;

        pause(0.1);

        %saving
        c=clock;
        time=sprintf('%02.0f %02.0f %02.0f %02.0f %02.0f',c(1), c(2), c(3), c(4), c(5));
        mkdir([path 'save\' key]);
        saveas(h,[path 'save\' key '\' key sprintf(' - %d',p(j)) '_' time '.jpg']);
        saveas(h,[path 'save\' key '\' key sprintf(' - %d',p(j)) '_' time '.m']);
        save([path 'save\' key '\' ' fresult ' key sprintf(' - %d',p(j)) '_' time],'fresult','-mat');
        save([path 'save\' key '\' ' workspace ' key sprintf(' - %d',p(j)) '_' time]);% workspace
end
xlswrite([path 'save\' key '\' ' integrals ' key '_' time '.xls'],...
    cat(1,cat(2,{'Expno'},name(1:size(num,2))),num2cell(RESULT)));
xlswrite([path 'save\' key '\' ' fitresults ' key '_' time '.xls'],...
    cat(1,cat(2,{'Expno'},coeffcell),num2cell(FITRESULTS)));
```

8.3.2. Excel Template for Configuration of Fit Parameters

In Tab. 8.1 the syntax of an Excel-sheet for the deconvolution routine in Matlab is presented. Explanations of column and row values and possible entries are described within the caption.

	A	B	C	D	E	F	G	H	I	J	K	L	M	N	O	P	Q	R	S	T	U	V	W	X	Y
1	0 = co	Comp	Name of com	chemi cal	Chemic	Lower bo	Upper bo	amplit ude	Factor fo	e in a.u. a = data	Lower bou	bound for amplitude	width fit?	h in Hz,	bound for width	bound for width	t structur	co upl	coupli ng in	bound for j-	bound for j-	gaus sian-	= start	bound for fit	bound for fit
2	active	num	name	fitpos	position	poslower	posupper	fitamp	fitampfac	amplitude	amplower	ampupper	fitwidth	width	widlower	widupper	multiplet	jfit	jcoup	jlower	jupper	fitglr	glr	glrlower	glrupper
3	0	1	DSS	0	0	-0.1	0.1	0	0	a	0	10	0	5	1	20	1	-2	0	0	0	0	0.5	0	1
4	0	2	ML CH3	0	0.88	0.865	0.895	0	0	a	0	2	0	65	55	75	1	-2	0	0	0	0	0.5	0	1
5	0	3	MP CH3	0	0.948	0.938	0.958	0	0	a	0	2	0	65	55	75	1	-2	0	0	0	0	0.5	0	1
6	0	4	Valine d1	0	1.032	1.027	1.082	0	0	a	0	2	-1	0	0	0	2	-2	7.4	0	0	-1	0	0	0
7	0	5	Valine d2	0	0.975	0.97	1.025	4	1	a	0	2	-1	0	0	0	2	-2	7.4	0	0	-1	0	0	0
8	0	6	Isoleucine d1	0	1	0.995	1.05	0	0	a	0	2	-1	0	0	0	2	-2	7.4	0	0	-1	0	0	0
9	0	7	Isoleucine t2	0	0.928	0.923	0.978	6	1	a	0	2	-1	0	0	0	3	-2	7.4	0	0	-1	0	0	0
10	0	8	Leucine d1	0	0.955	0.95	1.005	0	0	a	0	2	-1	0	0	0	2	-2	2.3	0	0	-1	0	0	0
11	0	9	Leucine d2	0	0.9435	0.9385	0.9935	8	1	a	0	2	-1	0	0	0	2	-2	2.3	0	0	-1	0	0	0
12	0	10	M2 Threonine	0	1.22	1.215	1.225	0	0	a	0	2	0	65	55	75	1	-2	0	0	0	0	0.5	0	1
13	0	11	ML CH2 n	0	1.285	1.275	1.3	0	0	a	0	2	0	65	55	75	1	-2	0	0	0	0	0.5	0	1
14	0	12	Lactate d1	0	1.32	1.315	1.325	0	0	a	0	2	-1	0	0	0	2	-2	7	0	0	-1	0	0	0
15	0	13	M3 Alanine	0	1.4	1.395	1.405	0	0	a	0	2	0	65	55	75	1	-2	0	0	0	0	0.5	0	1
16	0	14	Alanine d1	0	1.47	1.465	1.475	0	0	a	0	2	-1	0	0	0	2	-2	7.25	0	0	-1	0	0	0
17	0	15	ML CH2 beta	0	1.56	1.555	1.565	0	0	a	0	2	0	65	55	75	1	-2	0	0	0	0	0.5	0	1
18	0	16	M4	0	1.686	1.681	1.691	0	0	a	0	2	0	65	55	75	1	-2	0	0	0	0	0.5	0	1
19	0	17	DSS 3	0	1.776	1.771	1.781	0	0	a	0	2	0	25	20	30	1	-2	0	0	0	0	0.5	0	1
20	0	18	Acetate	0	1.911	1.906	1.916	0	0	a	0	2	-1	0	0	0	1	-2	0	0	0	-1	0	0	0
21	0	19	NAA	0	2.007	2.002	2.012	0	0	a	0	2	-1	0	0	0	1	-2	0	0	0	-1	0	0	0
22	0	20	ML CH2-CH	0	2.022	2.017	2.027	0	0	a	0	2	0	65	55	75	1	-2	0	0	0	0	0.5	0	1
23	0	21	M5 Glx	0	2.054	2.049	2.059	0	0	a	0	2	0	65	55	75	1	-2	0	0	0	0	0.5	0	1

Tab. 8.1 Excel Template for Configuration of Fit Parameters. Rows represent single peaks or multiplets, Columns: (A) “0” if compound is included in fitting routine, (B) Number of compound, e.g. for referencing to another compound, (C) Name of compound, e.g. for legend of fit result plots, (D) “0” if chemical shift is fit, (E) start value or fixed value of chemical shift in ppm, (F)+(G) lower and upper boundaries for chemical shift fitting in ppm, (H) “0” for separate fit of amplitude, “-2” for no amplitude fit, another compound’s number in case of combined fit with only one amplitude parameter, (I) Relative value of amplitude in case of combined amplitude fitting, (J) amplitude start value, “a” for actual amplitude of spectrum at this chemical shift as start value, (K)+(L) lower and upper boudaries for amplitude fit in relative values (relative to (J)), (M) “0” for separate fit of linewidth, “-1” for linewidh of DSS (determined by fit), “-2” if linewidth is not fit, another compound’s number in case of combined fit with only one linewidth parameter, (N) linewidth start value in Hz, (O)+(P) lower and upper boundaries for linewidth fit in Hz, (Q) multiplet structure, “1”, “2”, “3” for singlet, duplet and triplet, respectively, (R) “0” for separate J-coupling fit, “-2” for no J-coupling fit, (S) start value or fixed value of J-coupling in Hz, (T)+(U) lower and upper boundaries of J-coupling fit, (V) “0” for separate Gaussian-Lorentzian ratio (glr) fit, “-1” for glr of DSS (determined by fit), “-2” for no glr fit, another compound’s number in case of combined fit with only one glr parameter, (W) glr start value or fixed value, (X)+(Y) lower and upper boundaries of glr fit.

9. Danksagung

Danken möchte ich

- Prof. Dr. Ulrich Bogdahn für die interessante Aufgabenstellung, für die zahlreichen und fruchtbaren Diskussionen, für die Ermöglichung der Teilnahme an Konferenzen „auf der ganzen Welt“, für die stets aufbauenden Worte, für den ansteckenden Optimismus, für die gewährte Freiheit und die große Unterstützung,
- Prof. Dr. Dr. Hans Robert Kalbitzer für die Ermöglichung der Durchführung dieser Dissertation an seinem Institut, für die langen und aufschlussreichen Diskussionen über Physik und Biologie, für das Bereitstellen der Messgeräte, für freundschaftliche und gesellige Atmosphäre an seinem Lehrstuhl, und nicht zuletzt für die Geduld bezüglich sprachlichen Feinschliffs dieser Doktorarbeit,
- Prof. Dr. Ludwig Aigner für die Betreuung in der ersten Hälfte dieser Doktorarbeit, für die zahlreichen Gespräche, für die Einführung in seine Arbeitsgruppe, und für die fruchtbare Zusammenarbeit,
- PD Dr. Peter Hau für die Einführung in seine Arbeitsgruppe und die stete Unterstützung,
- der Labor-AG Neuroonkologie von PD Dr. Peter Hau, insbesondere Dr. Arabel Vollmann-Zwerenz, Petra Leukel und Birgit Jachnik für die Bereitstellung unzähliger Zellproben, für die Zellcharakterisierung, für die Beratung in biologischen Fragen und für die freundschaftliche Atmosphäre in ihrem Labor,
- den Mitgliedern und ehemaligen Mitgliedern des Instituts für Molekulare Regenerative Medizin von Prof. Dr. Ludwig Aigner, insbesondere Sebastien Couillard-Després, Sonja Plötz und Francisco Rivera für die Bereitstellung der Zellproben und die Auswertung biologischer Daten und für die interessanten Diskussionen über Stamzellbiologie,
- Dr. Christoph Beier für die fruchtbare Zusammenarbeit,
- den Technischen Assistenten des Lehrstuhls von Prof. Dr. Dr. Hans Robert Kalbitzer, allen voran Dörte Rochelt und Robert Bobardt, für die prompten Hilfen bei technischen Problemen und die Aufrechterhaltung des Routinebetriebs,
- den Teilnehmern des Seminars „Pulsprogramme und Co“ für ihre tollen Vorträge, für die interessanten Diskussionen und für ihr Durchhaltevermögen,
- Tanja Meierhofer, Sandra Kreitner, Maren Eberhardt, Prof. Dr. Werner Kremer für das spontane und geflissentliche Korrekturlesen dieser Doktorarbeit,
- den Direktionsmitarbeiterinnen von Prof. Dr. Ulrich Bogdahn, Stephanie Heigl und Viola Bánrévy, für ihre stete Hilfe bei organisatorischen Problemen, und für die Ermöglichung der zahlreichen Dienstreisen,
- Prof. Dr. Gerd Schmitz und Dr. Margot Grandl für die Bereitstellung der Lipoproteinproben und der Makrophagensuspensionen,

- Prof. Dr. Werner Kremer für die Einführung in das Messen an den NMR-Spektrometern,
- meinen Bürokollegen, Maren Eberhardt und Robert Bobardt, für das freundschaftliche Büroklima und ihre Hilfsbereitschaft,
- Dr. Christian Gröger und Dr. Christoph Liebold für zahlreiche Diskussionen über diese Doktorarbeit und für die Unterstützung in organisatorischen Fragen die Dissertation betreffend,
- dem gesamten Lehrstuhl von Prof. Dr. Dr. Hans Robert Kalbitzer für die tolle Atmosphäre, für die gesellige Kaffeerunde und die zahlreichen Aktivitäten fernab der Forschungstätigkeit,
- meinem Freundeskreis für die Unterstützung, für die aufbauenden Worte und die Ablenkung von der Arbeit,
- und nicht zuletzt meiner Lebensgefährtin Nathalie Strecker für ihre liebevolle Fürsorge und Unterstützung, und für Ihre Nachsicht gerade in den stressigen Phasen dieser Doktorarbeit.